LUMINESCENCE STUDIES OF TRANSITION METAL RELATED DEFECTS IN CRYSTALLINE SILICON

A THESIS FOR THE DEGREE OF
PHILOSOPHIAE DOCTOR

PRESENTED TO
DUBLIN CITY UNIVERSITY

BY

KEVIN GERARD M^C^GUIGAN B. Sc. (Jt. Hons.)
THE SCHOOL OF PHYSICAL SCIENCES
DUBLIN CITY UNIVERSITY

RESEARCH SUPERVISOR
Dr. MARTIN O. HENRY B. Sc. Ph. D.

SEPTEMBER 1989

DECLARATION

THIS THESIS IS BASED ON MY OWN WORK

THIS THESIS IS DEDICATED TO MY PARENTS EDDIE AND SUSAN, TO SINEAD, MY BETTER HALF AND TO THE MEMORY OF RAY AND CELINE HEERAN, WHO HELP KEEP A PERSPECTIVE ON IT ALL.

When things go wrong and will not come right,
Though you do the best you can,
When life looks black as the hour of night -
A PINT OF PLAIN IS YOUR ONLY MAN.

Flann O'Brien

CONTENTS PAGE

CONTENTS 5
ABSTRACT 9

CHAPTER 1: TRANSITION METAL DEFFECTS IN SILICON

1.1 INTRODUCTION 10
1.2 SOLID SOLUBILITIES AND DIFFUSION PROCESSES 12
1.3 LUMINESCENCE STUDIES 14
1.4 NON-OPTICAL STUDIES 18
1.5 CONCLUDING REMARKS 21

CHAPTER 2: BASIC THEORY

2.1 BAND THEORY 22
2.2 BAND SHAPE 24
2.3 IMPURITY STATES 28
2.4 PHONONS 30
2.5 OPTICAL ABSORPTION AND LUMINESCENCE 30
2.6 BOUND EXCITONS 34
2.7 THE VALLEY - ORBIT INTERACTION 36
2.8 ISOELECTRONIC CENTRES 38
2.9 LUMINESCENCE TEMPERATURE DEPENDENCE 39
2.10 TEMPERATURE DEPENDENCE OF LUMINESENCE DECAY TIMES 44

CHAPTER 3: UNIAXIAL STRESS AND ZEEMAN SPECTROSCOPY

3.1 UNIAXIAL STRESS 47
3.2 THEORY 47
3.3 DEFECT CO-ORDINATES 47
3.4 CRYSTAL CO-ORDINATES 55
3.5 TRANSITIONS INVOLVING DEGENERATE STATES 58
3.6 MIXING OF STATES 68
3.7 SPIN - ORBIT COUPLING 70
3.8 ZEEMAN STUDIES 73

CHAPTER 4: EXPERIMENTAL APPARATUS

4.1 INTRODUCTION 78
4.2 SAMPLE PREPARATION 78
4.3 DIFFUSION METHODS 79
4.4 SAMPLE QUENCHING 81
4.5 LOW TEMPERATURE APPARATUS 81
4.6 OPTICAL ARRANGEMENT 83
4.7 SIGNAL PROCESSING 84
4.8 STRESS CELL 87

CHAPTER 5: EXPERIMENTAL RESULTS

5.1 INTRODUCTION 90
5.2 ZINC RELATED PL STUDIES 90
5.2.1 THE 944.8 meV Zn - RELATED PL SYSTEM 90
5.2.2 THE 919 meV Zn - RELATED PL SYSTEM 99
5.2.3 THE 1059.9 meV Zn - RELATED PL SYSTEM 103
5.2.4 THE 1130 AND 1091 meV Zn - IMPLANTED PL SYSTEMS 115
5.3 COPPER RELATED PL STUDIES 122
5.3.1 THE 943.7 meV Cu - RELATED PL CENTRE 122
5.3.2 THE 1034 meV Cu - RELATED PL CENTRE 131

CHAPTER 6: UNIAXIAL STRESS AND ZEEMAN MEASUREMENTS ON THE 943.7 MEV Cu^* PL SYSTEM IN SILICON

6.1 INTRODUCTION 137
6.2.1 UNIAXIAL STRESS MEASUREMENTS 137
6.2.2 P||<111> 139
6.2.3 P||<100> 140
6.2.4 P||<110> 142
6.2.5 POLARIZATION DATA 145
6.3 ANALYSIS OF THE STRESS DATA 145
6.4 ZEEMAN MEASUREMENTS 150
6.5 DEFECT IDENTITY AND DIFFUSION RATE CONSIDERATIONS 159

CHAPTER 7: CONCLUSIONS AND SUGGESTIONS FOR FURTHER WORK

7.1 CONCLUSIONS 162
7.2 SUGGESTIONS FOR FURTHER WORK 164

APPENDIX 1 166

REFERENCES 172

ACKNOWLEDGEMENTS 176

A B S T R A C T

Infra-red photoluminescence (PL) spectra of zinc and copper related defects in silicon are presented in this thesis. Seven new PL systems with principal zero phonon lines at 919.8, 943.67, 945.8, 1033.5, 1059.9, 1090.7 and 1129.8 meV are discussed. All of the spectra can be classified as being due to isoelectronic bound exciton (IBE) recombination. Although the identities of the binding centres have not been conclusively established clear evidence has been obtained in most cases for the involvement of at least one specific transition metal (TM) impurity element.

The PL systems at 945.8, 919.8 and 1059.9 meV are all observed in silicon diffused with zinc and another TM. The 945.8 meV system is observed in silicon diffused with zinc at 1100° C for 16 hours. The system is not created by interstitial Mn and substitutional Zn as previously suggested. The 919 meV system is observed in silicon co-diffused with zinc and copper at 1100° C for 16 hours, while the 1059.9 meV system is most clearly observed in Si:FeZn quenched from 1000° C.

For silicon implanted with zinc the 1129.8 and 1090.7 meV systems are observed. Both of these systems have ground state and excited state splittings placing them in a minority group of IBE centres in silicon associated with deep acceptors and including the indium and thallium systems.

The quenching rate is found to be crucial for samples diffused with copper only. Slow quenches produce the 1034 meV SK system. Zeeman studies on the zero phonon lines of this centre reveal a singlet - triplet nature indicative of a strong central cell potential about the defect as well as a strong crystal field reaction. Rapid quenches combined with low copper concentrations produces the 943.7 Cu^{*} PL system. Uniaxial stress and magnetic field measurements on this centre suggest that the two lowest energy transitions arise from bound exciton recombination at a defect with tetrahedral or near tetrahedral symmetry. Diffusion rate calculations show that a single interstitial copper atom is not the most likely configuration . A larger defect involving one or more

atoms in a T_d arrangement is more likely, perhaps similar to to those already reported for the Mn_4 and Li_4 defects in PL and for the NL22 Fe related centre in EPR.

It is concluded that diffusion is not a suitable method of introducing transition metal impurities into silicon since the process is extremely susceptible to contamination. Implantation of the desired element followed by rapid thermal annealing is suggested as a much more promising avenue of investigation since this method affords much more control over the concentration, implantation depth and most importantly of all, the identity of the chemical element introduced into the host crystal.

CHAPTER 1 : TRANSITION METAL DEFECTS IN SILICON

1.1 INTRODUCTION

Discounting the lanthanides and actinides, transition metals (TM's) constitute over one third of all the known elements. Despite this it has only been since the development of VLSI technology that TM's in silicon have been studied in any great depth.

Since most as-grown wafers are TM contaminated in some way before they arrive at the factory (Graff 1984) TM contamination is one of the more common headaches that semiconductor device manufacturers have to contend with. For example whereas concentrations of as much as 10^{16} cm^{-3} of Cu or Ni don't significantly affect silicon solar cell performance, 10^{15} cm^{-3} Cr, Mn, Fe, Co or 10^{14} cm^{-3} Ti or V can result in a 50 % decrease in efficiency (Hopkins 1977, Rohatgi 1980)

Ludwig and Woodbury (1962) were the first to systematically study TM defects in silicon (using EPR) and they were able to determine the chemical nature, ground-state configuration and defect symmetry of several TM-related centres.

To explain the results of their exhaustive research Ludwig and Woodbury (L & W) proposed an empirical model for the 3d TM atom interaction with the host atoms. This model suggested that under T_d symmetry the 3d level of the TM atom with a $3d^{n-1}$ $4s^p$ configuration (n = 3 to 11, p = 2 except for Cr and Cu) splits into 2 levels corresponding to the e and t_2 representations of the T_d symmetry group. This splitting is usually termed the *crystal field splitting*. If the TM atom occupies an interstitial site it obeys Hund's rule of maximum multiplicity and, if the splitting between the e and t_2 levels is small, allows the orbitals to fill in such a manner as to maximize the total spin while satisfying Pauli's exclusion principle, as illustrated in Fig. 1.1.

If a TM atom enters substitutionally then four of its valence electrons are taken up to complete the covalent bonds with the Si lattice, while the remaining electrons outside

ION		V^{2+}	Cr^{+}, Mn^{+}	Mn^{o}, Fe^{+}
CONFIGURATION		$3d^3$	$3d^6$	$3d^7$
FILLING OF 3d ORBITALS	e	—	↑	↑
		—	↑	↑
	t_2	↑	↑	↑
		↑	↑	↑↓
		↑	↑↓	↑↓

Fig. 1.1 Filling of orbitals of interstitial TM ions according to the Ludwig - Woodbury model

the n = 2 shell all occupy the 3d level which we know splits into e and t_2 states. The sign of the crystal field interaction is reversed with respect to the interstitial case leaving the t_2 level higher in energy than the e level as shown in Fig. 1.2. This model adequately explained all the observed EPR spectra for TM centres in Si.

ION		Cr^{+}, Mn^{+}	Mn^{2-}
CONFIGURATION		$3d^2$	$3d^5$
FILLING OF 3d ORBITALS	t_2	—	↑
		—	↑
		—	↑
	e	↑	↑
		↑	↑

Fig. 1.2 Filling of orbitals of substitutional TM ions according to the Ludwig - Woodbury model

Since then, neutron activation analysis (NAA), deep level transient spectroscopy (DLTS), Hall measurements, photoluminescence (PL) and optical absorption methods have been used to examine such defects. In many cases the results were conflicting and confusing with the effect that it was only when comprehensive studies combining many of these techniques were conducted that identifications of the defects

could be made with any degree of confidence.

Some general conclusions have been extracted from the wealth of data accumulated over the years. These are listed in the following sections.

1.2 SOLID SOLUBILITIES AND DIFFUSION PROCESSES

The diffusion processes of TM's in silicon can be described by Eq. 1.1 (Weber 1983)

$$D = D_0 \exp(-Q/kT) \qquad (1.1)$$

where Q can be considered to be the activation energy needed for the TM diffusant to overcome the potential barrier between lattice sites and D_0 is analogous to the attempt frequency. In general both diffusivity and solubility increase as the atomic number of the diffusant and the temperature of the diffusion increase. It would appear that interstitial diffusion is the dominant process for all 3d TM's at high temperatures, but despite this only Cr, Mn, and Fe can be quenched into interstitial sites since Ni, Co, Cu and Pd all seem to precipitate easily and form clusters during the quenching procedures, no matter what the rate. A table of solubilities is given in Table 1.1. On average the values of diffusivity for TM's is of the same order as solute atoms in liquid solutions ! (Weber 1983). In fact Ni diffuses through silicon so fast that even at 700°C samples of dimension 7 mm x 4 mm x 1 mm achieve saturation level after only 2 minutes (Wiehl 1983).

Substitutional TM impurities seem only to form in either radiation damaged silicon that has an excess of vacancies or as a result of cooling a super-saturated TM solution in the silicon sample (e.g. Cu co-diffused with Mn produces substitutional Mn, (Ludwig et al. 1962)). High TM concentrations have been detected close to the sample surfaces in many diffusion experiments and this has been interpreted by some as evidence of a slowly diffusing substitutional species (Collins 1957) but this could just as

easily be explained as surface induced gettering formed during the quench (Yamaguchi 1963).

Comparisons between the Si:Ti and Si:Ni liquidus curves (Hansen 1958, Shunk 1969) show that they can be described by the same parameters indicating comparable interaction energies of Si with all the 3d TM's (Weber 1983).

Close examination of the solid solubilities in Table 1.1. allows a distinction into 2 groups to be made between the 3d TM's. (Weber 1983) ;

Group 1 : Cr, Mn, Fe, Co (Ti,V)

Group 2 : Ni, Cu

DIFFUSANT	DIFFUSION COEFFICIENT ($1100^{o}C$) cm^2/sec	SOLUBILITY ($1100^{o}C$)cm^{-3}	METHOD
Ti	6×10^{-11}	2×10^{13}	TRACER
V	$\approx 10^{-7}$	$\approx 10^{13}$	DLTS
Cr	2×10^{-6}	3×10^{14}	p/n JCT
Mn	3×10^{-6}	3×10^{15}	TRACER
Fe	4×10^{-6}	3×10^{15}	TRACER
Co	$\approx 10^{-5}$	4×10^{15}	NAA
Ni	4×10^{-5}	5×10^{17}	TRACER
Cu	1×10^{-4}	9×10^{17}	TRACER
Zn	$\approx 10^{-7}$		TRACER
Li	1×10^{-5}		VARIOUS
B	1×10^{-13}		
P	3×10^{-13}		p/n JCT
^{31}Si	5×10^{-16}		TRACER

TABLE 1.1 Solubilities and diffusivities of TM's and other dopants in silicon.

The formation enthalpies for each group have been calculated to be ≈ 2.1 eV and ≈ 1.5 eV respectively which Weber explains by the group 1 elements diffusing as neutral interstitials while the group 2 do so as positively charged interstitials.

1.3 LUMINESCENCE STUDIES

TM related defects in Si were first detected in PL by Mitchard in 1979 although it was not interpreted as such, and by Weber in 1980. Since then much research has been directed into this area. Table 1.2 gives a short list of some of the TM related PL centres reported in the intervening years. It should be noted that the TM listed with each centre in Table 1.2 are mostly only tentatively suggested as being involved (except for the 1014 meV copper related centre) since positive identification of defect constituents are usually based on isotope effects which are very small for elements of such high atomic mass. The energies listed in the table are of the lowest energy zero phonon line.

ENERGY (meV)	TM RELATED	REFERENCE	
1014	Cu-Cu	J. Weber	1982
834/781	Au	D. Thebault	1983
1067	Fe-B	D.H. Mohring	1984
844	Cr-B	H. Conzelmann	1984
1087	Fe-Tl	S.P. Watkins	1984
560	Mn_4	H. Conzelmann	1984
943	Zn-Mn	M.O. Henry	1987
735	Fe-	M.C. do Carmo	1987
822	V	H. Conzelmann	1987
677	Cr-Ga	H. Conzelmann	1987
943	Cu-	K.G. McGuigan	1988
916	Cu-Zn	N. O'Donnell	1988
1060	Zn-Fe	M.O. Henry	1988

Table 1.2 Some TM related defects reported over the past 10 years

The TM related spectra seem to split roughly into 2 groups. The first group containing Cu and Fe related centres exhibit long PL lifetimes, similar spectral zero phonon line (ZPL)

level schemes, and high absolute intensities despite low defect concentration indicating quantum efficiencies approaching unity. These spectra are believed to arise from excitonic decay at isoelectronic defects. Table 1.3 lists the lifetimes of some of these long-lived centres as well as some non-TM related PL decay times for comparison purposes.

An isoelectronic identification for these defects explains their long lifetimes nicely. Conzelmann (1987) has suggested that since the isoelectronic bound exciton (IBE) is essentially a two particle system the Auger process of non-radiative decay cannot operate here since this requires a third particle, an electron (or hole), to absorb all the energy from the excitonic recombination and be excited into the conduction band (valence band). The lifetime of PL from such centres is therefore usually determined by the radiative

CENTRE	LIFETIME (MICROSECONDS)	REFERENCE
Cu-Zn	9000	O'Donnell 1988
Cu-Cu	600	Watkins 1982
Zn-?	240	Henry 1988
Fe-In	200	Thewalt 1982
Fe-Tl	52	Thewalt 1981
Fe-B	30	Conzelmann 1985
In	2.7×10^{-3}	Vouk 1977
Tl	2.8×10^{-4}	Steiner 1984

Table 1.3 PL lifetimes for various centres.

recombination probability of the exciton bound to the defect. Some of the more interesting PL centres in this group are the Cu-Cu, Fe-Tl and Fe-In defects. The Cu-Cu 1014 meV PL system is interesting in that it is the only TM-related defect to have isotope shifts in its zero phonon lines (ZPL) and phonon replicas observed, which has been interpreted as direct proof that at least 2 Cu atoms participate in the defect. The 1014 meV system is shown in Fig. 1.3. The Fe-Tl and Fe-In systems

deserve a mention because each defect has been found to exist in two different configurations and can transform between these depending on the sample temperature. For $T < 15$ K the Fe-Tl centre has trigonal symmetry but for $15 \text{ K} \leq T \leq 20$ K it re-orients itself along a <100> axis to become a rhombic centre (Watkins 1985, Conzelmann 1986). Similar effects have been recently reported for sulphur and selemium centres in silicon (Singh et al. 1989).

Sauer (1983) has suggested that both these centres along with the Fe-B system consist of an interstitial Fe^{+} with an ionized acceptor occupying an adjacent substitutional site. This model is in good agreement with EPR data taken by Ludwig and Woodbury (1962) and Graff (1981).

So far, all the reported TM-related IBE defects agree with isoelectronic pseudo-donor models (Conzelmann 1987).

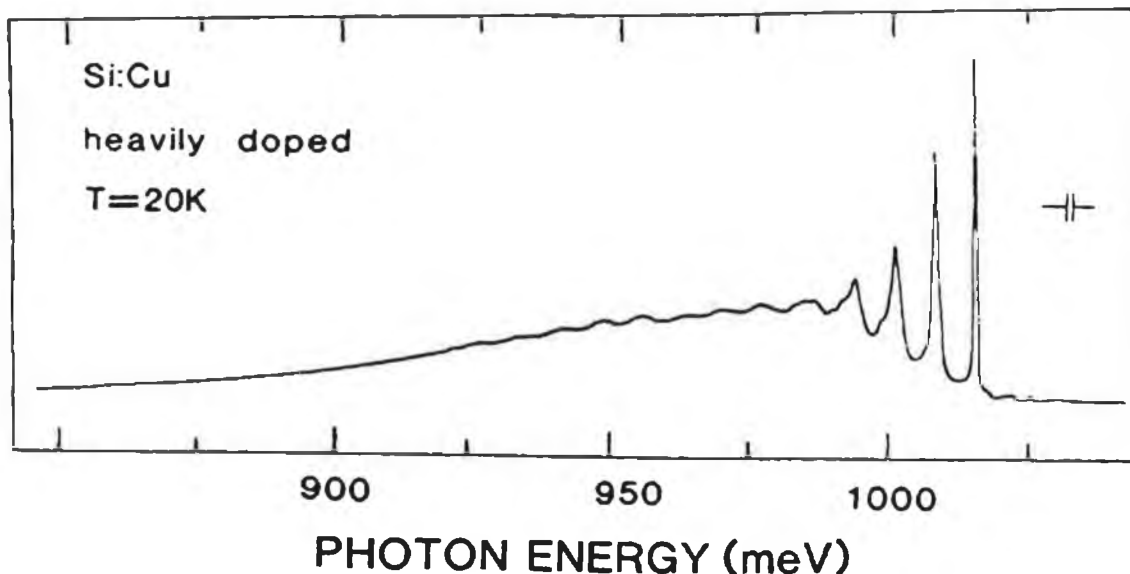

Fig.1.3 PL spectra of the 1.014 eV copper related system.

The other group of TM-related spectra, (see Fig. 1.4) including Cr-B, Cr-Ga, Mn_4 and V, are characterised by low absolute intensities, weak phonon coupling, and complex ground state structures, and are thought to arise from capture luminescence at deep centres. The optical transitions of all spectra, except V, take place between shallow effective mass like states 5 to 30 meV below the CB and the

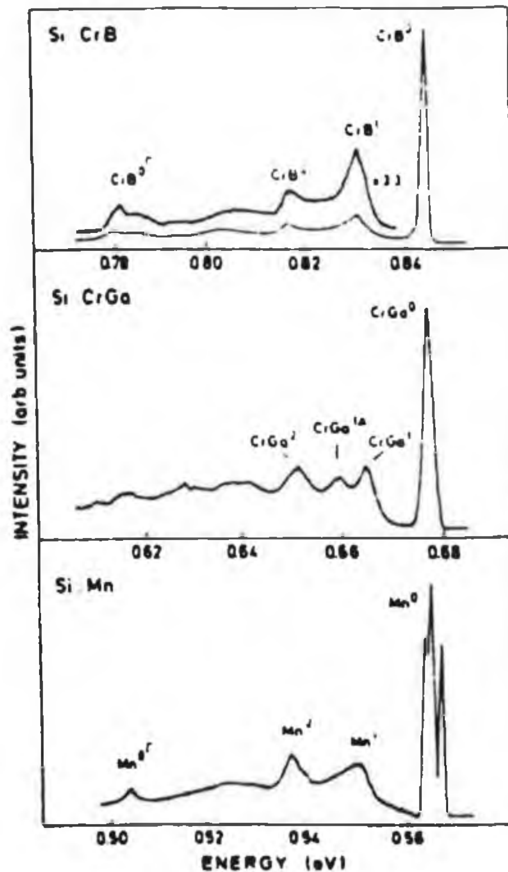

Fig. 1.4 PL spectra of Si:Cr-B, Si:Cr-Ga & Si:Mn (taken from Conzelmann (1987)).

ground state of a donor or a pseudo-donor in the case of IBE's. The occupancy of the 3d levels in the TM atom is thought to be of great importance in these defects. Theoretical studies of 3d level schemes (Watkins 1983) have predicted a ladder of TM states within the band gap but so far no luminescence lines from such intra d-shell transitions have been confirmed, Kleverman (1988) has reported lines in absorption spectra of Si:Ag that he ascribes to internal transitions within the 3d shell. Hangleiter (1985) has proposed some sort of excitonic Auger process to explain their lifetime behavior, but corraborative evidence has yet to be produced. This explanation is not at odds with Conzelmann's suggestion for the group 1 TM- related defects since the group 2 centres are not thought to be of an isoelectronic nature.

A study of the details of the phonon sidebands in the spectra

provides additional inportant information. Sauer and Weber (1983) suggest that, regardless of what group the PL centre falls into, it is solely the interstitial metal that is responsible for the local mode phonon replicas.

They argue that the interstitial TM of mass m_i moves in a harmonic potential and the phonon energies can be predicted if the strength of the potential barrier is known. Using the diffusion barrier H_m as a measure of the coupling strength of the TM to the surrounding Si atoms and the phonon energy of the Cr-B centre as a standard Conzelmann (1987) was able to predict the phonon energies of the different 3d complexes to a surprisingly good level of agreement with experimental evidence. The equation he uses is given in Eq. 1.2.

$$\omega_{th} = \omega_{CrB} \left[\left(H_{m_i} / H_{m_{Cr}} \right) . \left(m_{Cr} / m_i \right) \right]^{1/2} \qquad (1.2)$$

This implies that the substitutional partner takes no part in the phonon interaction. This model was also successfully applied to other PL centres involving elements on interstitial sites such as the Li_4 cluster (Canham 1983) and a Au-related centre (Thebault 1983). It is as a result of this phenomenon that the phonon energies of most of the identified 3d PL centres lie in the same small energy region from 14.5 to 13 meV since they all have roughly similar atomic masses. This model does not work for TM centres with high complex stability (Mn_4) or that are fast diffusers (implying a lower than normal diffusion barrier such as the Cu-Cu defect). In these cases the defect binding energy and bond length become the important factors (Sauer 1983).

1.4 NON-OPTICAL STUDIES

It has been known for some time that the electronic properties of Si are greatly affected by the presence of interstitial and substitutional 3d TM impurities. The different charge states that they can have in the impurity state often gives rise to multiple deep levels in the band structure of the host crystal. A defect that can create both

IMPURITY	HOST TYPE	IDENTITY	EN-LEVEL (eV)	REF.	REMARKS
Fe	i,n	Fe_i^o		98	
Fe	p	Fe_i^+	$E_v+.4$	98,71	
Fe	p	$(Fe-B)^o$	$E_v+.1$	98,6	
Fe	p	$(Fe-B)^o$	$E_v-.29$	6	
Fe	p	$(Fe-B)-Fe_i^+$		98	Band gap illumin.
Fe		$(Fe_sV)^+$		71	<111> symm.
Fe		$(Fe_i)_4$		71	<111> symm.
Mn	i	Mn_i^-		98,1	
Mn	i	Mn_i^o	$E_c-.42$	98,1	fast quench
Mn	i,n,p	$(Mn_i)_4^o$	$E_c-.54$	98,1	slow quench
Mn	i	$(Mn_i)_4^o$	$E_c-.28$	19	E.P.R.
Mn	i	$Mn^{-/o}$	$E_c-.13$	19	controlled
Mn	i	$Mn^{o/+}$	$E_c-.45$	19	Hall
Mn	i	$Mn^{+/++}$	$E_v+.3$	19	measure-
Mn	p	(MnB)	$E_c-.54$	19	-ments
Mn	p,n	(Mn-Cu)		28	slow cool
Cr	p	Cr_i^o		98	T < 6K
Cr	p	Cr_i^+		98	
Cr	p	Cr_i^-		15	
Cr	p	(Cr-B)	$E_v+.27$	98,15	E_g illum.
Pt	p	Pt_s^o	$E_c-.29$	74	photo-EPR
Cu		(Cu-Cu) ?	$E_v+.1$	100,39	
Cu		-Cu ?	$E_c-.24$	103	
Cu		-Cu ?	$E_v+.49$	103	
Cu		-Cu ?	$E_v+.52$	65	
Cu		-Cu ?	$E_v+.37$	65	
Cu		-Cu ?	$E_v+.24$	65	
Cu		-Cu ?	$E_v+.22$	54	
Cu		-Cu ?	$E_v+.41$	54	
Ni	i	Ni_i^+		98	v. weak
Ni	i	Ni_s		98	additnl. defect involved

Table 1.4 Reported EPR & DLTS systems in silicon

donor and acceptor levels in a crystal is termed an *amphoteric impurity.* One such example is Mn which gives rise to neutral, acceptor and donor levels in Si (Czaputa 1983, Weber 1983, Abdurakhmanov 1985).

The first in depth studies on TM levels in Si were done in EPR by Ludwig and Woodbury (1962) and since then with the development of other non-optical measurements techniques such as DLTS, ENDOR and TSCAP, many other deep states have been uncovered and identified. Some of these are listed in Table 1.4.

Despite the wealth of observed deep levels, theoretical modeling of such defects in agreement with L & W were not particularly successful until Hemstreet (1977) used an X_α scattered wave cluster method to accurately predict some of the levels produced by substitutional Cr, Co, Ni, Cu & Zn. Problems arose in its inability to account for charge state effects. DeLeo et al. (1981) using a similar model had some success calculating ground state levels for interstitial 3d impurities in good agreement with DLTS data (Weber 1978) especially for the (o/+) levels in Cr, Mn and Fe and for the (-/o) level in Mn but failed to explain the (o/+) level in V and predicted an unobserved (-/o) level for the Fe.

The confusion was further increased when Zunger et al. (1982, 1983) neglecting the cluster method in favour of a Green's function with a self interaction correction to lower the energy of the occupied orbitals in proportion to its degree of localisation, correctly predicted an e-t_2 splitting of 0.1 eV for Fe_i^o which exactly matched DeLeo's calculated value despite conflicting bases for both models.

So far, one consistent model that satisfactorily predicts the behaviour of interstitial and substitutional 3d impurities in Si has failed to emerge despite further studies using both of the above methods (Beeler 1985, Katayama-Yoshida 1984).

1.5 CONCLUDING REMARKS

From the preceding sections it is clear that the behaviour of TM atoms in Si is far from well understood. There is a large body of conflicting data concerning the electrically measured energy levels of interstitial and substitutional TM atoms while the configuration of most TM related PL centres remains unknown. In fact the only centre that has been identified with any degree of certainty is the 1014 meV Cu-Cu centre (Weber 1983) and even in this case it remains unclear whether the structure is Cu_i-Cu_s, Cu_i-Cu_i or if some other TM impurity possibly Fe is involved.

Since Ludwig and Woodbury had already shown that acceptors played a major role in the formation of many of the TM related EPR centres in silicon especially for the substitutional acceptor - interstitial donor defects, our group decided to examine Si:Zn and Si:Zn-TM (where TM is some other transition metal) in PL because zinc acts a deep double acceptor in silicon. Zinc is also the last of the 3d TM's and with its full d-shell has been somewhat neglected in recent research in favour of elements with partially filled shells. Double acceptors act much as expected in germanium but as a rule are not well behaved in silicon. Since zinc is no exception it was hoped that we might also gain some useful insight to explain its behaviour.

CHAPTER 2: BASIC THEORY

2.1 BAND THEORY

If we solve the Schrödinger equation for an isolated single atom we get a series of solutions that can be represented as discrete energy levels lying within a potential well. If two similar atoms are brought sufficiently close to one another their electronic wave functions will overlap. In order to satisfy Pauli's Exclusion Principle all the spin paired electrons acquire energies slightly different from their original isolated values. The energy spectrum of such a system therefore consists of a series of discrete doublets. The amount of splitting is dependent on the inter-nuclear distance and on the type of orbitals overlapping, with the 1s orbital splitting smaller than the 2s splitting which is smaller than the 2p splitting , etc.

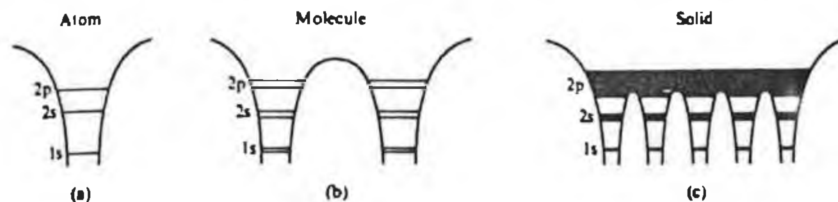

Fig. 2.1 Creation of band structure within semiconductors. The evolution of the energy spectrum of Li from an atom (a), to a molecule (b), to a solid (c).

In Fig. 2.1 we can see how if we extend this argument to N similar atoms brought within interacting distance of each other, they give rise to 2N electrons of the same orbital type occupying 2N different electron states. This thereby creates N sublevels that are so closely spaced that they can be considered to coalesce into one continuous energy band. The regions separating the energy bands are termed *forbidden energy bands.* It is the magnitude of this band gap energy E_g and the relative availability of electrons that determines

whether a solid is a metal, a semiconductor or an insulator. In general at zero Kelvin a semiconductor has a completely full lower energy band - called the *Valence Band* (V.B.) - separated from a completely unpopulated higher energy band - called the *Conduction Band* (C.B.) - by a band gap of less than 5 eV. In metals the V.B. and C.B. overlap (alternatively they may have a partly filled C.B.) allowing the electrons from the lower energy band to move easily into the higher, less densely populated band and thus the material exhibits high electrical conductivity.

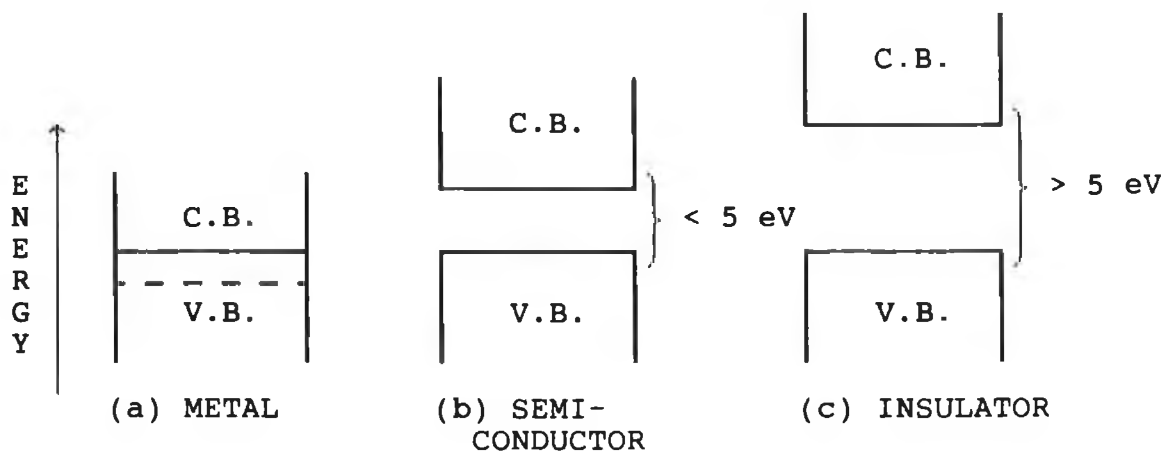

Fig. 2.2 Simplified band structure of different types of solids

In semiconductors the band gap is of such a magnitude at room temperatures electrons in the lower energy band can be excited thermally up into the C.B. where they can move about freely thus giving the solid some limited electrically conductive properties. Insulators, on the other hand, have much larger band gaps which means thermal processes in the crystal can not supply sufficient energy to the V.B. electrons to enable them to cross the gap, leaving the C.B. permanently unpopulated, with the result that the conductivity always approaches zero.

2.2 BAND SHAPE

The behavior of an electron travelling through a crystalline solid can be determined by solving the Schrödinger equation for a periodic or Bloch potential.

$$\left[-\frac{h^2 . \nabla^2}{8\pi^2 m} + V(\underline{r}) \right] \psi(\underline{r}) = E.\psi(\underline{r}) \qquad (2.1)$$

where $V(\underline{r})$ has the same translational symmetry, and hence the same period, as the real lattice. The solutions to Eq. 2.1 are called Bloch states and have the form :

$$\psi_k(\underline{r}) = e^{i.kr}.U_k(\underline{r}) \qquad (2.2)$$

where k is a vector quantity related to the momentum of the electron and $U_k(\underline{r})$ is a periodic function which also has the same translational symmetry as the real lattice. Mathematically speaking the electron travelling through a crystal behaves like a plane wave of vector k and consequently it has a de Broglie wavelength and momentum that conform to the equation :

$$P = \hbar k \qquad (2.3)$$

Substituting for Bloch states in Eq. 2.1 and re-arranging we end up with an eigenvalue equation which is easily solved. We find that for each value of k there are an infinite number of discrete energies E_{1k}, E_{2k},... These energies vary continuously as k is varied over its range of values, as is illustrated in Fig. 2.3

These discrete energy levels bear a one to one correspondence with the energy bands discussed in the previous section. Each energy band satisfies the following symmetry properties :

(1) $E_{n,(k+G)} = E_{n,k}$

(2) $E_{n,-k} = E_{n,k}$

(3) $E_{n,k}$ has the same rotational symmetry as its real lattice.

where G is any reciprocal lattice vector.

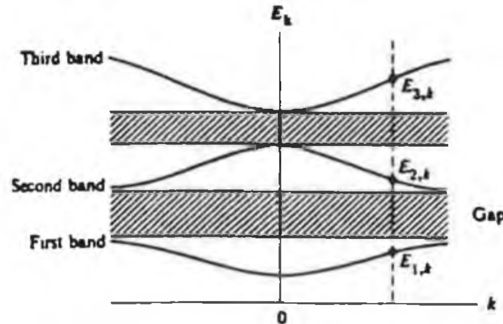

Fig. 2.3 Energy bands and gaps. The cross-hatched regions indicate energy gaps.

Further study reveals that the band structure of any crystalline solid need only be defined for the first Brillouin zone since it is repeated in the higher zones. Combining this with the three rules given above makes it necessary to define the band structure only for a very small fraction of the first Brillouin zone ($1/48^{th}$ in the case of Si).

Since the internuclear distance varies with crystal direction, so also will the band structure. Equivalently we say the band structure varies with wave vector k giving them a curved appearance in k-space. One consequence of this is that some crystals, depending on the symmetry of their lattice, will have their CB minimum and VB maximum at different points in k-space . These substances are called *Indirect Gap* semiconductors and the band structure of 2 such crystals silicon and germanium, is given in Fig. 2.4. If the maximum of the VB and the minimum of the CB lie at the same value of k in k-space then the crystal is termed a *Direct Gap* semiconductor. A table of direct and indirect gap semiconductors is given in Table 2.1.

Electrons can be excited from the V.B. across the energy gap into the C.B. by electrical, optical or thermal processes. The properties of vacant orbitals in an otherwise filled band are very important in semiconductor physics. Vacant orbitals at the top of the valence band are generally

(a) (b)

Fig. 2.4 Band structure of Si (a) & Ge (b) plotted along the [100] & [111] directions respectively.

called *holes.* A hole acts in an applied electric or magnetic field as if it has a positive charge e^{+}.Both electrons and holes when in the presence of an applied field behave as if their masses were different from the no field situation. We say they have an effective mass m^{*} given by ;

$$\frac{1}{m^{*}} = \frac{4\pi^{2}}{h} \cdot \frac{d^{2}E}{dk^{2}} \tag{2.4}$$

In Ge and Si holes near the band edges are characterised by two different effective masses (so called light and heavy holes) formed from $P_{3/2}$ electronic states while a third hole

state (split off) is created by the L-S interaction between the hole states. If the crystal purity is high enough the electron and hole can often attract each other to form a short lived quasi-stable state called *an exciton*. The binding energy of these excitons is quite small, of the order of 0.01 eV usually, giving rise to an energy state lying just below the C.B. edge as shown in Fig. 2.5.

SEMI CONDUCTOR	TYPE	BAND-GAP* (eV)	GAP TYPE
C	IV	5.48	i
Si	IV	1.17	i
Ge	IV	0.74	i
AlSb	III-V	1.70	i
AlAs	III-V	2.22	i
AlP	III-V	2.52	i
GaP	III-V	2.34	i
GaN	III-V	3.47	d
InP	III-V	1.42	d
InAs	III-V	0.42	d
InSb	III-V	2.35	d
ZnO	II-VI	3.44	d
ZnS	II-VI	3.80	d
ZnSe	II-VI	2.80	d
ZnTe	II-VI	2.38	d
CdS	II-VI	2.58	d
CdSe	II-VI	1.84	d
CdTe	II-VI	1.60	d

* band gap measured at room temperature

Table 2.1 Energy gaps and gap types of various semiconductors

As can be seen from Fig. 2.5, closer examination of this excitonic level beneath the C.B. reveals not one but a whole series of levels. These levels are easily explained if we think of the exciton as consisting of an electron and a hole revolving about a common centre of mass, forming a basic

hydrogenic system which has a series of excitonic ionisation energies given by ;

$$E_x = -\frac{m_r^* q^4}{2h^2 \varepsilon n^2} \quad (2.5)$$

where ε in this case is the relative permitivity of the host material.

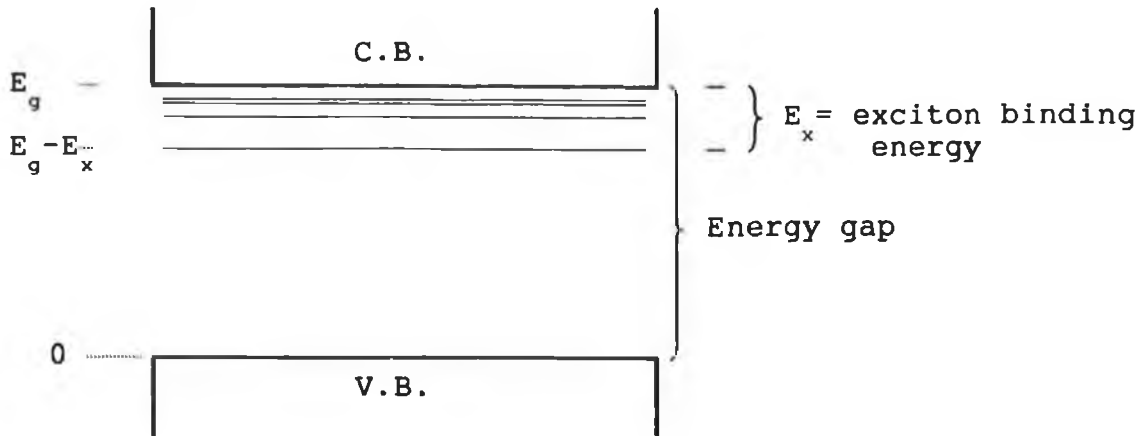

Fig. 2.5 A hydrogenic series of excitonic states in the band gap

where n is an integer ≥ 1 and m_r^* is the reduced mass of the exciton

i.e.
$$\frac{1}{m_r^*} = \frac{1}{m_e^*} + \frac{1}{m_h^*} \quad (2.6)$$

The C.B. edge is the limit of the hydrogenic series i.e. n = infinity.

2.3 IMPURITY STATES

Impurities can interact with the lattice in several ways. If the impurity replaces a constituent atom and provides the crystal with one or more extra electrons than the atom that it replaces then it is called *a donor impurity*

since it can be considered to donate an electron to the crystal band structure. Donors form impurity states within the band gap usually just below the C.B. (although deep donors can form states near to the V.B.)

If, on the other hand, the impurity has one less valence electron than the host atom it is called *an acceptor* and it

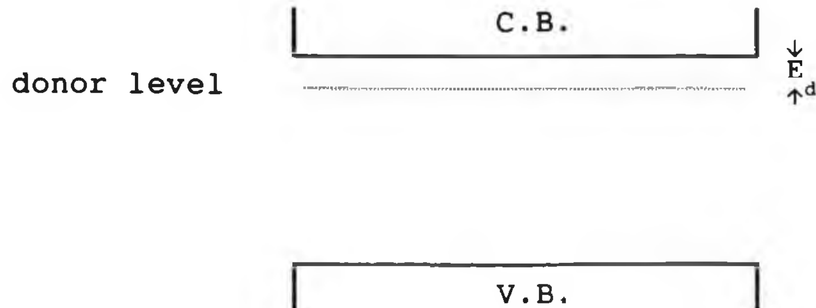

Fig. 2.6 A shallow donor level in the forbidden band gap

corresponds to the creation of an additional hole in the V.B. Accordingly, acceptors generally create impurity states just above the V.B.

If the impurity atom lodges in an interstitial site some or all of its outer-shell electrons are available for conduction and so it can create another donor level. Lattice site vacancies often combine with interstitial impurities to form semi-molecular complexes that can act as either donor or acceptor.

Since the common donor and acceptor levels usually lie relatively close to the band edges they are termed *shallow*

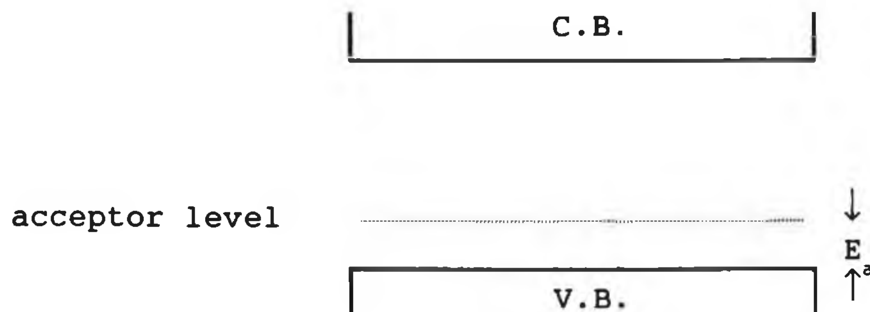

Fig. 2.7 A shallow acceptor level in the forbidden band gap

defects Other defects such as those caused by transition metal impurities form levels deep inside the forbidden energy gap and such levels are called *deep defects.*

2.4 PHONONS

Thermal energy in crystals is usually exhibited as lattice vibrations. Early investigations into the specific heat capacity of crystals revealed that only lattice vibrations of certain frequencies can propagate through the structure. In effect the frequency spectrum of the lattice vibrations is not continuous but quantized. The quantum of vibration is called a *phonon* and by analogy with the photon it has energy E given by ;

$$E = \hbar\omega \tag{2.7}$$

and by De Broglie's hypothesis can be considered to possess some particle-like properties. Its momentum is given by ;

$$P = \hbar k \tag{2.8}$$

As a direct consequence of this, an elastic sound wave propagating through a crystal, or a lattice vibration can be thought of as a stream of phonons carrying the energy and momentum of the wave.

2.5 OPTICAL ABSORPTION AND LUMINESCENCE

Absorption and luminescence measurements yield the energy levels of the defect, information about the associated wavefunctions , the identity of the defect symmetry under favorable conditions and in the case of some shallow defects impurity concentrations can also be determined. At very low temperatures only the ground level of the defect is appreciably occupied and so absorption spectra give the energy levels directly. The polarization properties of the

states can yield further information about the site symmetry. Often luminescence is excited by absorption of light of wavelength lying in a particular range. This range may correspond to (1) a transition between energy levels of localised states of the defect responsible for the luminescence; (2) a transition from a localised state to band states of the host state; (3) a transition from VB states to CB states; (4) or a transition between states of another defect called a *sensitizer* , which transfers its energy to the luminescent defect. The minimum detectable defect concentration is usually much lower in luminescence than in absorption since there is no large background light level present to reduce the signal to noise ratio. A third type of spectrum which is often useful is the luminescence excitation spectrum which is a plot of the luminescence intensity at a fixed luminescence wavelength versus the wavelength of the excitation source. In general the excitation spectrum corresponds to a part of the absorption spectrum (Watts 1977).

Optical band to band absorption is the process whereby an electron in the V.B. can be excited into the C.B. by absorbing a photon from incident radiation. For this to happen the photon energy must clearly be greater or equal to the band gap energy i.e.:

$$\nu \geq E_g/h \tag{2.9}$$

The threshold frequency arrived at when the inequality is replaced by an equals sign is termed *the absorption edge* of the crystal. In all transitions the total energy and momentum of the electron-photon system must be conserved i.e.:

$$E_f = E_i + h\nu \tag{2.10}$$

and

$$k_f = k_i + k_{ph} \tag{2.11}$$

where $h\nu$ is the absorbed photon energy and k_{ph} is its wave vector. However since photons in the optical and infra-red

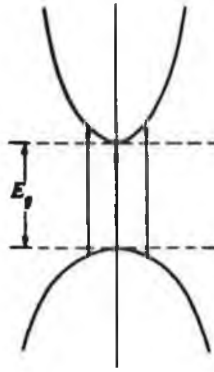

Fig. 2.8 The fundamental absorption process in semiconductors.

regions of the electromagnetic spectrum have negligibly small wave vectors Eq. 2.11 reduces to :

$$k_f = k_i \tag{2.12}$$

These selection rules only allow vertical transitions in k-space between the V.B. and the C.B. as shown in Fig. 2.8.

Electrons in indirect gap semiconductors cannot make a direct transition from the top of the V.B. to the bottom of the C.B. without violating Eq. 2.12. Transitions can still occur however, as a two step process involving the absorption of a photon and either the emission or absorption of a phonon (Fig. 2.9). The phonon energy is small enough to leave Eq. 2.10 valid but its appreciable momentum is sufficient to satisfy Eq. 2.12. Although a broad spectrum of phonons are available, only those with the required momentum are usable.

Luminescence is the reverse process of absorption. An electron excited to a higher energy state makes a transition down to an empty lower energy state emitting all or most of the energy difference between the states as electromagnetic radiation.

The main prerequisite for emission is that the system not be at equilibrium. For this to happen requires some form of excitation to be supplied, either electrically (electroluminescence), by optical absorption (photo - luminescence) by electron beam excitation (cathodo -

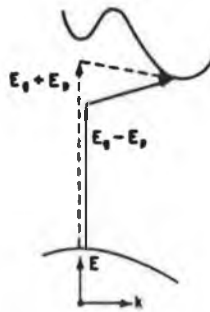

Fig. 2.9 Indirect transition involving a momentum conserving phonon interaction.

luminescence), by mechanical excitation (triboluminescence) or by chemical reaction (chemiluminescence).

If we consider some semiconductor that has some form of excitation acting upon it forming electron-hole pairs then we find that if the material is sufficiently pure, the pairs form excitons which eventually recombine emitting a narrow spectral line. This process is called *Radiative Recombination.*

The emitted photon energy in direct gap materials is given by :

$$h\nu = E_g - E_x \tag{2.13}$$

: as illustrated in Fig. 2.10 (a).

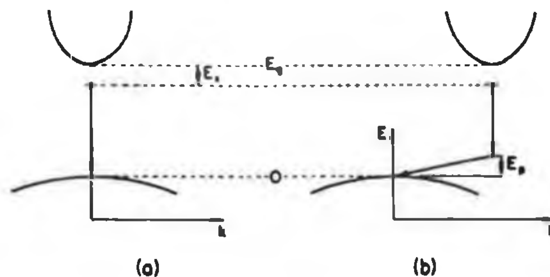

Fig. 2.10 Exciton recombination :(a) direct; (b) indirect

Since excited excitonic states can exist, the excitonic emission spectrum should consist of a series of narrow lines corresponding to higher energy states. Such lines have been observed in GaAs (Gilleo 1968) in absorption for the $n = 1$ and 2 states. Higher order lines are difficult to observe since the luminescence intensity decreases as n^{-3} (Elliott 1957).

The situation in indirect gap materials is somewhat different. The selection rules governing the conservation of momentum dictate that one or more phonons be emitted to complete the transition as indicated in Fig. 2.10 (b).

Here the photon energy is described by :

$$h\nu = E_g - E_x - m.E_{ph} \quad .... \quad m \in \mathbb{Z} \qquad (2.14)$$

where m is the number of phonons emitted in the transition.

Sometimes a reverse process can occur where the defect absorbs a lattice phonon before making a transition down to the ground state. This results in a broad feature at higher energies in the optical spectrum and is termed an *Anti-Stokes phonon replica*, which usually appears at higher sample temperatures where the probability of capturing a phonon is greater.

Direct gap materials can also couple phonons to transitions in much the same manner.

2.6 BOUND EXCITONS

Neutral impurity states within the energy gap of the semiconductor can often attract or trap an electron (or hole) as a result of some central cell potential such as electronegativity or local strain about the defect. This electron (hole) can then coulombically attract a hole (electron) to form an exciton bound to the defect. This type of exciton is called a *bound exciton* (B.E.).

Radiative recombination at excitons bound to impurity sites is characterised by lines of narrow spectral width, at lower

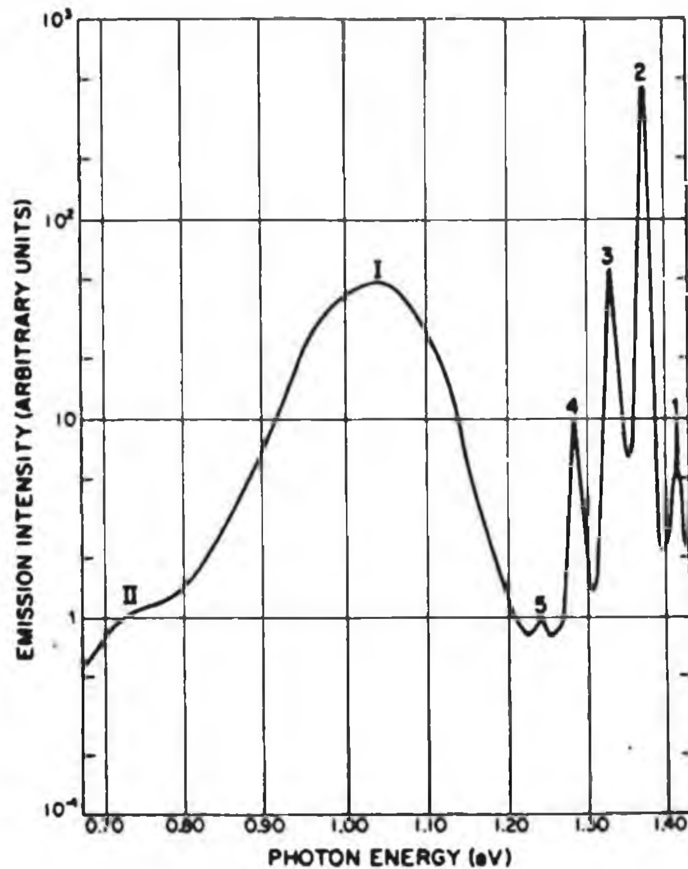

Fig. 2.11 PL spectra of InP at 6 K (taken from Turner et al. 1963).

photon energies than free exciton (F.E.) luminescence. Photoluminescence (P.L.) from F.E.'s and B.E.'s can occur simultaneously in the same material, in which case each can be identified by their characteristic linewidths and energies. For example the linewidth of a B.E. feature in GaAs is 0.1 meV compared to 1 meV for the F.E.line in the same material (Elliott 1968).

A P.L. spectrum of InP is given in Fig. 2.11 (Turner et al. 1963) . The emission peak labelled 1 is interpreted to be due to F.E. recombination while lines 2 to 5 are attributed to B.E. recombination assisted by 0,1,2 and 3 phonon emission. The spacing between the respective B.E. features is 43 meV which corresponds to the LO phonon in InP. The broad spectral features labelled I and II arise through

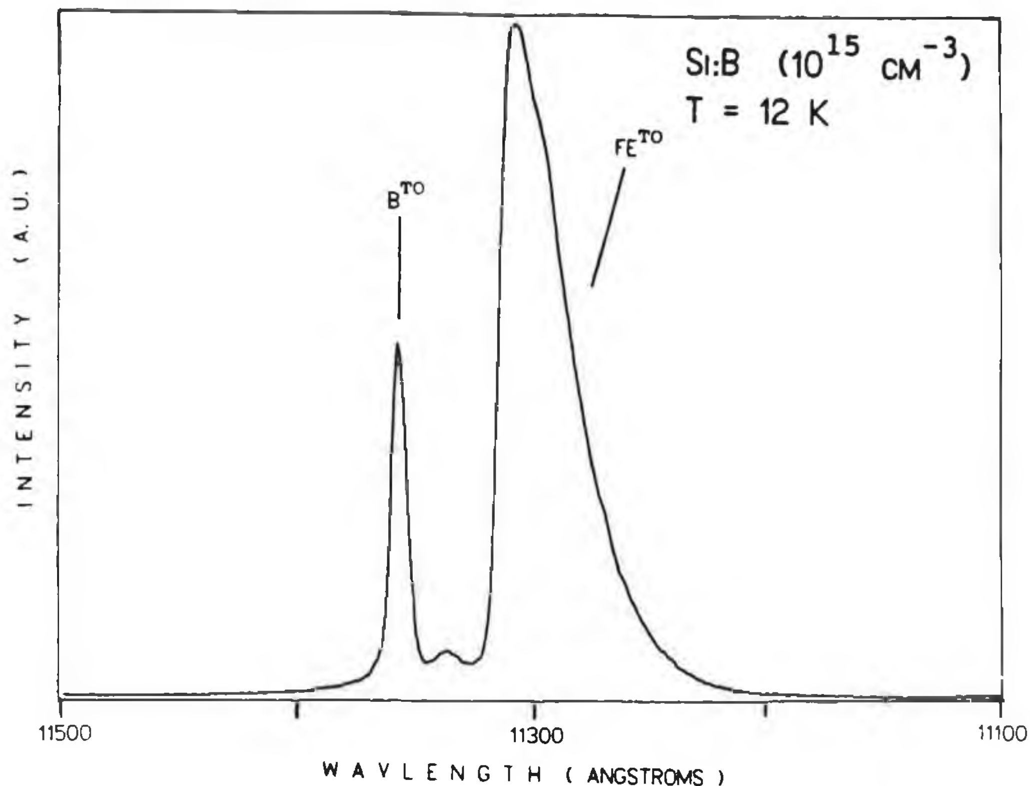

Fig. 2.12 Comparison of linewidths between free exciton and bound exciton PL features in boron doped silicon. Both features are transverse optical (TO) phonon replicas of the respective recombination processes.

non-excitonic processes. The narrower line width of bound exciton features is also illustrated in Fig. 2.12 for phonon assisted PL features in Si:B. Since silicon is an indirect gap semiconductor no zero phonon luminescence is observed for the free exciton recombination process . In the diagram we see the free exciton TO (LO) phonon assisted feature alongside a boron TO assisted peak . The obseved linewidths are clearly different.

2.7 THE VALLEY-ORBIT INTERACTION

If an electron were bound to a donor in free space the absorption spectrum of this system would reflect its' hydrogen - like nature and consist of a hydrogenic series of

excited states. In a crystal however the band structure and crystal field combine to perturb this system. For example, silicon and gallium phosphide have conduction band minima lying along the <100> direction in k-space which leads to a six-fold degeneracy. Fortunately the crystal field created by

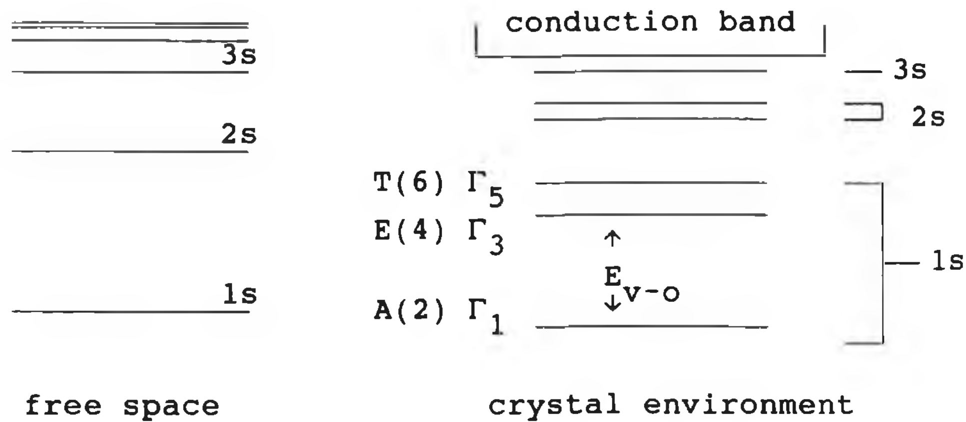

Fig. 2.13 The effect of a crystal environment on the absorption spectrum of a hydrogenic system leading to the valley orbit interaction.

the lattice removes some of the degeneracy and the states split into three groups that transform as A, E and T representations of the T_d symmetry group. When this is combined with spin considerations we are left with a Γ_1, a Γ_3 and a Γ_5 state that form a multiplet that corresponds to the 1s level in the free-space absorption spectrum.

This situation is illustrated in Fig. 2.13. The Γ_1 level has a spherically symmetric electron distribution function and the electron is localised about the defect core to a much greater extent than the Γ_3 and Γ_5 states which both have nodes in their distribution function at the core. As a result the Γ_1 state is much lower in energy than the other two states and this difference in energy is called the valley - orbit splitting and is represented by E_{v-o} in Fig. 2.13. The numbers in brackets in the figure are the degeneracy of each state. The magnitude of the valley - orbit splitting varies widely in silicon from as little as 1.8 meV for the lithium

donor (Faulkner 1969) to as much as 42.5 meV for the 1060 meV zinc related defect reported by Henry et al. (1988). This interaction affects the 1s state to the greatest extent but can also be observed in the higher states but with diminishing magnitude.

2.8 ISOELECTRONIC CENTRES

An isoelectronic impurity is a substitutional impurity with the same number of valence electrons as the atom of the host crystal that it replaces, for example C or Ge in silicon. A direct consequence of this is that it is always electrically neutral but the difference in its electronic structure can be sufficient to create an impurity state within the the gap. Such defects were first detected in ZnTe:O (Dietz 1962) and in GaP:N (Dean 1963); since then isoelectronic defects have been reported in most semiconductor crystals. The defect need not be a single impurity atom and more complex molecular isoelectronic centres have been reported such as the ZnO and CdO defects in GaP (Henry et al. 1967). In 1966 Hopfield et al proposed a model for isoelectronic traps that explains much of their observed behaviour. The trap can be considered to be attractive to either electrons or holes but since the defect is electrically neutral the binding force is thought to arise from some short range force such as electro-negativity or local strain about the defect site. After binding the initial electron or hole this in turn captures a carrier of opposite charge via its Coulombic potential. Cohen and Sturge (1977) confirmed this model for the near-neighbour N_P - N_P in GaP using photoluminescence excitation (PLE) to scan the absorption spectrum of acceptor-like excited states of the hole which was shown to be bound in the Coulombic potential of a highly localised electron. An obvious distinction between isoelectronic centres can now be made on the basis of which free-carrier is bound first. They are normally referred to as an isoelectronic donor if they bind the hole first and isoelectronic acceptors if the electron is the tightly bound

carrier.

It was only at the end of the 1970's with the developement of the germanium detector that isoelectronic traps were identified in silicon (Vouk 1977, Weber 1979). Since then many others have been reported. In contrast to GaP no point isoelectronic traps have been discovered. Canham (Ph. D. thesis 1983) has suggested that the more covalent nature of the silicon lattice prevents hole traps arising at Ge, Sn or Pb substitutional sites while the impurity potential surrounding substitutional carbon seems insufficient to trap electrons.

The other major difference between IBE's reported in silicon and GaP is the inability to conclusively identify the chemical constituents in the former. The main reason being that without isotope studies, identification must rely almost solely on doping studies which yield much better information for the compound semiconductors than they do for silicon.

2.9 LUMINESCENCE TEMPERATURE DEPENDENCE

The manner in which the total luminescence intensity of a PL system varies with changes in sample temperature gives detailed information on the excitonic environment of both the defect in question and of shallower levels arising at other defects in the sample. The PL spectra of most TM related defects consists of at least two zero phonon lines (ZPL's), so for the sake of simplicity let us consider a system giving rise to two levels as shown in Fig. 2.14.

$$N_2 = N_1 g_{21} \exp(-\Delta E/kT)$$

$$I(0) = N_1(0) f_1$$

$$N_{tot}(0) = N_1(0)$$

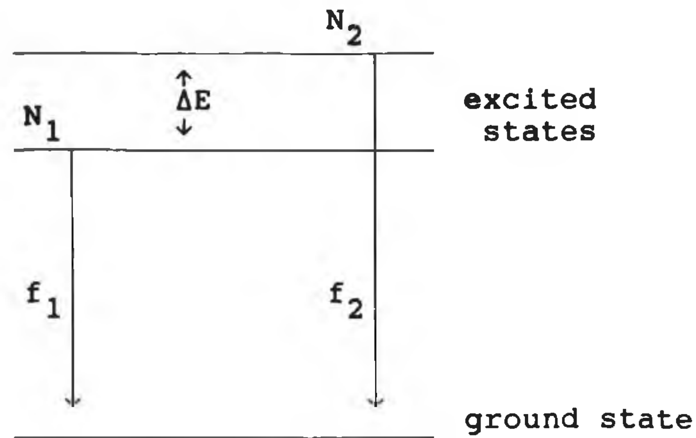

where ; N_i = the population of the ith level.
f_i = the transition probability of the ith level.
g_{21} = the ratio of the degeneracy of the second level to the first level.

Fig. 2.14 A simplified energy level diagram

$$N_{tot} = N_1 + N_2$$

$$= N_1(1 + g_{21}\exp(-\Delta E/kT))$$

$$I_{tot} = I_1 + I_2$$

$$= N_1 f_1 + N_2 f_2$$

$$= N_1 f_1(1 + f_2 N_2/f_1 N_1)$$

$$= N_1 f_1(1 + (f_2/f_1)g_{21}\exp(-\Delta E/kT))$$

at 0 K $\quad I_{tot} = I(0) = N_1(0)f_1$

at T K $\quad I_{tot} = I(T) = N_1(T)f_1(1 + (f_2/f_1)g_{21}\exp(-\Delta E/kT))$

$$N_1(T) = N_1(0)/(1 + g_{21}\exp(-\Delta E/kT))$$

$$\Rightarrow \quad I_{tot}(T) = \frac{N_1(0)f_1(1+(f_2/f_1)g_{21}\exp(-\Delta E/kT))}{(1+g_{21}\exp(-\Delta E/kT))}$$

$$\Rightarrow \quad I_{tot}(T) = \frac{I_1(0)(1+(f_2/f_1)g_{21}\exp(-\Delta E/kT))}{(1+g_{21}\exp(-\Delta E/kT))}$$

This last expression will be denoted from now on by $F_1(T)$ i.e.

$$\Rightarrow \quad F_1(T) = \frac{I_1(0)(1+(f_2/f_1)g_{21}\exp(-\Delta E/kT))}{(1+g_{21}\exp(-\Delta E/kT))} \qquad (2.15)$$

and it describes the behaviour of the intrinsic luminescence arising at the impurity levels created by the defects.

More than likely the TM related defect will not be the only defect type produced during the fabrication process. If some

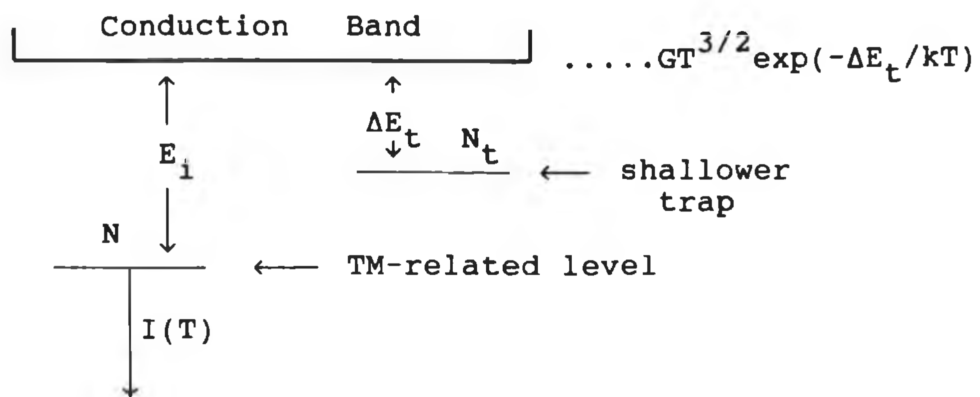

N_t = the total population in the other level.
E_t = the binding energy of excitons bound to the traps.
N = composite of N_1 and N_2 of the previous section.
E_i = the binding energy of excitons bound to the TM related defect.

Fig. 2.15 Schematic diagram representing the luminescence contribution from other traps in the samples.

of these other defects have excitons weakly bound to them, the probability is that they are more likely to dissociate by a thermal process than via radiative recombination. In

such a situation the excitons that decay thermally off the other traps become available for capture by the TM related PL system which results in an increase in the total intensity that cannot be accounted for by the $F_1(T)$ function.

Again for simplicity let us consider a case where all the different types of traps can be represented by a single level as shown in Fig. 2.15. We can think of the conduction band as acting as a pool of excitons available for capture by either level with both competing with each other. As the temperature increases the traps can no longer capture excitons since they are ionized off again almost immediately which means the fraction of shallow traps competing for the excitons decreases. The fraction competing is just that fraction left in the shallow level which Davies (1989) describes by the equation :

$$f = 1 / (1 + GT^{3/2}\exp(-\Delta E_t/kT))$$

where the $GT^{3/2}$ term describes the temperature dependence of the concentration ratio of band states to traps.
At $T = 0$, $f = 1$ which means all the traps are competing for exciton capture.

If we call the maximum value of intensity that the PL can have I_{max} then $I(T) = I_{max}$ only if there is no trapping from the shallower levels or if the temperature is sufficiently high that all the traps are ionized. For real values of T the intensity would behave according to the following equation deduced by Davies (1989).

$$\frac{I(T)}{I_{max}} = \frac{1}{1 + r.f} \qquad (2.16)$$

where r is the branching ratio between luminescence centres and shallow traps for exciton capture.

Clearly as r increases the dominance of the shallower traps increases. We define :

$$F_{trap}(T) = \frac{I_{max}}{1 + r.f}$$

where $$f = 1 / (1 + GT^{3/2}\exp(-\Delta E_t/kT))$$

Sometimes a situation might exist where a shallow trap transfers its' excitons directly into the luminescence level without losing them to the band first. In this case then the $F_{trap}(T)$ function remains the same except that the density of states term in the equation for f is replaced by a factor describing the ratio of the concentrations of traps and luminescence centres and ΔE_t is replaced by the activation energy for the energy transfer.

If the temperature is increased further then the excitons on the TM related defect begin to thermally decay before they have a chance to recombine radiatively leading to an overall decrease in total intensity. If we denote the number of luminescence centres with excitons bound to them by N_i^x, the number of centres with the exciton ionized thermally off by N_i^o and the total number of luminescence centres by N_i then :

$$I(T) = N_i^x(T)f^x$$

where f^x is the probability of radiative recombination.

$$I(T) = N_i f^x / (1 + GT^{3/2}\exp(-E_i/kT))$$

$$= I_i(0)/(1 + GT^{3/2}\exp(-E_i/kT))$$

if we define

$$F_{decay}(T) = 1/(1 + GT^{3/2}\exp(-E_i/kT)) \qquad (2.17)$$

then we find the total intensity of the luminescence band is given by :

$$I_{tot}(T) = I_o \cdot F_1(T) \cdot F_{trap}(T) \cdot F_{decay}(T) \qquad (2.18)$$

The role of direct non-radiative processes is not believed to make a significant contribution to the temperature dependence of bound exciton luminescence in silicon.

Thus a fit to any temperature dependent luminescence data would be in terms of the seven following parameters:

$$g_{21},\ G,\ F=f_1/f_2,\ r,\ \Delta E,\ E_t \text{ and } E_i$$

Since E_i is the ionization energy of the exciton bound to the defect this effectively corresponds to the binding energy of the more loosely bound excitonic component.

2.10 TEMPERATURE DEPENDENCE OF LUMINESCENCE DECAY TIMES

We now examine the effect of increasing temperature on the PL decay times. We adopt the same model as used in the analysis of the luminescence intensity, namely that illustrated in Fig. 2..16. The following notation applies :

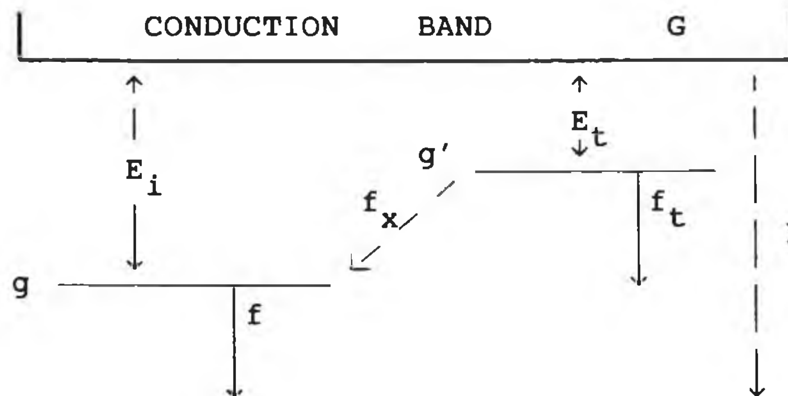

Fig. 2.16 Schematic representation of the effect of shallow traps transfering energy into a luminescence level.

f = the probability of exciton recombination at a luminescence centre.

f_t = the probability of exciton recombination at a shallow trap.

f_x = the probability of exciton transfer from a trap to a luminescence centre.

g and g' are the respective degeneracies of the PL

centres and traps

G and F denote the effective density of band states and the recombination probabilitiies of carriers released to the band respectively.

The total decay time of the traps is given by :

$$f' = f_t + f_x$$

We assume initially that $f_x = 0$ i.e. there is no transfer of energy from the traps to the luminescence centres. In this case the luminescence decay time is given by :

$$1/\tau = g.f$$

As the temperature increases, and in the absence of any excited states, a small change in τ is expected as additional phonon assisted transitions take place. At temperatures such that the excitons become thermally dissociated from the centres, a rapid decrease in τ can be expected. The temperature dependence of such a system is formally expressed by the equation :

$$\frac{1}{\tau} = \frac{gf + GFT^{3/2}\exp(-E_i/kT)}{g + GT^{3/2}\exp(-E_i/kT)} \qquad (2.19)$$

Following an excitation pulse the PL transient can be described by :

$$I(t) = I_o\exp(-t/\tau) \qquad (2.20)$$

In a system where exciton transfer from shallower traps is occurring the luminescence transient following an excitation pulse may be a more complex function of time. The transient will consist of at least two components. The first being that resulting from centres directly excited by exciton capture from the bands, while the second is produced by the donation of excitons from the traps. The first component will have a decay time τ governed by Eq. 2.20. The second component will show up in the transient only if the decay time of the traps

τ_t is longer than that of the luminescence centres. For our purposes this is the situation of interest.

Let N and N_t denote the concentration of luminescence centres and traps with excitons bound to them respectively. Using the definitions of f, f' and f_x we can write the following rate equations.

$$dN_t/dt = -N_t f'$$

and

$$dN/dt = -Nf + N_t f_x$$

The solutions to these are given by Reilly (Ph. D. thesis, appendix A.2, 1979) as :

$$N_t(t) = N_t(0).\exp(-t/\tau_t)$$

and

$$N(t) = A.\exp(-t/\tau) + B.[\exp(-t/\tau_t) - \exp(-t/\tau)]$$

In the measurement of the luminescence transient the intensity is proportional to N(t) so we find :

$$I(t) = A.\exp(-t/\tau) + B.[\exp(-t/\tau_t) - \exp(-t/\tau)] \quad (2.21)$$

The A and B parameters are a measure of the relative magnitudes of the components of the luminescence produced by direct capture and by exciton capture. The implication of this analysis is that a luminescence transient consisting of two (or more) components indicates the presence of some transfer mechanism in the material. Such transfer processes are invariably temperature dependent and substantial changes are to be expected as the temperature increases. An excellent example of such a system is discussed in section 5.2.3.

CHAPTER 3: UNIAXIAL STRESS & ZEEMAN SPECTROSCOPY

3.1 UNIAXIAL STRESS

Uniaxial stress spectroscopy (piezo-spectroscopy) is now well established as an experimental method to determine the symmetry group of a defect or to probe the vibronic properties of electronic structures in solids. The manner in which we expect different transitions to split under the application of uniaxial stress is well documented in many papers both for absorption (Kaplayanskii 1963) and photoluminescence (Davies 1982)

The theory behind this technique is straight forward and is outlined below.

3.2 THEORY

Either of two approaches may be used to fully describe the interaction of applied stress with impurity states arising from axial defects in crystals ; calculations with respect to *defect co-ordinates* or with respect to *crystal co-ordinates.* Both co-ordinate systems are equivalent and will be addressed in the following sections.

3.3 DEFECT CO-ORDINATES

Let us assume we have a transition between two states E_a and E_b. Under the action of stress the energy levels may take up new energy values as shown in Fig. 3.1.

We think of the original energy levels as being acted upon by some potential V. It is reasonable to assume that this potential has the same symmetry as the centre causing it. V adds an extra term to the Hamiltonian of the system.

$$H = H_o + V \tag{3.1}$$

where

$$V = a_1 S_{xx} + a_2 S_{yy} + a_3 S_{zz} + a_4 S_{yz} + a_5 S_{zx} + a_6 S_{xy} \tag{3.2}$$

$$S_{ij} = |P| . \cos (\hat{P}, i) . \cos (\hat{P}, j) \tag{3.3}$$

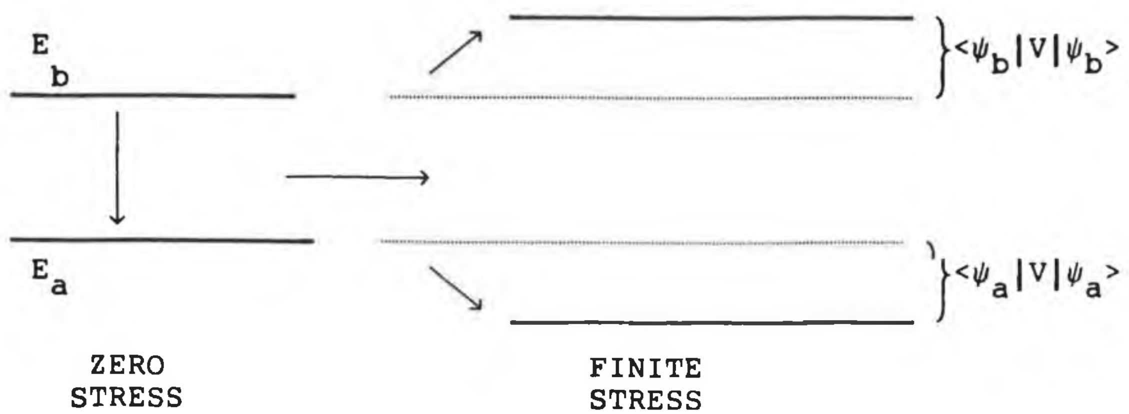

Fig. 3.1 The effect of stress on transitions between electronic states

where (P,i) is the angle between the stress direction $\hat{P}$ and the ith axis, $|\hat{P}|$ is the magnitude of the applied stress and the a_i are real constants.

We will now solve these equations for a defect of some particular symmetry. We will assume that the defect has C_{1h} monoclinic I symmetry. For the moment we will also assume that the states involved are *non-degenerate.* The original spectral line will change its' energy value by an amount Δ (see Fig. 3.1), where ;

$$\Delta = E_b - E_a + \langle\psi_a|V|\psi_a\rangle + \langle\psi_b|V|\psi_b\rangle \qquad (3.4)$$

For non-degenerate states the only non-zero matrix elements are those that transform as the totally symmetric, non-degenerate identity representation for that group. Table 3.1 is the character table for the C_{1h} group :

C_{1h}	E	C_2	
A	1	1	x^2 y^2 z^2, xy, x, y
B	1	-1	xz, yz, z

Table 3.1 Character table for the symmetry group C_{1h}

The S_{ij} components of V transform as their subscripts, which means that since we have specified that we are dealing with non-degenerate states we can rewrite Eq. 3.2 as ;

$$V = a_1S_{xx}+a_2S_{yy}+a_3S_{zz}+a_6S_{xy} \tag{3.5}$$

If we relabel the a_6 constant as a_4, and substitute Eq. 3.5 into Eq. 3.4 we get ;

$$\begin{aligned}\Delta = E_a - E_b - &[\langle\psi_a|a_1S_{xx}|\psi_a\rangle - \langle\psi_b|a_1S_{xx}|\psi_b\rangle] \\ - &[\langle\psi_a|a_2S_{yy}|\psi_a\rangle - \langle\psi_b|a_2S_{yy}|\psi_b\rangle] \\ - &[\langle\psi_a|a_3S_{zz}|\psi_a\rangle - \langle\psi_b|a_3S_{zz}|\psi_b\rangle] \\ - &[\langle\psi_a|a_4S_{xy}|\psi_a\rangle - \langle\psi_b|a_4S_{xy}|\psi_b\rangle]\end{aligned} \tag{3.6}$$

We can rewrite this equation as ;

$$\Delta = E_a - E_b - \delta \tag{3.7}$$

Where δ is termed the shift rate.

We must now calculate all possible non-equivalent monoclinic I centres and then calculate the values of S_{ij} for each one. The defect co-ordinates of each non-equivalent monoclinic I centre in a crystal with T_d symmetry is given in Table 3.2.

Care must be taken in calculating the values of S_{ij} to remember that all vectors involved are unitary vectors. The values of S_{ij} for all 12 monoclinic I defects under a uniaxial stress along the <100> axis have been calculated and are given in Table 3.3. It is clearly seen from this table that under <100> stress the 12 different defects split into 2 distinct sets, one of 4 and one of 8. Thus we would expect a spectral line arising from a transition between non-degenerate states at a monoclinic I defect to split into two distinct components when subjected to stress along the <100> direction, as shown in Fig. 3.2.

Centre no.	X co-ord.	Y co-ord.	Z co-ord.
1	001	110	110
2	$00\bar{1}$	110	$1\bar{1}0$
3	001	$\bar{1}10$	$\bar{1}\bar{1}0$
4	$00\bar{1}$	$\bar{1}\bar{1}0$	$\bar{1}10$
5	010	$\bar{1}01$	101
6	$0\bar{1}0$	101	$\bar{1}01$
7	010	$10\bar{1}$	$\bar{1}0\bar{1}$
8	$0\bar{1}0$	$\bar{1}0\bar{1}$	$10\bar{1}$
9	100	$0\bar{1}1$	$0\bar{1}\bar{1}$
10	$\bar{1}00$	011	$01\bar{1}$
11	$\bar{1}00$	$0\bar{1}\bar{1}$	$0\bar{1}1$
12	100	$01\bar{1}$	011

Table 3.2 The defect co-ordinates of all possible monoclinic I defects in a T_d symmetry crystal.

Centre No.	S_{xx}	S_{yy}	S_{zz}	S_{xy}
1	0	0.5	0.5	0
2	0	0.5	0.5	0
3	0	0.5	0.5	0
4	0	0.5	0.5	0
5	0	0.5	0.5	0
6	0	0.5	0.5	0
7	0	0.5	0.5	0
8	0	0.5	0.5	0
9	1	0	0	0
10	1	0	0	0
11	1	0	0	0
12	1	0	0	0

Table 3.3 The values of S_{ij} for all 12 monoclinic centres in a T_d symmetry crystal under a uniaxial stress along the <100> axis.

The relative intensities of the peaks can be calculated by assuming that the electric dipole of the defect lies along some particular direction - usually taken to be the z-axis of the defect. This done, the intensity is calculated by taking the square of the projection of the unitary vector lying along the direction of the electric dipole, onto the unitary vector lying in the direction parallel to the stress

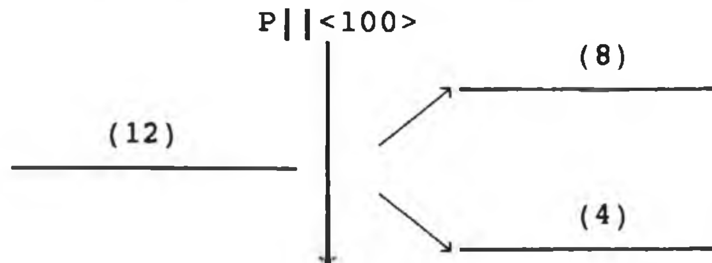

Fig. 3.2 Splitting of a non-degenerate monoclinic-I defect under <100> stress

Centre No.	π-Polarization Intensity π||<100>	σ-Polarization Intensity σ||<011>
1	1	1
2	1	1
3	1	1
4	1	1
5	1	1
6	1	1
7	1	1
8	1	1
9	0	2
10	0	0
11	0	0
12	0	2

Table 3.4 π and σ polarization intensity contributions from all the inequivalent monoclinic I centres under <100> stress

(to give the expected intensity under π polarized excitation), or perpendicular to the stress (to give σ polarization intensity). If the predicted intensities don't agree with the experimental results then more than likely the electric

dipole direction has been incorrectly chosen. Table 3.4 shows the predicted polarization intensity contributions from all the inequivalent monoclinic I defects in a T_d symmetry crystal under <100> stress.

We are now in a position to fully predict what would occur to such a defect under <100> stress. From Tables 3.3 and 3.4 we can see that the 12 inequivalent centres split into 2 groups with the following shift rates ;

$$\text{Group 1} : \delta_1 = 1/2\,(a_2 + a_3) \tag{3.8}$$

and

$$\text{Group 2} : \delta_2 = a_3 \tag{3.9}$$

Their relative polarization intensities ratios are ;

	π : σ
Group 1	8 : 8
Group 2	0 : 4

Table 3.5 polarization intensities for the <100> stress splitting.

The information given in equations 3.8, 3.9 and Table 3.5 is often displayed graphically as illustrated in Fig. 3.3

Fig. 3.3 Splitting and polarization intensities for a non-degenerate monoclinic-I defect under <111> stress

The S_{ij} values and polarization intensity contributions for stress in the <111> and <110> directions are calculated in the same fashion.

P||<111>

Group 1: $\delta_3 = 1/3(a_1 + 2a_3)$. (3.10)

Group 2 : $\delta_4 = 1/3(a_1 + 2a_2 - \sqrt{2}a_4)$ (3.11)

Group 3 : $\delta_5 = 1/3(a_1 + 2a_2 + \sqrt{2}a_4)$ (3.12)

Centre No.	S_{xx}	S_{yy}	S_{zz}	S_{xy}	π ||<111>	σ ||<110>
1	1/3	0	2/3	0	4/3	0
2	1/3	2/3	0	$-\sqrt{2}/3$	0	2
3	1/3	0	2/3	0	4/3	0
4	1/3	2/3	0	$\sqrt{2}/3$	0	2
5	1/3	0	2/3	0	4/3	1/2
6	1/3	2/3	0	$-\sqrt{2}/3$	0	1/2
7	1/3	0	2/3	0	4/3	1/2
8	1/3	2/3	0	$\sqrt{2}/3$	0	1/2
9	1/3	0	2/3	0	4/3	1/2
10	1/3	2/3	0	$-\sqrt{2}/3$	0	1/2
11	1/3	2/3	0	$\sqrt{2}/3$	0	1/2
12	1/3	0	2/3	0	4/3	1/2

Table 3.6 S_{ij} and polarization values for <111> stress

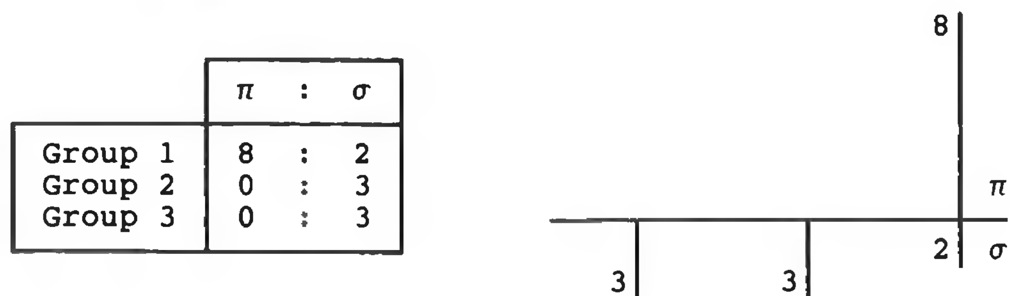

	π : σ
Group 1	8 : 2
Group 2	0 : 3
Group 3	0 : 3

Table 3.7 and Fig 2.4 Splittings and polarizations for stress along <111>

P||<110>

Since there are two non-equivalent crystal directions perpendicular to <110> (i.e. <001> and <1$\bar{1}$0>), there will be two sets of inequivalent σ-polarization results. We know

they are inequivalent because each direction has a different value for the projection onto <110>

Under <110> stress the transition splits into 4 groups :

Group 1 : $\delta_6 = a_3$ (3.13)

Group 2 : $\delta_7 = a_2$ (3.14)

Group 3 : $\delta_8 = 1/4(2a_1 + a_2 + a_3 - \sqrt{2}a_4)$ (3.15)

Group 4 : $\delta_9 = 1/4(2a_1 + a_2 + a_3 + \sqrt{2}a_4)$ (3.16)

Centre No.	S_{xx}	S_{yy}	S_{zz}	S_{xy}	π ||<110	σ_1 ||<1$\bar{1}$0>	σ_2 ||<001>
1	0	0	1	0	2	0	0
2	0	1	0	0	0	2	0
3	0	0	1	0	2	0	0
4	0	1	0	0	0	2	0
5	1/2	1/4	1/4	$-\sqrt{2}/4$	1/2	1/2	1
6	1/2	1/4	1/4	$-\sqrt{2}/4$	1/2	1/2	1
7	1/2	1/4	1/4	$\sqrt{2}/4$	1/2	1/2	1
8	1/2	1/4	1/4	$\sqrt{2}/4$	1/2	1/2	1
9	1/2	1/4	1/4	$-\sqrt{2}/4$	1/2	1/2	1
10	1/2	1/4	1/4	$-\sqrt{2}/4$	1/2	1/2	1
11	1/2	1/4	1/4	$\sqrt{2}/4$	1/2	1/2	1
12	1/2	1/4	1/4	$\sqrt{2}/4$	1/2	1/2	1

Table 3.8 S_{ij} and polarization values for <110> stress

	π : σ_1 : σ_2
Group 1	4 : 0 : 0
Group 2	4 : 0 : 0
Group 3	2 : 2 : 4
Group 4	2 : 2 : 4

Table 3.9 Polarization intensities for stress along <110>

Each δ_i represents a shift rate so if we go to the actual APPLIED STRESS vs. ENERGY SHIFT stress data, it is easy to ascribe each component in the graph to one or other of the shift rates, by virtue of the polarization data. If we work out the numerical value of the individual shift rates of each

component (the slope of that line on the graph), we end up

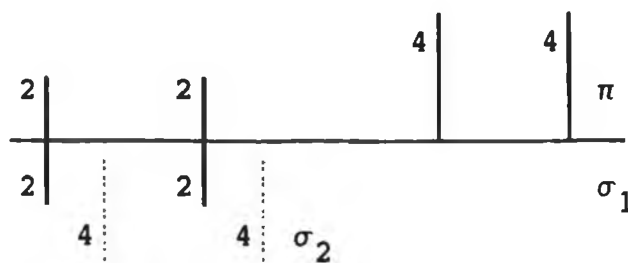

Fig. 3.5 Splittings and polarization intensities for stress along <110> direction

with a set of simultaneous equations . In this case we get 9 simultaneous equations in 4 variables (a_1, a_2, a_3 and a_4), which is easily solvable.

3.4 CRYSTAL CO-ORDINATES

If we compare our results for the splitting under stress of a monoclinic I defect with those obtained by Kaplayanskii ((a) 1963) we find that although he too needs only 4 parameters to predict the splitting, he has different co-efficients.

The conversion table between our co-efficients and Kaplayanskii's is given in Table 3.10.

OUR NOTATION	KAPLAYANSKII'S NOTATION
a_1	A_1
a_2	$A_2 - A_1$
a_3	$A_2 + A_3$
a_4	$2\sqrt{2}A_4$

Table 3.10 comparison of our results with Kaplayanskii's

The reason that the co-efficients differ is because Kaplayanskii takes a different approach to the problem.

Whereas we keep the stress direction constant and examine the way the different inequivalent centres behave, he keeps the defect constant and examines the way that originally equivalent crystal directions behave under stress. This approach is described as using *crystal co-ordinates*.

To illustrate this type of approach we will now examine a non-degenerate $A \rightarrow A$ transition at a C_{3v} trigonal centre. Such a centre has a three-fold axis lying along the <111> direction, this axis is usually taken to be the Z-axis of the defect. One such trigonal centre would have the following defect axes :

$$\text{Z-axis} = \langle 111 \rangle \ : \ \text{Y-axis} = \langle \bar{1}10 \rangle \ : \ \text{X-axis} = \langle 11\bar{2} \rangle$$

We call this set of axes our *standard orientation*. In the unstressed crystal there are four equivalent Z-directions corresponding to the four <111> type body diagonals of a unit cube.

For P||<100> all four <111> directions remain equivalent since they all have equal projections from <111> onto <100>, so we don't expect the transition to split under <100> stress. At most there might be some kind of hydrostatic shift.

The four <111> axes split into two groups of two for P||<110>. We will call these the <110> and $\langle 1\bar{1}0 \rangle$ groups. Hence we expect the transition to split into 2 components under <110> stress..

For P||<111> the four axes split into a group of one (the axis lying parallel to the Z-axis) and a group of three. So again we expect the line to split into two components, which we denote by the <111> and $\langle 1\bar{1}1 \rangle$ groups.

The potential created by a trigonal defect in a T_d symmetry environment is given by Hughes and Runciman (1967) as ;

$$V = a_1(S_{xx} + S_{yy} + S_{zz}) + a_2(S_{yz} + S_{zx} + S_{xy})$$

$$+ E_x(S_{xx} + S_{yy} - 2S_{zz}) + E_x'(S_{xx} + S_{yy} - 2S_{zz})$$

$$+ E_y\sqrt{3}(S_{xx} - S_{yy}) + E_y'\sqrt{3}(S_{yz} - S_{zx}) \qquad (3.17)$$

If we restrict ourselves to transitions involving non-degenerate states that means we need only concern ourselves with functions that transform as one-dimensional representations of the C_{3v} symmetry groups i.e. only those parts of Eq. 3.17 with a_1 and a_2 co-efficients remain. Which means Eq. 3.17 reduces down to ;

$$V = a_1(S_{xx} + S_{yy} + S_{zz}) + a_2(S_{yz} + S_{zx} + S_{xy}) \qquad (3.18)$$

We now calculate the S_{ij} values for stress along the different directions.

For P||<100> we find $S_{xx} = 1$ and all other $S_{ij} = 0$ therefore our first shift rate δ_1 is just ;

$$\delta_1 = a_1 \qquad (3.19)$$

i.e. the spectral line does not split, which is what we predicted.

For P||<110> we find :

$$\left.\begin{array}{l} S_{xx} = S_{yy} = S_{xy} = 1/2 \\ S_{ij} = 0 \text{ for all others} \end{array}\right\} \Rightarrow \delta_2 = a_1 + 1/2\ a_2 \qquad (3.20)$$

For P||<1$\bar{1}$0> we find :

$$\left.\begin{array}{l} S_{xx} = S_{yy} = 1/2 \\ S_{xy} = -1/2 \\ S_{ij} = 0 \text{ for all others} \end{array}\right\} \Rightarrow \delta_3 = a_1 - 1/2\ a_2 \qquad (3.21)$$

i.e. under <110> stress, the spectral line splits into two components whose shift rates are given in Eq.'s 3.20 and 2.21.

For P||<111> we find :

$$S_{ij} = 1/3 \text{ for all } i,j$$

$$\Rightarrow \delta_4 = a_1 + a_2 \qquad (3.22)$$

For $P||\langle 1\bar{1}1\rangle$ we find :

$$\left.\begin{array}{l} S_{xx} = S_{yy} = S_{zz} = S_{zx} = 1/3 \\ S_{xy} = S_{yz} = -1/3 \end{array}\right\} \Rightarrow \delta_5 = a_1 - 1/3\, a_2 \qquad (3.23)$$

i.e. the line splits into 2 components under <111> stress.

Note we only need two parameters to fully describe the A →A transition at a trigonal defect using Kaplayanskii's crystal co-ordinates.

3.5 TRANSITIONS INVOLVING DEGENERATE STATES

To fully understand transitions involving degenerate states some time-independent Perturbation Theory for stationary states is needed. Applying stress to such a transition can effect it in any of the 3 following ways :

(1) The stress will remove some, or, all of the electronic degeneracy.
(2) The stress will remove any orientational degeneracy.
(3) The stress will do both of the above, depending on the situation

In the most general terms, if the roots of the secular equation of the Hamiltonian of the system are all different, then all the degeneracy will be removed. To illustrate this we will return to the case of a trigonal defect but in this case we examine an A → E transition.

E states are 2-dimensional representations and as such we can split them into 2 components E_x and E_y. We recall that the Hamiltonian representing the potential about a C_{3v} trigonal defect in a T_d environment is given in Eq. 3.17

$$V = a_1(S_{xx} + S_{yy} + S_{zz}) + a_2(S_{yz} + S_{zx} + S_{xy})$$

$$+ E_x(S_{xx} + S_{yy} -2S_{zz}) + E_x'(S_{xx} + S_{yy} -2S_{zz})$$

$$+ E_y\sqrt{3}(S_{xx} - S_{yy}) + E_y'\sqrt{3}(S_{yz} - S_{zx}) \quad (3.17)$$

This is substituted into the secular matrix which is given below in Table 3.11.

H_s	E_x	E_y
E_x	$\langle E_x \vert V \vert E_x \rangle$	$\langle E_x \vert V \vert E_y \rangle$
E_y	$\langle E_y \vert V \vert E_x \rangle$	$\langle E_y \vert V \vert E_y \rangle$

Table 3.11 Secular matrix for the stress Hamiltonian

As stated already, the degeneracy of the system will only be lifted if the solutions to the secular equation are distinct i.e.

for $$\det\left| \hat{H}' - \lambda \, Id \right| = 0 \quad (3.24)$$

where

$$\hat{H}' = H_0 + H_s \quad (3.25)$$

Id = the identity matrix

and λ = the eigen values

We require all the eigenvalues to be unique.

Clearly it would be very laborious to substitute Eq. 3.17 for V in Table 3.11 and work every component out for each element. Fortunately we can use the Wigner-Eckart theorem to deduce which elements are equal to zero.

The Wigner-Eckart theorem states :

$$\langle E_q | O_{\Pi_\Gamma} | E_s \rangle = [E || O || E] . \langle \Pi_\Gamma E_s | E_q \rangle \quad (3.26)$$

Clebsch-Gordon co-efficient

where O_{Π_Γ} = the operator that transforms according to the Γ representation of the group Π.

The Clebsch-Gordon co-efficients can be found in most standard group theory books (Griffiths 1961). Basically ,if the the Clebsch-Gordon co-efficient is equal to zero then we can ignore that term in the secular equation.

For example $< E_x | H_s | E_x >$splits into :

$$< E_x | A_1 | E_x > = [E || A_1 || E].\text{constant} = \mathbb{A}_1 \qquad (3.27)$$

$$< E_x | A_1' | E_x > = [E || A_1' || E].\text{constant} = 2\mathbb{A}_2 \qquad (3.28)$$

$$< E_x | E_x | E_x > = [E || E_x || E].(-1/\sqrt{2}) = -\mathbb{B} \qquad (3.29)$$

$$< E_x | E_x' | E_x > = [E || E_x' || E].(-1/\sqrt{2}) = -\mathbb{C} \qquad (3.30)$$

$$< E_x | E_y | E_x > = [E || E_y || E].0 = 0 \qquad (3.31)$$

$$< E_x | E_y' | E_x > = [E || E_y' || E].0 = 0 \qquad (3.32)$$

$\mathbb{A}_1$, $\mathbb{A}_2$,$\mathbb{B}$, and $\mathbb{C}$ are all just constants . We should expect Eq.'s 3.31 and 3.32 to be equal to zero since E_x and E_y are orthogonal to each other. Thus we now find by substituting the above equations back into $< E_x | H_s | E_x >$,

$$\begin{aligned} < E_x | H_s | E_x > = \; & < E_x | A_1(S_{xx} + S_{yy} + S_{zz}) | E_x > \\ & + < E_x | A_1'(S_{yz} + S_{zx} + S_{xy}) | E_x > \\ & + < E_x | E_x(S_{xx} + S_{yy} - 2S_{zz}) | E_x > \\ & + < E_x | E_x'(S_{yz} + S_{zx} - 2S_{xy}) | E_x > \end{aligned} \qquad (3.33)$$

$$\begin{aligned} \Rightarrow < E_x | H_s | E_x > = \; & (S_{xx} + S_{yy} + S_{zz}) < E_x | A_1 | E_x > \\ & + (S_{yz} + S_{zx} + S_{xy}) < E_x | A_1' | E_x > \\ & + (S_{xx} + S_{yy} - 2S_{zz}) < E_x | E_x | E_x > \\ & + (S_{yz} + S_{zx} - 2S_{xy}) < E_x | E_x' | E_x > \end{aligned} \qquad (3.34)$$

$$\Rightarrow \langle E_x | H_s | E_x \rangle = \mathbb{A}_1(S_{xx} + S_{yy} + S_{zz}) + 2\mathbb{A}_2(S_{yz} + S_{zx} + S_{xy})$$
$$-\mathbb{B}(S_{xx} + S_{yy} - 2S_{zz}) - \mathbb{C}(S_{yz} + S_{zx} - 2S_{xy}) \quad (3.35)$$

If we define $\alpha = \mathbb{A}_1(S_{xx} + S_{yy} + S_{zz})+2\mathbb{A}_2(S_{yz} + S_{zx} + S_{xy})$

and $\beta = \mathbb{B}(S_{xx} + S_{yy} - 2S_{zz})+ \mathbb{C}(S_{yz} + S_{zx} - 2S_{xy})$

we can rewrite Eq. 3.35 as :

$$\langle E_x | H_s | E_x \rangle = \alpha - \beta \quad (3.36)$$

similarly we find

$$\langle E_y | H_s | E_y \rangle = \alpha + \beta \quad (3.37)$$

and

$$\langle E_x|H_s| E_y\rangle = \langle E_y|H_s|E_x\rangle = \mathbb{B}\sqrt{3}(S_{xx} - S_{yy})+ \mathbb{C}\sqrt{3}(S_{yz} - S_{zx}) \quad (3.38)$$

we define $\gamma = \mathbb{B}\sqrt{3}(S_{xx} - S_{yy}) + \mathbb{C}\sqrt{3}(S_{yz} - S_{zx})$

$$\Rightarrow \langle E_x|H_s| E_y\rangle = \langle E_y|H_s|E_x\rangle = \gamma \quad (3.39)$$

So we can rewrite our secular matrix as Table 3.12 :

H_s	E_x	E_y
E_x	$\alpha-\beta$	γ
E_y	γ	$\alpha+\beta$

Table 3.12 Revised secular matrix for an A - E transition at a trigonal defect

We want :

$$\begin{vmatrix} \alpha - \beta - \lambda & \gamma \\ \gamma & \alpha + \beta - \lambda \end{vmatrix} = 0$$

which only happens when :

$$\lambda = \alpha \pm (\gamma^2 + \beta^2)^{1/2} \tag{3.40}$$

We need now only calculate the values of λ under the different stresses. Recall :

$$\alpha = \mathbb{A}_1(S_{xx} + S_{yy} + S_{zz}) + 2\mathbb{A}_2(S_{yz} + S_{zx} + S_{xy})$$

$$\beta = \mathbb{B}(S_{xx} + S_{yy} - 2S_{zz}) + \mathbb{C}(S_{yz} + S_{zx} - 2S_{xy})$$

$$\gamma = \mathbb{B}\sqrt{3}(S_{xx} - S_{yy}) + \mathbb{C}\sqrt{3}(S_{yz} - S_{zx})$$

(1) P||<100>

$\Rightarrow$ $S_{xx} = 1$ and all other $S_{ij} = 0$

$$\left.\begin{cases} \alpha = \mathbb{A}_1 \\ \beta = \mathbb{B} \\ \gamma = \sqrt{3}\ \mathbb{B} \end{cases}\right\} \Rightarrow \lambda = \mathbb{A}_1 \pm 2\mathbb{B}$$

So, the E state splits into 2 components :

$$\delta_1 = \mathbb{A}_1 + 2\mathbb{B} \tag{3.41}$$

$$\delta_2 = \mathbb{A}_1 - 2\mathbb{B} \tag{3.42}$$

(2) P||<111>

$\Rightarrow$ $S_{ij} = 1/3$ for all i,j

$\Rightarrow$ $\alpha = \mathbb{A}_1 + 2\mathbb{A}_2$

and $\beta = \gamma = 0$

$\Rightarrow$ $\lambda = \delta_3 = \mathbb{A}_1 + 2\mathbb{A}_2$

This is a case where the degeneracy has not been lifted by the stress, we can say this because there is no ± term in Eq.

3.43, i.e. this two dimensional secular matrix only yields one eigenvalue.

$P||\langle 1\bar{1}1\rangle$

$\Rightarrow \quad S_{xx} = S_{yy} = S_{zz} = S_{xz} = 1/3$

and $\quad S_{xy} = S_{yz} = -1/3$

$$\Rightarrow \left\{\begin{array}{l} \alpha = \mathbb{A}_1 - 2/3\ \mathbb{A}_2 \\ \beta = 2/3\ \mathbb{B} \\ \gamma = -2/\sqrt{3}\ \mathbb{C} \end{array}\right\} \Rightarrow \lambda = \mathbb{A}_1 - 2/3\ \mathbb{A}_2 \pm 4/3\ \mathbb{C}$$

$$\Rightarrow \quad \delta_4 = \mathbb{A}_1 - 2/3\ \mathbb{A}_2 + 4/3\ \mathbb{C} \qquad (3.44)$$

$$\text{and} \quad \delta_5 = \mathbb{A}_1 - 2/3\ \mathbb{A}_2 - 4/3\ \mathbb{C} \qquad (3.45)$$

(3) $P||\langle 110\rangle$

$\Rightarrow \quad S_{xx} = S_{yy} = S_{xy} = 1/2$

all other $S_{ij} = 0$

$\Rightarrow \quad \alpha = \mathbb{A}_1 + \mathbb{A}_2 \ : \ \beta = \mathbb{B} - 2\mathbb{C} \ : \ \gamma = 0$

$\Rightarrow \quad \lambda = \mathbb{A}_1 + \mathbb{A}_2 \pm (\ \mathbb{B} - 2\mathbb{C}\ )$

$$\Rightarrow \quad \delta_6 = \mathbb{A}_1 + \mathbb{A}_2 + (\ \mathbb{B} - 2\mathbb{C}\ ) \qquad (3.46)$$

$$\text{and} \quad \delta_7 = \mathbb{A}_1 + \mathbb{A}_2 - (\ \mathbb{B} - 2\mathbb{C}\ ) \qquad (3.47)$$

$P||\langle 1\bar{1}0\rangle$

$\Rightarrow \quad S_{xx} = S_{yy} = 1/2,\ S_{xy} = -1/2$

all other $S_{ij} = 0$

$\Rightarrow \quad \alpha = \mathbb{A}_1 + \mathbb{A}_2 \ : \ \beta = \mathbb{B} + 2\mathbb{C} \ : \ \gamma = 0$

$$\Rightarrow \qquad \lambda = \mathbb{A}_1 - \mathbb{A}_2 \pm (\mathbb{B} + 2\mathbb{C})$$

$$\Rightarrow \qquad \delta_8 = \mathbb{A}_1 - \mathbb{A}_2 + (\mathbb{B} + 2\mathbb{C}) \qquad (3.48)$$

$$\Rightarrow \qquad \delta_9 = \mathbb{A}_1 - \mathbb{A}_2 - (\mathbb{B} + 2\mathbb{C}) \qquad (3.49)$$

Again we end up with 9 equations in 4 variables which should prove little problem.

Now that we know the way the lines split under stress it remains only to work out the polarization intensities. This requires the identity of 24 possible inequivalent trigonal defect co-ordinates. These are given in Table 3.13.

Of these 24 , only those which are non-equivalent, relative to the stress and polarization axes are needed to calculate the intensities . For <100> stress only one centre with co-ordinates (X,Y,Z) = ($11\bar{2}$, $\bar{1}10$, 111) need be considered with the electric vector *D* on <100>. <110> uses this orientation also ,along with another at (X,Y,Z) = ($1\bar{1}\bar{2}$, 110, $11\bar{1}$) with *D* on <110> and <110> respectively. For <111> we can use both the above orientations plus a third one at (X,Y,Z) = ($1\bar{2}\bar{1}$, $\bar{1}0\bar{1}$, $11\bar{1}$) with *D* on <111>. These 3 orientations are regarded as being populated in the ratios 1:2:1.

CENTRE	Z	Y	X	CENTRE	Z	Y	X
1	$1\bar{1}\bar{1}$	110	$\bar{1}\bar{1}2$	13	$\bar{1}1\bar{1}$	$0\bar{1}\bar{1}$	$\bar{2}1\bar{1}$
2	$\bar{1}1\bar{1}$	$\bar{1}\bar{1}0$	$\bar{1}12$	14	$1\bar{1}1$	$0\bar{1}1$	$\bar{2}11$
3	$\bar{1}\bar{1}1$	110	$\bar{1}\bar{1}\bar{2}$	15	$\bar{1}\bar{1}1$	011	$2\bar{1}1$
4	$\bar{1}1\bar{1}$	$10\bar{1}$	$\bar{1}\bar{2}\bar{1}$	16	111	$10\bar{1}$	121
5	111	$\bar{1}01$	$1\bar{2}1$	17	$\bar{1}1\bar{1}$	$\bar{1}01$	$\bar{1}\bar{2}\bar{1}$
6	$\bar{1}\bar{1}1$	101	$\bar{1}21$	18	$\bar{1}\bar{1}1$	$\bar{1}0\bar{1}$	$\bar{1}21$
7	$1\bar{1}\bar{1}$	$\bar{1}0\bar{1}$	$12\bar{1}$	19	$1\bar{1}\bar{1}$	101	$1\bar{2}\bar{1}$
8	111	$01\bar{1}$	$\bar{2}11$	20	$1\bar{1}\bar{1}$	$\bar{1}\bar{1}0$	$1\bar{1}2$
9	$\bar{1}\bar{1}1$	$0\bar{1}\bar{1}$	$2\bar{1}1$	21	111	$\bar{1}10$	$11\bar{2}$
10	$1\bar{1}\bar{1}$	$0\bar{1}1$	$\bar{2}\bar{1}\bar{1}$	22	$\bar{1}\bar{1}1$	$1\bar{1}0$	$\bar{1}\bar{1}\bar{2}$
11	$\bar{1}1\bar{1}$	011	$21\bar{1}$	23	$\bar{1}1\bar{1}$	110	$\bar{1}12$
12	$1\bar{1}\bar{1}$	$01\bar{1}$	$\bar{2}\bar{1}\bar{1}$	24	111	$1\bar{1}0$	$11\bar{2}$

Table 3.13 Defect co-ordinates of the 24 inequivalent C_{3v} trigonal defects under T_d symmetry

Calculation of the polarization intensities are often much simplified by finding what form the corresponding eigenvectors take.
To find the eigenvectors we must substitute the two values of λ given in Eq. 3.40 into Eq. 3.50

$$\begin{pmatrix} \alpha - \beta - \lambda & \gamma \\ \gamma & \alpha + \beta - \lambda \end{pmatrix} \cdot \begin{pmatrix} X \\ Y \end{pmatrix} = 0 \qquad (3.50)$$

If we take the lower energy value of λ first (i.e $\lambda = \alpha -$ ...) and substitute in we find that X = 0 which means that the lower energy component of a line split under stress, and that has had all its' degeneracy removed, is a pure E_y state. Similarly, by taking the higher energy component of λ we find the higher energy line in such a case is a pure E_x state. Therefore if the intensity of a transition is proportional to the relationship given in Eq. 3.51

$$I \propto |\langle \Phi \mid D \mid A \rangle|^2 \qquad (3.51)$$

where : D = the electric dipole vector operator
A = the A state

then for all stress directions except <111> the Φ state can be replaced by either an E_x or E_y state. For the <111> case, where all the degeneracy is not removed, then Φ is just a linear combination of these two states i.e.

$$\Phi = c_1 E_x + c_2 E_y \qquad (3.52)$$

$$\Rightarrow \qquad I \propto |\langle c_1 E_x + c_2 E_y \mid D \mid A \rangle|^2$$

$$\Rightarrow \qquad I \propto |\langle c_1 E_x \mid D \mid A \rangle + \langle c_2 E_y \mid D \mid A \rangle|^2$$

$$\Rightarrow \qquad I \propto |c_1 \langle E_x \mid D \mid A \rangle + c_2 \langle E_y \mid D \mid A \rangle|^2$$

But we can separate D into components such that :

$$D = X + Y + Z$$

and since we have assumed D is parallel to the crystal Z axis then the Z component of D will contribute nothing to the overall intensity which means we can say :

$$I \; \alpha \; | \; c_1 < E_x | \; X \; | \; A > + \; c_2 < E_y \; | \; Y \; | \; A > |^2$$

for this direction we use the following co-ordinates as our standard orientation.

Z	Y	X
111	$\bar{1}10$	$11\bar{2}$

Take π ||<111> and σ ||<110> :

$$\left.\begin{array}{l} \pi_x = -2/\sqrt{18} + 1/\sqrt{18} + 1/\sqrt{18} = 0 \\ \pi_y = 0 \end{array}\right\} \Rightarrow I_\pi = |0 + 0|^2 = 0$$

$$\left.\begin{array}{l} \sigma_x = 0 \\ \sigma_y = -1 \end{array}\right\} \Rightarrow I_\sigma = |0 - 1|^2 = 1$$

$$\begin{array}{c} \pi : \sigma \\ 0 : 1 \end{array}$$

For all other stress directions :

$$I \; \alpha \; |< \Phi \; | \; D \; | \; A >|^2$$

where $\Phi = E_x$ or E_y

e.g. for P||<110> we use the following co-ordinates :

Z	Y	X
111	$\bar{1}10$	$11\bar{2}$

$\pi || <110> : \sigma_1 || <001> : \sigma_1 || <\bar{1}10>$

$$\pi_x = 4/12 : \pi_y = 0$$

$$\sigma_{1x} = 8/12 : \sigma_{1y} = 0$$

$$\sigma_{2x} = 0 \quad : \sigma_{2y} = 1$$

For $P || <1\bar{1}0>$ we use the following co-ordinates :

Z	Y	X
111	$1\bar{1}0$	112

$\pi || <110> : \sigma_1 || <001> : \sigma_1 || <1\bar{1}0>$

$$\pi_x = 0 \quad : \pi_y = 1$$

$$\sigma_{1x} = 8/12 : \sigma_{1y} = 0$$

$$\sigma_{2x} = 4/12 : \sigma_{2y} = 0$$

Thus we expect the polarization intensities to be as given in Fig. 3.6

Fig 3.6 Splittings and polarization intensities for an A - E transition under <110> stress

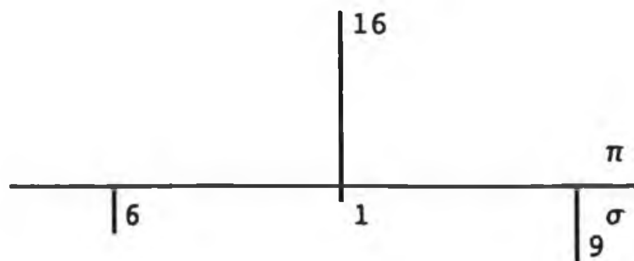

Fig. 3.7 Splittings and polarization intensities for stress along <111> direction

A similar method is used for the P||<111> case to give the intensities shown in Fig. 3.7.

N.B. The polarization intensities calculated so far are valid only for stress measurements in absorption, cathodoluminescence, or luminescence excited by above band-gap radiation. In the case of luminescence excited by below band-gap radiation, a further factor must be taken into consideration. Here, we assume the transition occurs because a dipole moment at the ith orientation of the optical centre is aligned with direction cosines :

$$(l_z^i , m_z^i , n_z^i) \quad \text{w.r.t. the crystal axes}$$

The excitation is polarized such that *D* has direction cosines

$$(l_e , m_e , n_e) \quad \text{w.r.t. the crystal axes}$$

The centre emits luminescence with its' *D* vector along :

$$(l_d , m_d , n_d) \quad \text{w.r.t. the crystal axes}$$

: and with intensity I :

$$I \propto [(l_z l_e + m_z m_e + n_z n_e)^2 . (l_z l_d + m_z m_d + n_z n_d)^2]$$

3.6 MIXING OF STATES

Mixing of states occurs between two states of nearly equal energy sometimes called *nearly degenerate* states, and is essentially an interaction between the levels resulting in a non-linear shiftrate. This effect manifests itself in the Stress vs Energy shift graphs as non-linear, curved shift rates instead of the expected straight ones.

Let us again take the example of an A to E transition at a trigonal centre and we will assume that the level mixing with the transition is another E level. The interaction matrix in this case becomes :

H_s	E_x	E_y	E_x'	E_y'
E_x	$\langle E_x \| H_s \| E_x \rangle$	$\langle E_x \| H_s \| E_y \rangle$	$\langle E_x \| H_s \| E_x' \rangle$	$\langle E_x \| H_s \| E_y' \rangle$
E_y	$\langle E_y \| H_s \| E_x \rangle$	$\langle E_y \| H_s \| E_y \rangle$	$\langle E_y \| H_s \| E_x' \rangle$	$\langle E_y \| H_s \| E_y' \rangle$
E_x'	$\langle E_x' \| H_s \| E_x \rangle$	$\langle E_x' \| H_s \| E_y \rangle$	$\langle E_x' \| H_s \| E_x' \rangle$	$\langle E_x' \| H_s \| E_y' \rangle$
E_y'	$\langle E_y' \| H_s \| E_x \rangle$	$\langle E_y' \| H_s \| E_y \rangle$	$\langle E_y' \| H_s \| E_x' \rangle$	$\langle E_y' \| H_s \| E_y' \rangle$

From our earlier calculations we already know some of the elements in this matrix :

H_s	E_x	E_y	E_x'	E_y'
E_x	$\alpha - \beta$	γ	?	?
E_y	γ	$\alpha + \beta$	?	?
E_x'	?	?	$\alpha' - \beta'$	γ'
E_y'	?	?	γ'	$\alpha' + \beta'$

The job of filling in the question marks is made much easier by the fact that we know the $\langle E_i | H_s | E_i \rangle$ (where i = x or y) behave in the same manner as they did in the previous section, and that

$$\langle E | \; | E' \rangle = \langle E' | \; | E \rangle$$

So we can predict that the final matrix will have the form shown below where θ, π and ζ are some new constants with similar mathematical origins as α, β and γ in section 3.5 .

The eigenvalues are calculated in the usual manner and from these it is easy to calculate the S_{ij} values and determine which components survive.

H_s	E_x	E_y	E_x'	E_y'
E_x	$\alpha - \beta$	γ	$\theta - \pi$	ζ
E_y	γ	$\alpha + \beta$	ζ	$\theta - \pi$
E_x'	$\theta - \pi$	ζ	$\alpha' - \beta'$	γ'
E_y'	ζ	$\theta + \pi$	γ'	$\alpha' + \beta'$

3.7 SPIN-ORBIT COUPLING

A, E and T states all arise from angular momentum considerations so , if we assume spin states take part in the interactions we get two more components in our basis functions ; a and b

where $a = |1/2,1/2\rangle$ and $b = |1/2,-1/2\rangle$

The first part indicates the magnitude of the spin vector projected onto the z-axis and the second part describes its' direction. The perturbation Hamiltonian given in Eq. 3.2 now becomes :

$$H = \sum a_{ij}S_{ij} + \xi \underline{L}.\underline{S} \qquad (3.52)$$

While the basis functions of the secular matrix change to :

$$|E_x\rangle|a\rangle \qquad |E_x\rangle|b\rangle$$

$$|E_y\rangle|a\rangle \qquad |E_y\rangle|b\rangle$$

Working out the values of the individual $\langle E_i|\langle\phi|H_s|\phi\rangle|E_i\rangle$ (for i = x or y and ϕ = a or b)is simplified by the fact that cross terms in the spin states equal zero i.e.

$$\langle a| \quad |b\rangle = \langle b| \quad |a\rangle = 0$$

This is because if we consider the spin part of the $\underline{L}.\underline{S}$ operator we can see that this acts only on the a and b parts

of the basis functions and not on the E_x or E_y parts.

$$\Rightarrow \langle E_x|\langle b|H\ |a\rangle|E_x\rangle = \langle E_x|a_{ij}S_{ij}|E_x\rangle\langle b|\xi\underline{L}.\underline{S}|a\rangle$$

$$= \text{constant}.\langle E_x|a_{ij}S_{ij}|E_x\rangle\langle b|a\rangle$$

but $a \perp b \Rightarrow \quad \langle b|a\rangle = 0$

$$\Rightarrow \quad \langle E_x|\langle b|H\ |a\rangle|E_x\rangle = 0$$

This effectively splits the secular matrix into two half sized dimension matrices of the form :

H_s	$E_x a$	$E_y a$
$E_x a$		
$E_y a$		

H_s	$E_x b$	$E_y b$
$E_x b$		
$E_x b$		

One method employed to find the eigenvalues of these type of matrices uses the fact that both a and b are basis functions in spherical co-ordinates. Intelligible results can only be found when all of :

$$\langle E_i|\langle\phi|\xi\underline{L}.\underline{S}|\phi\rangle|E_i\rangle \quad i = x,y \quad \phi = a,b$$

: is expressed in spherical co-ordinates (see Tinkham p-124) To do this we redefine $\underline{L}$ and $\underline{S}$ in terms of new co-ordinates L_z, L^+, L^- and S_z,S^+,S^- where :

$$L_z|\ l,m\ \rangle = m|\ l,m\ \rangle$$

$$S_z|\ S,M_z\ \rangle = M_z|\ S,M_z\ \rangle$$

$$S^+|1/2,1/2\rangle = |1/2,3/2\rangle$$

$$S^-|1/2,1/2\rangle = |1/2,-1/2\rangle$$

Changing co-ordinates also requires us to redefine the $\underline{L}.\underline{S}$ cross product as :

$$\xi\underline{L}.\underline{S} = \xi(\tfrac{1}{2}L^{+}.S^{-} + L_{z}.S_{z} + \tfrac{1}{2}L^{-}.S^{+})$$

$$\Rightarrow \langle E_x|\langle\alpha|\xi\underline{L}.\underline{S}|\alpha\rangle|E_x\rangle = \langle E_x|\langle\alpha|\xi(\tfrac{1}{2}L^{+}.S^{-} + L_{z}.S_{z} + \tfrac{1}{2}L^{-}.S^{+})|\alpha\rangle|E_x\rangle$$

$$= \langle\alpha|S_Z|\alpha\rangle\langle E_x|\xi L_Z|E_x\rangle$$

$$+ \langle\alpha|S^{-}|\alpha\rangle\langle E_x|\xi L^{+}|E_x\rangle/2$$

$$+ \langle\alpha|S^{+}|\alpha\rangle\langle E_x|\xi L^{-}|E_x\rangle/2$$

By definition :

$$\langle\alpha|S^{-}|\alpha\rangle = \langle\alpha|S^{+}|\alpha\rangle = 0$$

$$\Rightarrow \quad \langle E_x|\langle\alpha|\xi\underline{L}.\underline{S}|\alpha\rangle|E_x\rangle = \langle\alpha|S_z|\alpha\rangle\langle E_x|\xi L_z|E_x\rangle$$

again by definition :

$$S_z|\alpha\rangle = 1/2|\alpha\rangle \Rightarrow \langle\alpha|S_z|\alpha\rangle = 1/2$$

$$\Rightarrow \langle E_x|\langle\alpha|\xi\underline{L}.\underline{S}|\alpha\rangle|E_x\rangle = \langle E_x|\xi L_z|E_x\rangle/2$$

Clearly since everything else is in spherical co-ordinates E_x has little meaning here so it too must be converted. This can be done from first principles using the method given in Tinkham or alternatively they can be found in data tables (Table 1.4 R.K Watts 1977) where they are found to be expressed as single or linear combinations of spherical harmonic operators Y_l^m We find :

$$E_x = 1/\surd 2\ (-Y_1^1 + Y_1^{-1}) + i/\surd 2\ (Y_1^1 + Y_1^{-1}) \qquad (3.52)$$

and

$$E_y = 1/\surd 2\ (-Y_1^1 + Y_1^{-1}) - i/\surd 2\ (Y_1^1 + Y_1^{-1}) \qquad (3.53)$$

Calculating $\langle E_x|\xi L_z|E_x\rangle$ is not as difficult as it might at first appear, once we realise that :

$$L_z|1/\surd 2(-Y_1^1 + Y_1^{-1})\rangle = 1/\surd 2\ L_z|-Y_1^1\rangle + 1/\surd 2\ L_z|Y_1^{-1}\rangle$$

but recall :

$$L_z|1,m> = m|1,m>$$

$$\Rightarrow \qquad L_z|\Upsilon_1^m> = m|\Upsilon_1^m>$$

$$\Rightarrow \qquad = -1/\sqrt{2}\ |-\Upsilon_1^1> - 1/\sqrt{2}\ |\Upsilon_1^{-1}>$$

$$\Rightarrow \quad L_z|E_x> = -1/\sqrt{2}\ (-\Upsilon_1^1 + \Upsilon_1^{-1}) - i/\sqrt{2}\ (\Upsilon_1^1 + \Upsilon_1^{-1}) = i|E_y> \qquad (3.54)$$

So only off-diagonal elements in the secular matrix are affected by the presence of the L.S coupling.

If we let :

$$<E_x|<a|\xi \underline{L}.\underline{S}|a>|E_y> = 1/2\ i\Omega$$

and

$$<E_x|<b|\xi \underline{L}.\underline{S}|b>|E_y> = -1/2\ i\Omega$$

the secular matrices become :

H_s	$E_x a$	$E_y a$
$E_x a$	$\alpha-\beta$	$\gamma+1/2i\Omega$
$E_y a$	$\gamma-1/2i\Omega$	$\alpha+\beta$

H_s	$E_x b$	$E_y b$
$E_x b$	$\alpha-\beta$	$\gamma-1/2i\Omega$
$E_x b$	$\gamma+1/2i\Omega$	$\alpha+\beta$

Fortunately both matrices yield the same eigenvalue

$$\lambda = \alpha^2 \pm (\beta^2 + \gamma^2 + 1/4\Omega^2)^{1/2} \qquad (3.55)$$

which is in good agreement with Ludlow (1968). The shiftrates can be calculated from this equation in the manner already shown.

3.8 ZEEMAN STUDIES

Since the discovery of isoelectronic bound exciton (IBE) radiative recombination in semiconductors in 1962 (Dietz et al.) much work has been conducted on these types of defects in an attempt to determine the process by which the excitons bind to them and also to identify their geometrical symmetry.

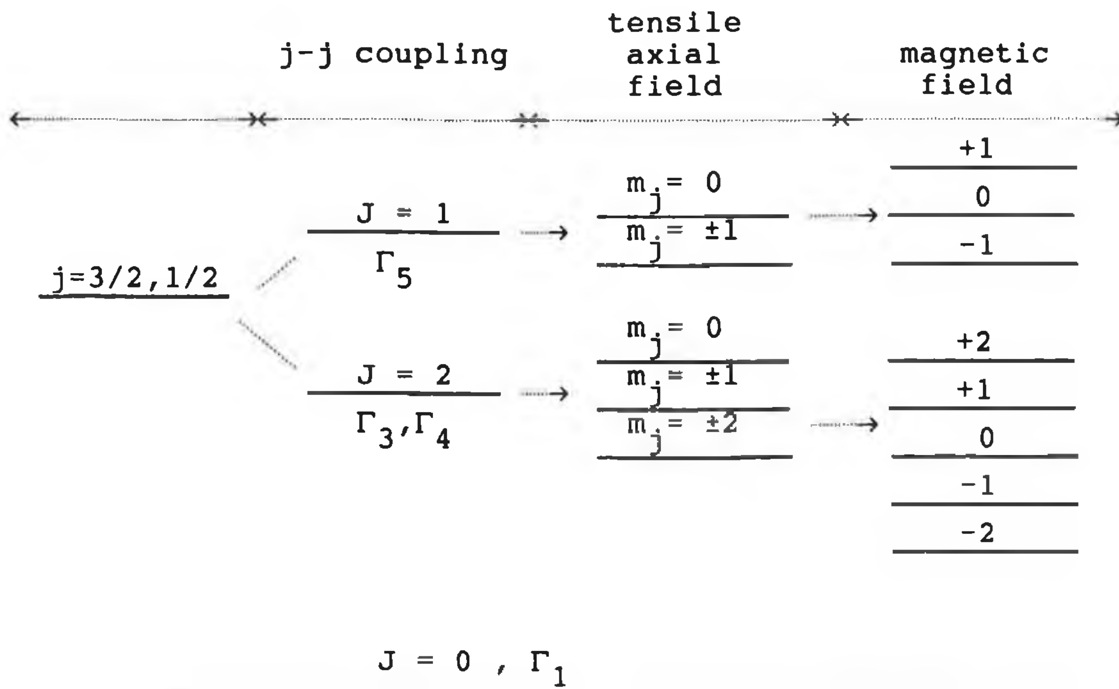

Fig. 3.8 The zero phonon level structure of a quintuplet - triplet BE system

To this end, the effect of magnetic fields on the optical spectra, termed *Zeeman Spectroscopy*, has proved to be a very powerful technique.

To understand its' significance we must first examine the effects of internal strain and j-j coupling on the energy level structure of these defects.

If we have a j = 1/2 electron from the bottom of the C.B. and a j = 3/2 hole from the top of the V.B. then they can couple to form excitonic states of total angular momentum J = 1 or J = 2, with the J = 2 level lying lower in energy. If a tensile axial strain is present about the defect the J values no longer remain good quantum numbers so the J = 2 level splits into m_j = ±2, ±1 and 0 sublevels, in order of increasing energy, while the J = 1 level splits into m_j = ±1 and 0. The 2-fold degeneracy of these m_j levels is called *Kramers degeneracy*. The selection rules for optical spectra namely :

$$\Delta S = 0$$

$$\Delta l = 0, \pm 1$$

$$\Delta j = 0, \pm 1 \text{ (0 to 0 forbidden)}$$

$$\Delta m_j = 0, \pm 1 \text{ (if } \Delta j = 0 \text{ then 0 to 0 forbidden)}$$

: still apply so transitions from the $m_j = \pm 2$, and 0 sublevels to the $m_j = 0$ crystal ground state are dipole forbidden, while the $m_j = \pm 1$ sublevel are dipole allowed.

Examples of such systems are GaP:N (Dean et al. 1963), GaP:Bi (Dean et al. 1969) and Si:Tl (Watkins 1984). If the symmetry is sufficiently low, all the degeneracy may be removed, as in the case of the C_{1h} symmetry defect reported in GaP (Monemar et al. 1986).

All the reported electron attractive neutral IBE defects in semiconductors have been found to exhibit this quintet-triplet (QT) nature although some hole attractive defects arising out of compressive local strain in CdTe (Monemar et al. 1986) and ZnTe (Holtz et al. 1986) also conform to this QT model.

If the axial field is compressive then the lowest energy hole state becomes the $j = 3/2$, $| m_j | = 1/2$ state. If the hole is the tightly bound particle it is much more sensitive to the local crystal field around the defect as in the case of the S_P - Ge_P defect in GaP (White et al. 1974). This centre has been interpreted as having a next-nearest neighbour C_{2v} configuration which restricts the degeneracy of allowed states so that the hole orbital angular momentum becomes quenched. This leaves the hole behaving as a simple isotropic $j = 1/2$ state.

j-j coupling of these states with $j = 1/2$ electrons results in an $S = 1$ triplet and an $S = 0$ singlet state. Here we ignore the orbital angular momentum L and use S only since the exciton states are pure spin states .This situation can also arise with IBE acceptor defects if the local crystal field is sufficiently strong. Several of these types of defects have been detected in electron irradiated Si:Li (

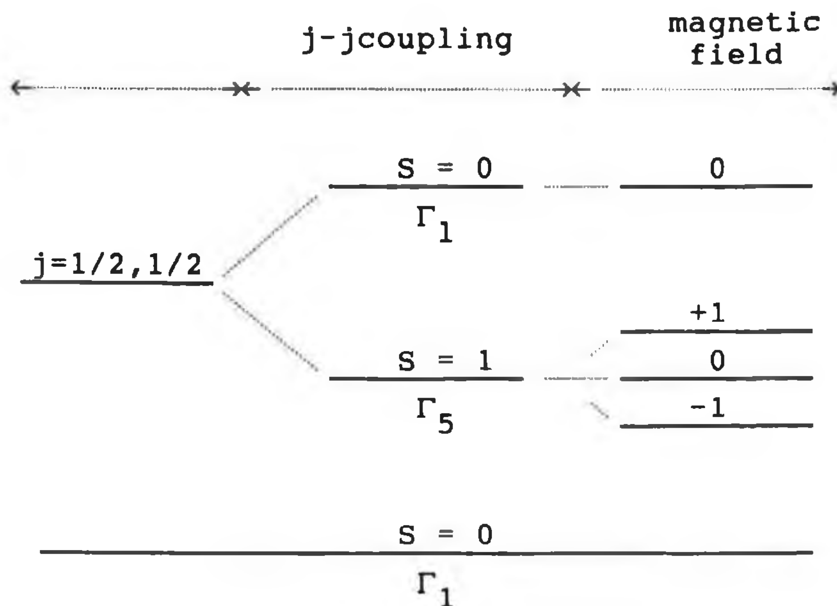

Fig. 3.9 The zero phonon level structure of a triplet - singlet BE system

Lightowlers et al. 1984). Orbital angular momentum quenching seems to be a common effect in complex defects in GaP (Gislason 1985) and Si (Watkins 1985) but has also been observed in direct gap materials such as GaAs (Gislason 1985) and InP (Skolnick 1983).

In both cases, any degeneracy resulting from the local strain field or the j-j coupling can be removed by applying a magnetic field which results in a splitting of the states by an amount given by :

$$\Delta E = \pm \mu_B g_{eff} m_j H_z \qquad (3.56)$$

where μ_B = the Bohr magneton
g_{eff} = the effective g-factor
and H_z = the component of the magnetic field along the defect axis.

Naturally some cases occur that are intermediate between these two extremes i.e. the hole might have a spin-like character but with a strong contribution of angular momentum due to strong effects of spin-orbit coupling such as occurs in CdTe (Monemar 1986). In this case a more complete set of

hole basis functions has to be used in the diagonalization of the perturbation Hamiltonian. Such an analysis has not been carried out for a complex defect in any semiconductor material.

CHAPTER 4 : EXPERIMENTAL APPARATUS AND METHODS

4.1 INTRODUCTION

Silicon is not a substance that lends itself readily to optical spectroscopic studies. The various TM related spectra arise from impurity levels lying within the energy gap of the host crystal. and since Si has a band gap $\approx$ 1.1 eV the luminescence lies in the near-infrared part of the electromagnetic spectrum. Excitons bound to some defects in Si have binding energies of the order of 10 - 50 meV and so dissociate thermally at temperatures above 60 K. Thermal broadening of the luminescence sets an effective limit to the spectral resolution possible between any closely spaced features for temperatures above 25 K. For both these reasons most spectra have to be recorded at sample temperatures below 25 K. The spectra lie in the region from 1 to 2 μm which unfortunately also includes areas strongly affected by water vapor absorption. Unless corrected this absorption can distort a region that might otherwise exhibit finely detailed luminescence features.

The experimental apparatus and computer software used to obtain the spectra at these temperatures and to compensate for the water vapor absorption are described below.

4.2 SAMPLE PREPARATION

The standard procedure for introducing transition metals (T.M.'s) into the silicon was to heat them in the presence of the metal in a sealed quartz tube for a varying number of hours. The samples used were nominally p-type, high resistivity (20 kΩcm), zone refined Hoboken Si ingots of typical dimensions 12mm X 4mm X 2mm. After initial cutting the samples were etched in a 8:1 mixture of HNO_3 and HF to remove any damaged surfaces left over from the previous processes and also to remove any contaminants left on their surfaces from the saw blade. They were then rinsed thoroughly

in de-ionized water before being dried and placed in a clean quartz test tube along with small masses (≤ 2g) of whichever T.M. we wished to introduce. All the T.M.'s used were at least 99.99 % pure. A smaller bore quartz test tube was then placed inside as well, and the complete assembly was connected to a vacuum system and evacuated. An oxy-acetylene welding torch burning a mixture of hydrogen and oxygen was then used to melt the outer tube onto the inner tube thus forming a vacuum tight seal all the way around a (hopefully) contaminant-free volume for the diffusion to take place. (see Fig.3.1).

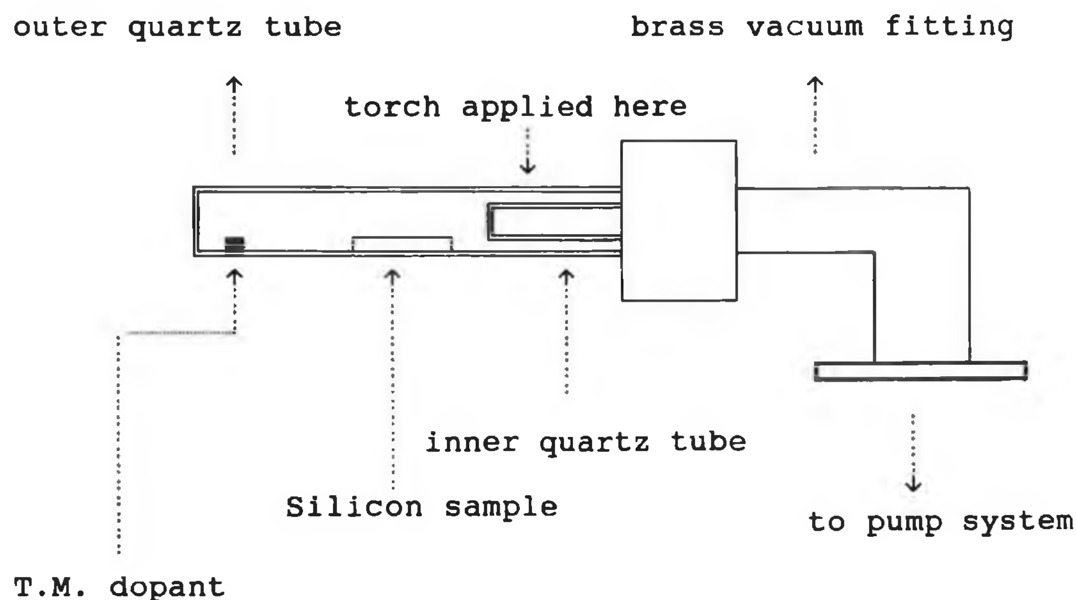

Fig. 4.1 Quartz tube and vacuum assembly used in the TM diffusion process.

4.3 DIFFUSION METHODS

For most of the samples diffusion took place in a furnace at 1100°C and the time varied from under 2 hours to over 16 hours depending on the diffusivity or solubility of the T.M. in question.

This method of diffusing impurities into Si has the following advantages :

(1) The vacuum inside the quartz tube prevents

an oxide layer forming on the Si surface. An oxide layer can sometimes seal the surfaces and bring the diffusion process to a stop.

(2) At high temperatures the diffusants evaporate and since the tube is sealed they achieve a very high vapour pressure which aids the diffusion process

The procedure used to create the Cu^* system differed from the normal method. The samples were cut from an ingot of

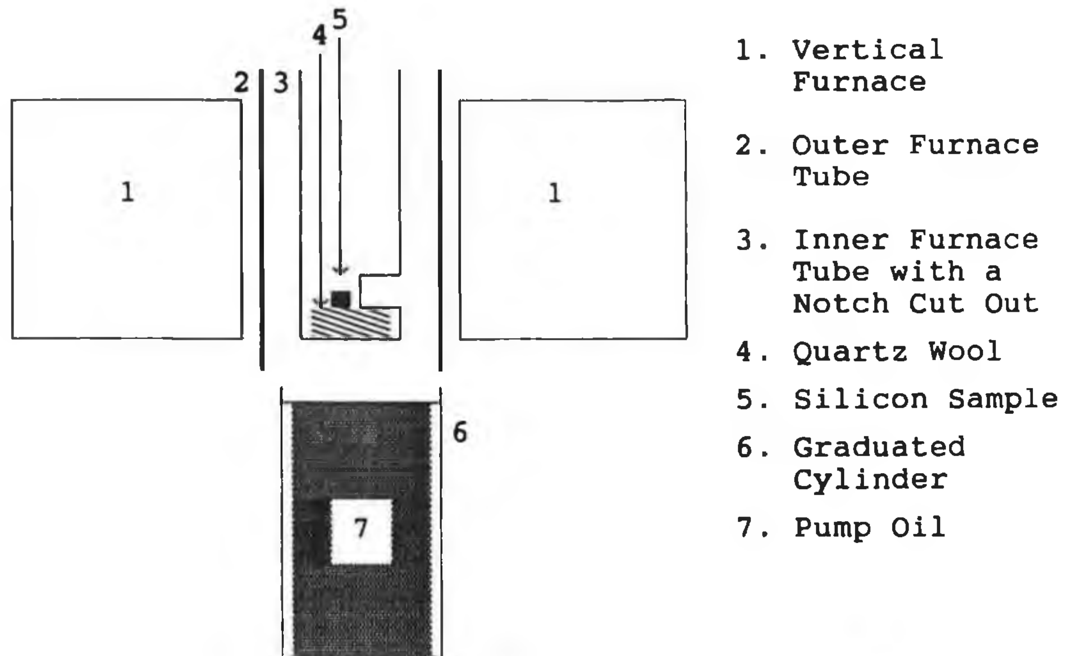

Fig 4.2 The furnace assembly used to create the Cu^* system.

copper diffused silicon with a concentration of approximately 10^{13} cm^{-3} measured by atomic absorption. These were then etched and washed in the usual manner and placed in a clean, open quartz furnace tube with a notch cut in the bottom . The tube was placed in a Carbolite CFM 1200 vertical furnace pre-heated to $1100^{o}C$. After 2 minutes the samples were quenched by shaking the inner furnace tube vigorously until the sample fell through the notch and down into a 100 cc graduated cylinder of rotary pump oil positioned directly underneath the furnace tube assembly, as illustrated in Fig. 4.2.

4.4 SAMPLE QUENCHING

Usually the samples were quenched down to room temperature by quickly removing the sealed tube from the furnace and dropping it into a water bath. Invariably the quartz tube shattered or cracked but the samples were usually undamaged and on average a quench rate of approximately $400^{o}C/$ second was achieved.

The necessity for a long path length of oil to quench the Cu^{*} samples cannot be over emphasized. If the path length was under 10 cm then the sample tended to lay on the bottom of the container cooling in a surrounding layer of warm oil and obviously not quenching as fast as possible.

The samples were then rinsed in acetone to remove any residual oil and then mounted in the cryostat.

4.5 LOW TEMPERATURE APPARATUS

Two different cryostats were used to cool the samples down to the low temperatures needed to observe the luminescence.

The first was an Air Products CS202W cryogenic refrigerator that used helium gas as the cryogen. Thermal contact between the sample and the primary heat station was achieved using Crycon grease which has high thermal conductivity at low temperatures. A chromel-alumel thermocouple and a small heater circuit, both attached to the cold-finger and connected to a standard Air Products temperature controller were used to measure and control the sample temperature. The cold finger was enclosed in a radiation shield attached to the secondary heat station of the refrigerator that kept it at a temperature of around 80 K. This in turn was surrounded by a steel vacuum shroud in contact with the ambient laboratory atmosphere. The sample space was evacuated by a diffusion pump backed by a rotary pump, maintaining a vacuum of about 10^{-6} Torr. Since the sample was only in indirect contact with the primary heat station i.e. via the indium gasket and the Crycon grease, heat losses throughout the system limited the lowest attainable temperature to around

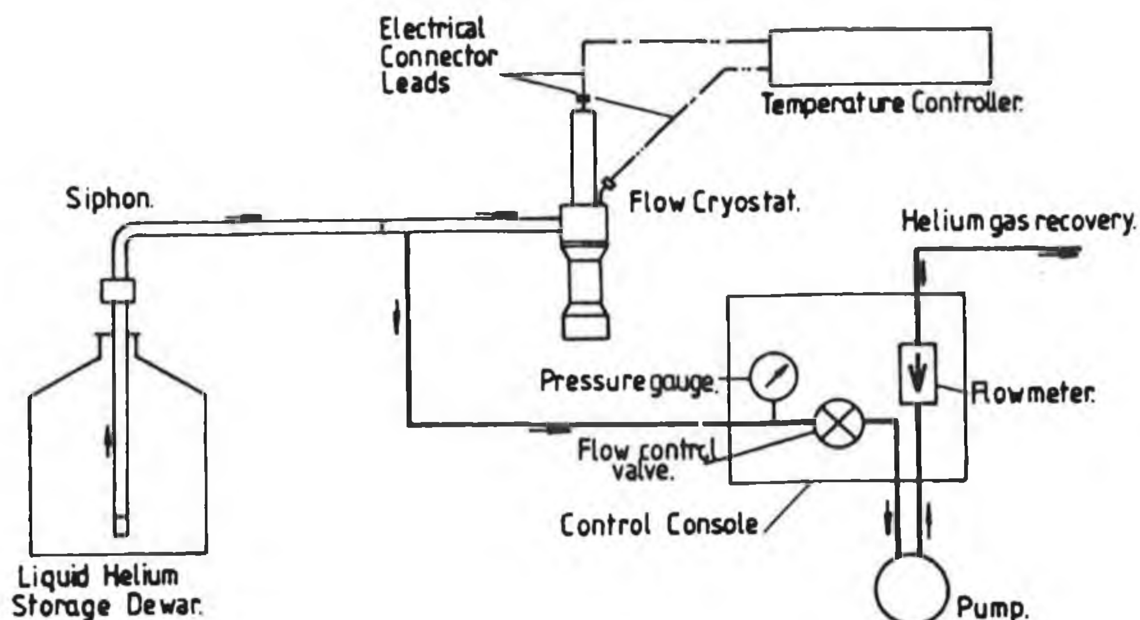

Fig.4.3 Schematic diagram of the Helium flow cryostat system

12 Kelvin.

To attain lower sample temperatures a Thor C584 liquid helium flow cryostat was used. This worked by pumping the liquid helium from a 30 litre capacity dewar through a transfer siphon to an annular reservoir surrounding the sample space in the cryostat. The sample was strapped to a central sample stick using P.T.F.E. tape and research standard helium gas at a pressure of one atmosphere was used as the exchange medium between the annular reservoir and the sample. Both the annular reservoir and the sample stick had a DT500 silicon diode temperature sensor and a 100 Ω heater resistor fitted to measure and control the sample space temperature, respectively. The helium flow cryostat system is illustrated in Fig. 4.3.

This system enabled us to reach sample temperatures right down to 4.2 K but unfortunately owing to the large expense involved in purchasing and transporting liquid helium from the U.K. only limited use of the flow cryostat was possible.

4.6 OPTICAL ARRANGEMENT

The luminescence was excited by either of two sources; the 514 nm line of type 52 Coherent 3 watt argon ion c.w. laser or a narrow band centred at approximately 918 nm from an Ealing type 1207 150 watt xenon arc lamp filtered through a Spex Minimate 0.25 m focal length Czerny-Turner spectrometer fitted with a grating ruled at 600 lines / mm with a blaze wavelength of 1.0 μm for improved performance in the infrared.

The lens geometry about the sample varied according to which cryostat was used. The helium flow cryostat had one axial and four equally spaced radial windows which meant that the luminescence was collected normal to the incident exciting radiation.

The Air Products cold-finger was centrally mounted allowing us to machine the radiation shield and the vacuum shroud such that they incorporated an angle of 135° between the inlet and outlet window. As can be seen in Fig. 4.4 the

1. STEEL VACUUM SHROUD
3. SAMPLE MOUNT
4. SAMPLE
5. GLASS WINDOWS
6. VACUUM
7. EXCITATION BEAM

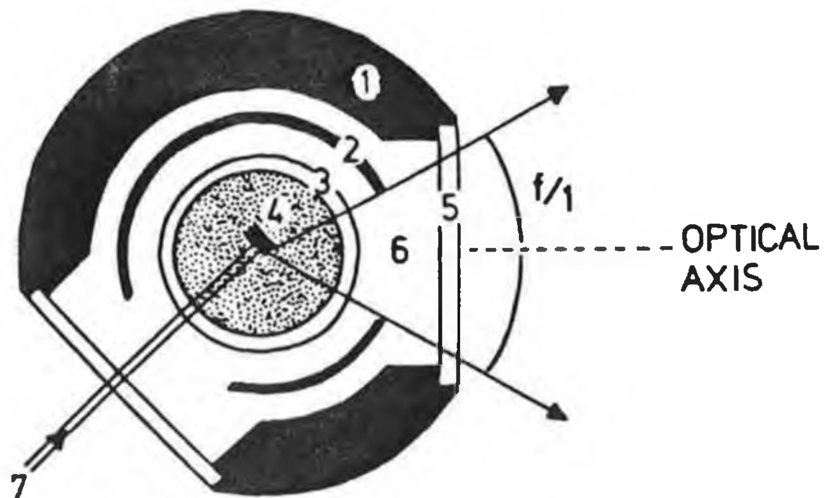

Fig. 4.4 Geometry of the closed cycle system sample mount.

luminescence originating from the small area excited by the incident radiation, is refracted through quite large angles

as a result of the high refractive index change at the Si-vacuum interface. Placing the optical axis of the aspherical collecting lens at an angle of 135 $^{\circ}$ to the incoming excitation enabled us to collect the luminescence much more efficiently off the edges of the sample.

The luminescence was focused onto the entrance slits of a Spex 1704, 1m focal length Czerny-Turner spectrometer fitted with grating ruled at 600 lines / mm with a blaze angle of 1.2 μm The slitwidths on the spectrometer were usually set to 200 μ (except in the case of uniaxial stress measurements) which gave a resolution of approximately 0.2 meV compared to the minimum line separation in the Cu^{*} system of 0.57 meV. The grating was controlled by a B.B.C. microcomputer via a Spex mini-step-driver unit. The " SPEXDR " program to do this is included in the Appendix.

4.7 SIGNAL PROCESSING

A North Coast EO-817 germanium detector was attached to the exit slit of the monochromator. This consists of a reverse biased (-100 V) p-i-n diode and a low noise pre-amplifier. Both the diode and the F.E.T. in the first stage of the pre-amp were cooled with liquid nitrogen stored in a dewar in the casing. These combined to give a highly sensitive (responsivity = 4×10^{8} V/W), low noise performance in the 0.8 μm to 1.8 μm spectral region. This model had both A.C. and D.C. outputs to facilitate the use of either a lock-in amplifier or an analog to digital converter for computer storage of spectra.

The detector was very sensitive to cosmic rays and background radiation, both of which tended to induce large sudden voltage surges on the detector output signal. An electronic spike removal unit (S.R.U.) based on a design by Collins (1982) was built to remove these effects. Basically it consisted of a sample-and-hold chip and a differentiating amplifier to both of which the detector output was applied. A voltage spike emerging from the detector created a large output from the differentiator

triggering a monostable flip-flop which in turn froze the sample-and-hold circuit in the hold mode for a time approximately equal to the response time of the detector thus blocking the undesired spike.

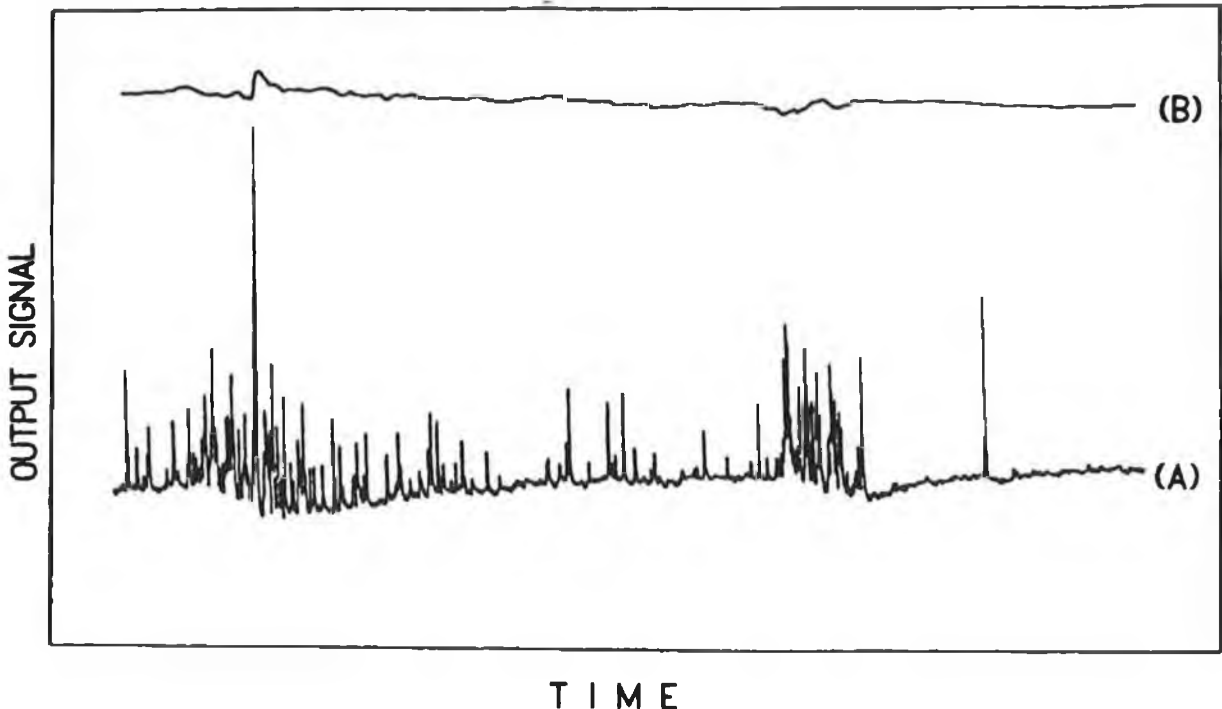

Fig. 4.5 (a) Detector output showing spikes caused by a nearby γ - source. (b) The S.R.U. output of the same signal with the spikes suppressed.

Fig. 4.5 shows the output from the detector with a radiation source held next to it (A), and the same signal as it emerges from the spike removal unit (B).

The output from the S.R.U. was connected to a Rikadenki x-t chart recorder for immediate display or alternatively it could be stored on disc by the B.B.C. computer using the SPEXDR program in conjunction with an analog to digital converter. It was this facility to store spectra on disc that enabled us to compensate for the effect of water vapor absorption. This was done by first recording the luminescence spectra on disc and then recording the water vapor absorption spectra of a calibrated tungsten lamp using the same start, finish, and stepsize parameters. The water vapor absorption spectrum was then divided into the luminescence spectrum in a computer array to give the final corrected spectrum. The

same procedure can be applied to absorption spectra and in Fig. 4.6 the uncorrected and corrected spectra for the absorption of Si:Be (Maloney 1986) are shown to illustrate the importance of applying the correction.

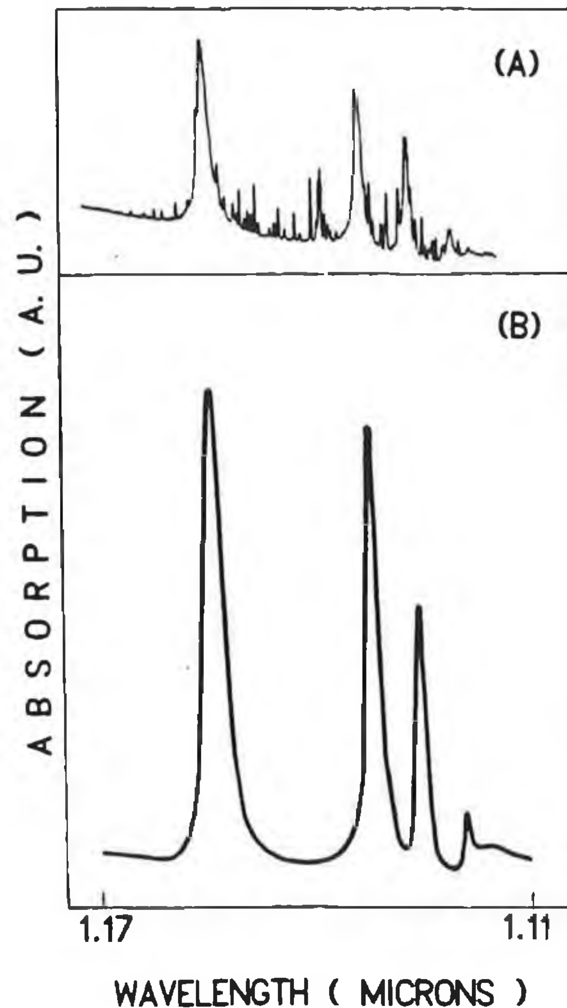

Fig. 4.6 (a) The absorption spectrum of Si:Be with overlapping water vapour features. (b) The final computer compensated spectrum over the same spectral range.

A schematic layout of the data collection apparatus is given in Fig. 4.7

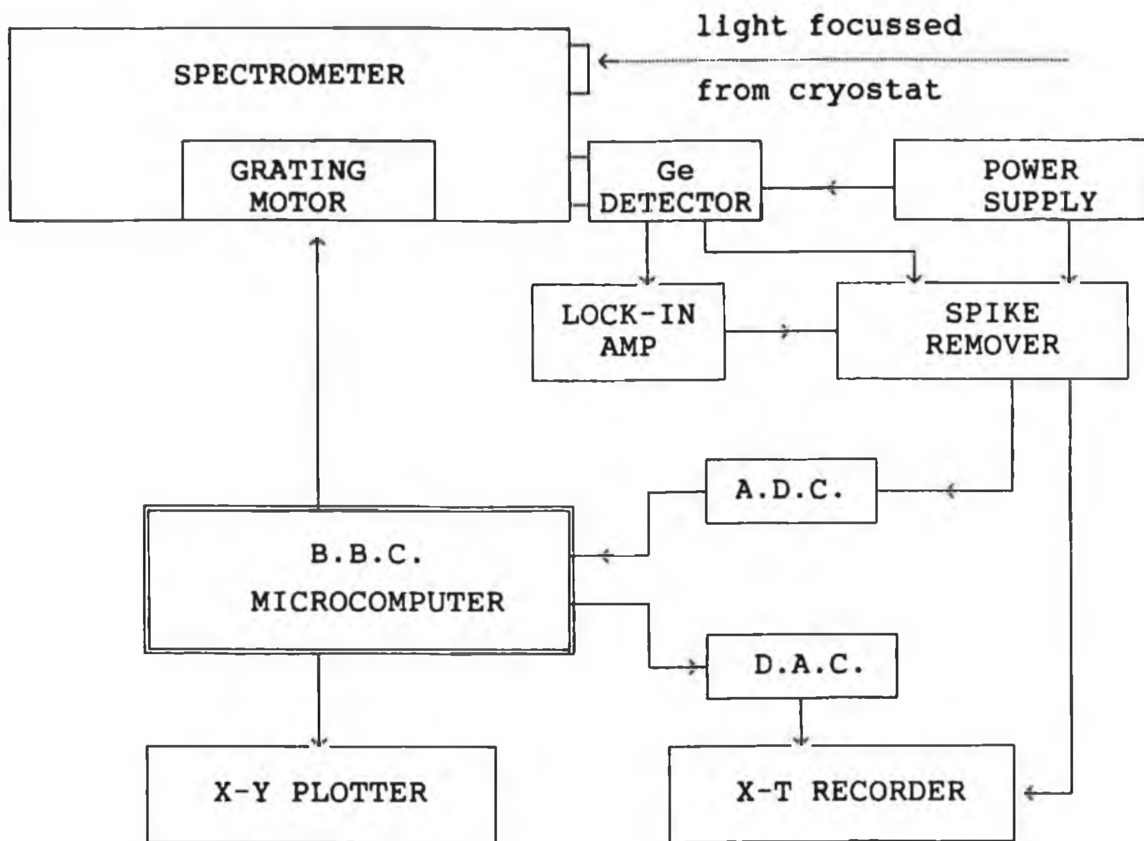

Fig. 4.7 Schematic diagram of the signal processing apparatus

4.8 STRESS CELL

The stress cell used in the uniaxial stress experiments is shown in Fig. 4.8. It was machined out of stainless steel and consisted of an outer hollow cylinder with four radial windows positioned near the bottom and a vacuum flange welded onto the top such that when inserted into the He-flow cryostat the stress cell windows coincided with those of the cryostats. An oriented sample was mounted, using double sided adhesive tape, exactly perpendicularly to the surface of a small threaded insert with a machined flat surface which was then threaded into the bottom of the assembly such that the long axis of the sample was exactly parallel with the vertical axis of the stress cell. A small freely moving push rod with machined ends was brought carefully in contact with the remaining end of the sample. A second, longer, push rod was rested on top of the first in such a way as to leave the

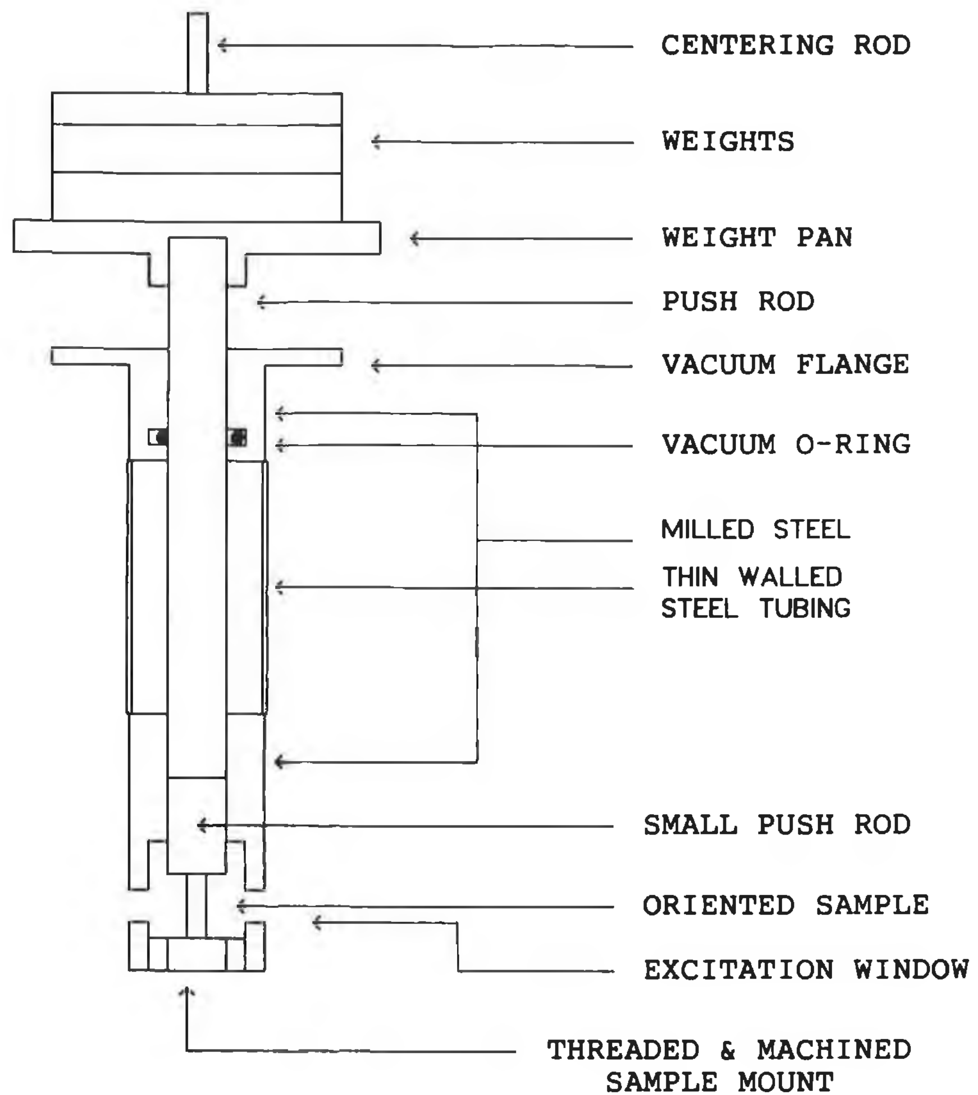

Fig. 4.8 Diagram of the stress cell used in the uniaxial stress experiments.

opposite end free from the whole assembly. A weight pan was secured onto this end and the stress that the sample experienced was varied by changing the number of weights placed on the pan.

A vacuum could be maintained inside the cryostat with the stress cell inserted through the use of a vacuum o-ring positioned on the inside of the stress cell in contact with the long push rod. Table 4.1 gives the calibration table for the stress cell when samples of cross sectional dimensions

1.5 X 3 mm are used.

A rough empirical conversion equation for the load - to pressure relationship is given in Eq. 4.1

$$P = (M + .68) \times 2.31 \qquad (4.1)$$

where P = the resultant pressure in MPa
M = the applied load in kg
.68 = the mass of the push rod assembly and weight pan in kg.

LOAD (kg)	PRESSURE (MPa)	LOAD (kg)	PRESSURE (MPa)
1	3.88	12	29.32
2	6.20	13	31.64
3	8.50	14	33.95
4	10.82	15	36.26
5	13.13	16	38.57
6	15.45	17	40.89
7	17.76	18	43.2
8	20.07	19	45.51
9	22.39	20	47.82
10	24.70	21	50.14
11	27.01	22	52.45

Table 4.1 Calibration table for the stress cell when using samples of cross-sectional dimensions 1.5 X 3 mm

CHAPTER 5 : EXPERIMENTAL RESULTS

5.1 INTRODUCTION

Effective mass theory has proved reasonably successful in explaining the observed features in the absorption and excitation spectra of donor and acceptor impurities in many semiconductor materials (Fisher and Ramdas 1969). However, even though double acceptors such as Zn and Hg have been found to behave much as expected in Ge (Fisher 1960,1966 and Chapman 1967), this is not so in the case of Si. It was for this reason that we decided to examine zinc and zinc-related PL defects in silicon. Initial experiments involving silicon diffused with zinc only, failed to uncover any new PL spectra, so we decided to concentrate our investigations on the co-diffusion of zinc with other 3d transition metals. Ludwig and Woodbury (1962) had previously shown that strong EPR signals could be obtained from TM interstitial donor - substitutional acceptor pairs in silicon. It was our intention to study any corresponding PL spectra arising out of such co-diffused samples.

5.2 Zn-RELATED PL STUDIES

5.2.1 THE 944.8 meV Zn-RELATED PL SYSTEM

The first combination of TM's that were co-diffused into Si were Mn & Zn. Mn was chosen because Ludwig & Woodbury observed a strong EPR signal from a centre that they identified as Mn_i - Zn_s in 1962 but despite this no subsequent studies of luminescence studies on silicon doped with this combination of TM's were reported.

The diffusion was carried out using the sealed quartz tube method outlined in the previous chapter, at 1150^{oC} over 16 hours with a fast quench into a water bath at the end. Samples treated in this manner did produce a new PL spectrum. As can be seen from Fig. 5.1 (taken from Henry et al. 1988)

ENERGY meV	IDENTIFICATION	REMARKS
945.8	$Mn\text{-}Zn^{0}_{1}$	zero phonon
944.8	$Mn\text{-}Zn^{0}_{0}$	zero phonon
935	$Mn\text{-}Zn^{1}_{0,1}$	10.3 meV phonon rep.
926	$Mn\text{-}Zn^{ac}_{0,1}$	19.3 meV phonon rep.
910	$Mn\text{-}Zn^{1'}_{0,1}$	35 meV phonon rep.
882	$Mn\text{-}Zn^{O^{\Gamma}}_{0,1}$	O^{Γ} phonon rep.
871	$Mn\text{-}Zn^{1+O^{\Gamma}}_{0,1}$	
862	$Mn\text{-}Zn^{ac+O^{\Gamma}}_{0,1}$	
847	$Mn\text{-}Zn^{1'+O^{\Gamma}}_{0,1}$	
818	$Mn\text{-}Zn^{2O^{\Gamma}}_{0,1}$	

Table 5.1 Spectral features of the Mn-Zn system

this spectrum consists of a thermalizing zero-phonon doublet at 944.8 & 945.8 (± 0.1) meV accompanied by a number of different energy phonon replicas and a broad phonon sideband that dominates the spectrum at all temperatures indicative of strong phonon coupling. The energies, labelling and identifications of the main features in the spectrum are listed in Table 5.1. In the notation used the subscript denotes the electronic level of the state from which the transition originates and the superscript denotes the number and type of phonons involved with the transition.

The intensity of the feature marked with an asterisk in Fig. 5.1 was found to be excitation wavelength dependent and was later observed in samples implanted with Zn only (M. O.

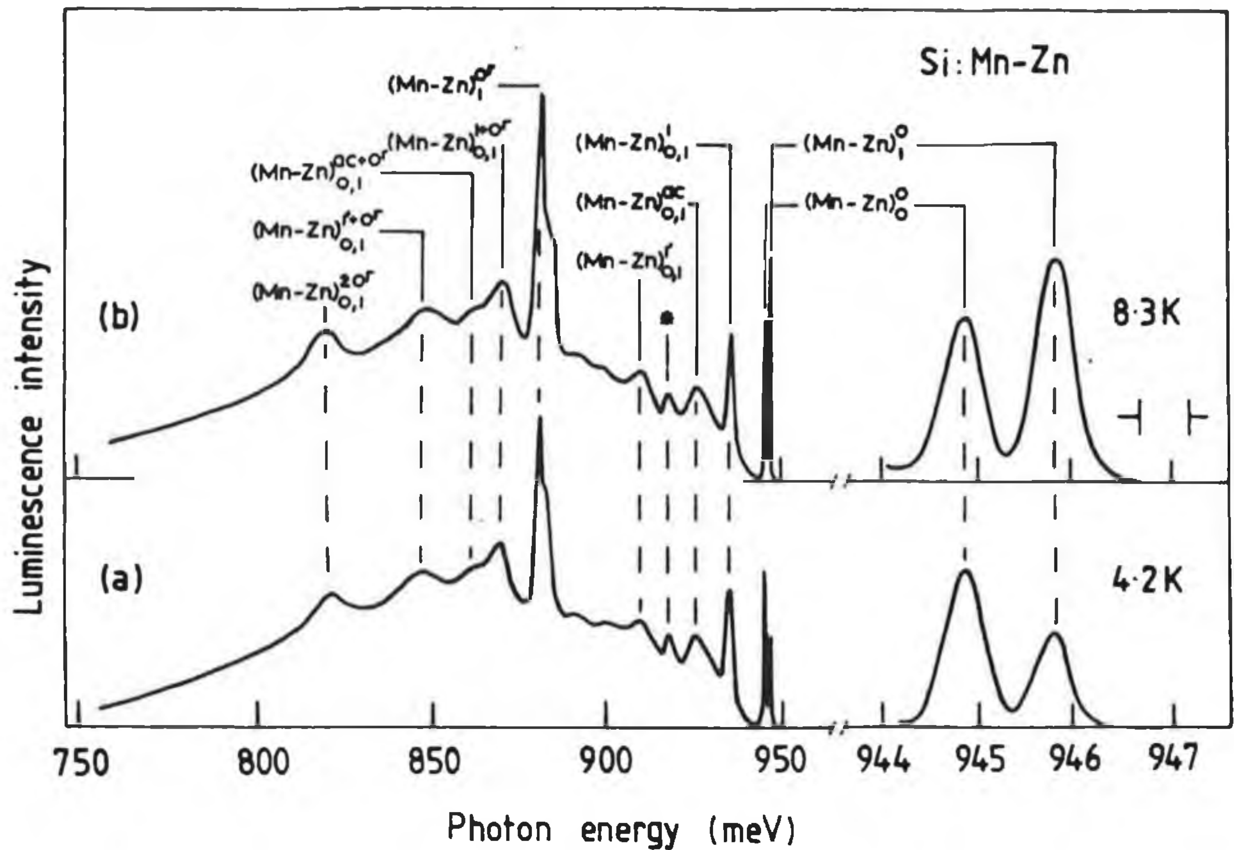

Fig. 5.1 PL spectra of the .945 eV Mn-Zn system

Henry private communication 1987) and as such is not thought to be intrinsic to the defect under consideration.

The log of of the relative intensities of the 2 ZPL components as a function of inverse temperature (shown in Fig. 5.2) yields a thermal activation energy of 0.933 (± 0.2 eV) in good agreement with the spectral separation of the two lines (1.0 meV) suggesting that both excited states depopulate into the same ground state leading to the very simple energy level diagram shown in Fig. 5.3.

The ratio of infinite temperature transition probabilities, derived from the same thermalisation data, was found to be ;

$$Mn\text{-}Zn_0^0 : Mn\text{-}Zn_1^0 = 1 : 8$$

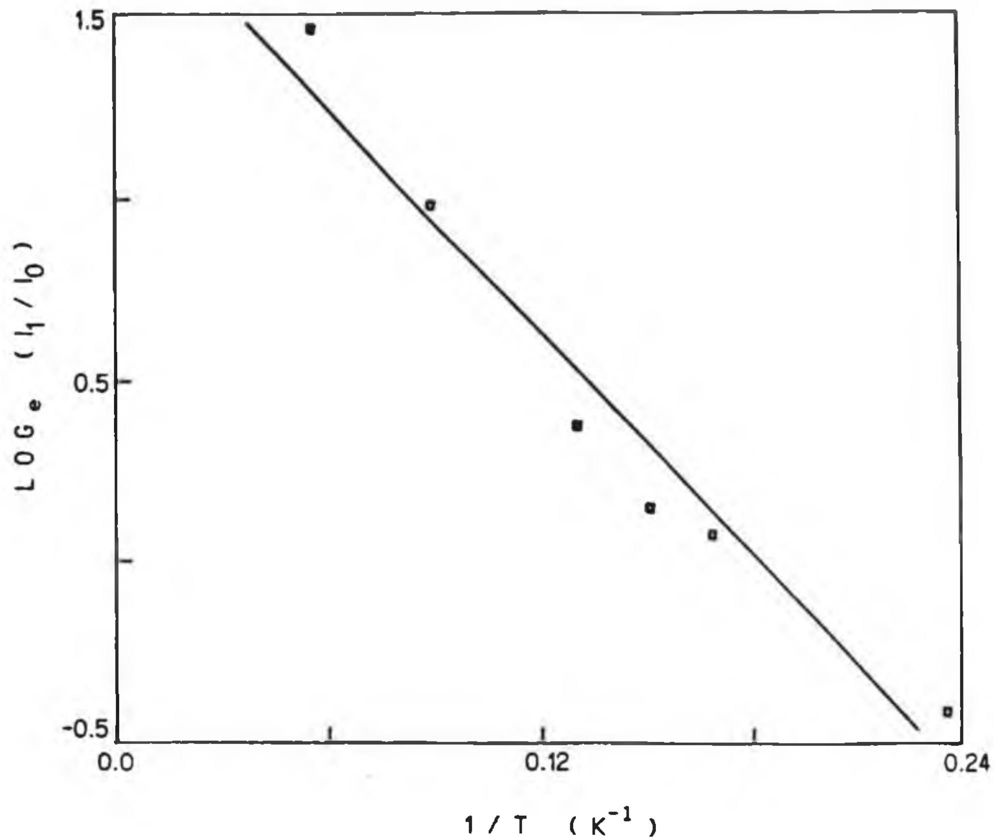

Fig. 5.2 Arrhenius plot of the log of ratio of intensities of the two zero phonon lines versus inverse temperature.

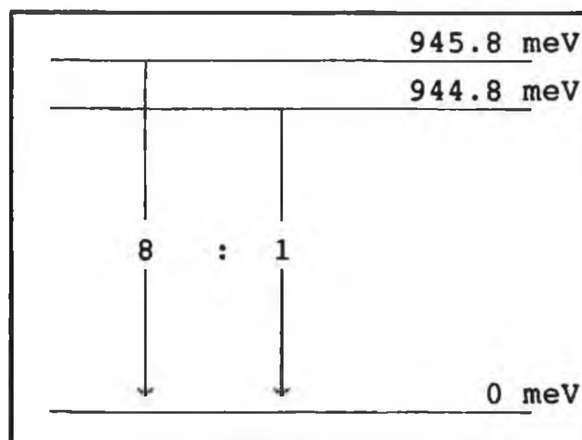

Fig. 5.3 Energy level diagram of the Mn-Zn system.

The total luminescence intensity as a function of temperature is illustrated in Fig. 5.4. Below 20 K the system behaves much as we would expect it to with the luminescence

increasing as the levels become more populated and more phonons are coupled to the transition. The intensity levels off at around 20 K but instead of gradually decreasing as the excitons thermally decay, the overall luminescence begins to increase again between 25 & 35 K. This can be explained by assuming that shallower traps lose excitons bound to them as the temperature increases thus indirectly populating the PL level by making more excitons available for capture by the Mn-Zn traps as explained in section 2.9. This explains why

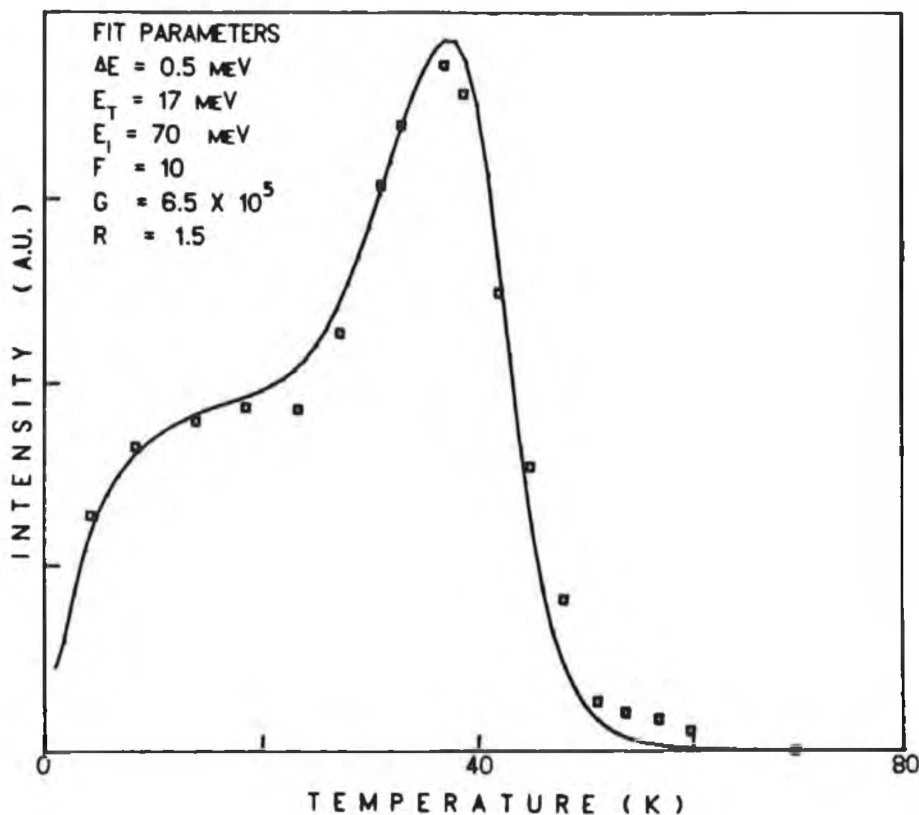

Fig. 5.4 Plot of the total luminescent intensity vs. sample temperature for the 945 meV PL system.

this process only begins at temperatures above 25 K. An Arrhenius plot over the range 23 K to 40 K yields a line whose slope corresponds to an activation energy of 10 meV (± 1.5 meV). A simplified energy level diagram illustrating this process is shown in Fig. 5.5.

The decrease in intensity after 38 K can be explained by

thermal decay of the excitons bound to the PL defect. An Arrhenius plot over the 40 K to 60 K temperature range gives a line whose slope corresponds to the thermal activation energy of the exciton, in other words the binding energy of the secondary component of the exciton bound to the centre. In this case this was found to be equal to 75 meV (± 8 meV). A reasonable fit to the data presented in Fig. 5.4 was obtained using the expression given in Eq. 5.1.

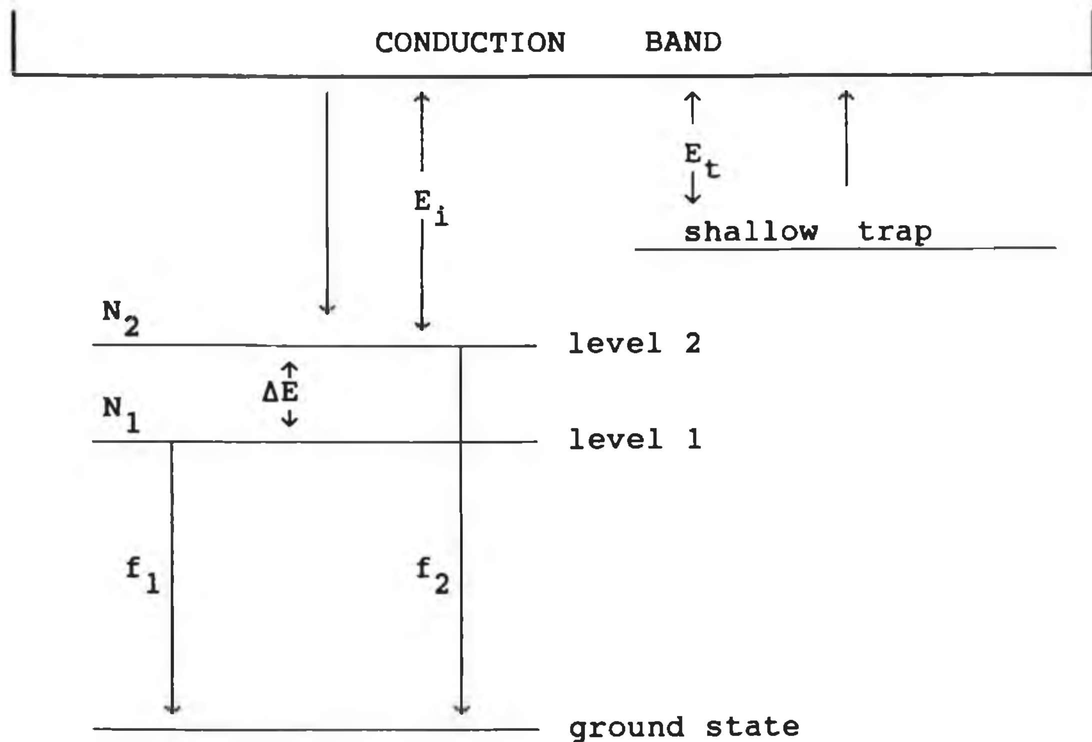

Fig. 5.5 Simplified energy level diagram showing the interaction of a non-radiative level and how it can still contribute to the overall luminescent intensity.

$$I_{tot}(T) = I_o \cdot F_1(T) \cdot F_{trap}(T) \cdot F_{decay}(T) \qquad (5.1)$$

where

I_o = the total intensity at 0 K

$$F_1(T) = (1 + \frac{f_1}{f_2} . g_{21} \exp(-\Delta E/kT) / (1 + g_{21} \exp(-\Delta E/kT)$$

$$F_{trap}(T) = 1/(1 + (r.f))$$

where $$f = 1/(1 + GT^{3/2}.\exp(-E_t/kT))$$

$$F_{decay}(T) = 1/(1 + GT^{3/2}.\exp(-E_i/kT))$$

where each variable has the same meaning as explained in section 2.9 or as is obvious from Fig. 5.5.

The experimentally measured and fitted parameters are compared below:

	EXPERIMENT	FIT
ΔE	0.933 meV	0.5 meV
E_t	10.0 ± 1.5 meV	17 meV
E_i	75.0 ± 8 meV	70 meV
$\frac{f_1}{f_2}$	8.0 ± 1	10

with

$$g_{21} = 2.5$$

$$G = 6.5 \times 10^5$$

$$r = 1.5$$

This fit is shown in Fig. 5. 4 as the solid line.

EPR was carried out on two of the best PL samples. In each case no signal was detected at room temperature but at 77 K a strong signal was observed that was identical to that identified by Ludwig & Woodbury (1962) as being from Mn_i-Zn_s centres,(shown in Fig. 5.6). The PL & EPR signals both only occurred in samples co-diffused with Mn and Zn. Samples diffused singly with Zn or Mn and others co-diffused with Mn-B, Zn-B, Mn-P and Zn-P, gave no signal in either EPR or

PL.

It was on this fairly strong evidence that the 945 meV PL band was assigned to bound exciton recombination at the Mn-Zn centres known to exist in the samples (Henry et al. 1987). The infinite temperature ratio of the two zero phonon lines (8:1) is typical of the triplet - singlet ratio observed for IBE's in silicon. To confirm this assignment, Zeeman measurements were attempted. It was not possible to obtain definitive data in the experiment due to poor signal levels, however the the lower energy zero phonon line broadened in a manner consistent with that expected for a J=1 to J=0 transition assuming a g-value of 2. These are shown in Fig. 5.7 where the observed line shape is compared to a calculated lineshape (assuming g=2 and allowing for the effects of thermalisation).

The triplet identity for the excited state of the 945 meV line was also examined using ODMR in an attempt to find a direct correlation between the Mn-Zn EPR and PL signals but the signal levels were again too weak to provide any useful data.

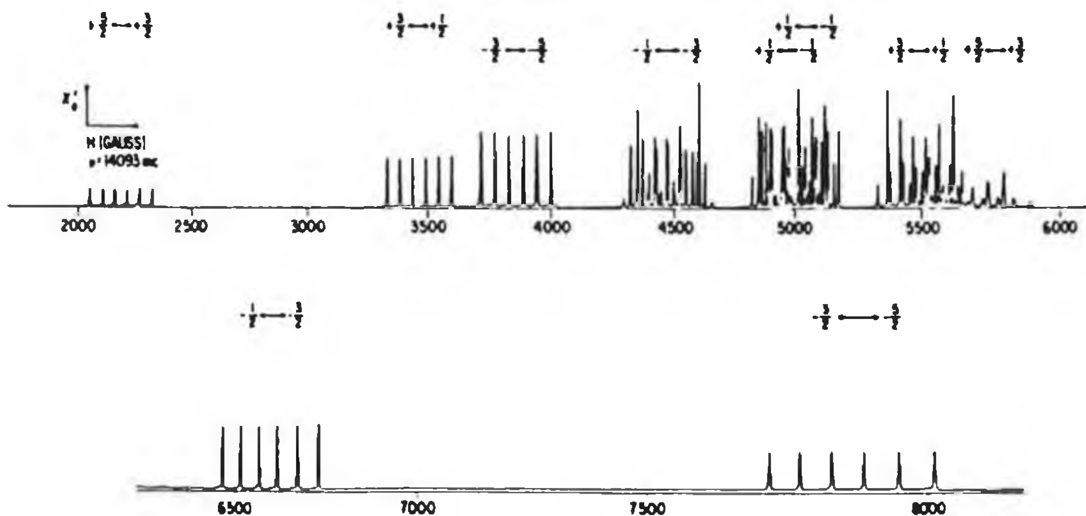

Fig. 5.6 The EPR spectrum of Mn_i- Zn_s observed by Ludwig et al. (1962) and also detected in samples that exhibited the 945 meV luminescence system.

Subsequent studies on samples co-diffused with Cr-Zn, Pt-Zn, Ni-Zn and Fe-Zn all produced the so called Mn-Zn PL centre with the signal from the Fe-Zn sample being by far the strongest yet seen. EPR studies on all these samples failed to detect any Mn-Zn signal. The only system detected being a strong Fe^{3+} signal in the Fe-Zn sample (R. C. Barklie private communication).

It is therefore clear that the Mn-Zn identification for the 944.8 meV PL system is incorrect. The only conclusion that can safely be drawn is that the defect involves Zn since it is detected only in samples that were co-diffused with Zn.

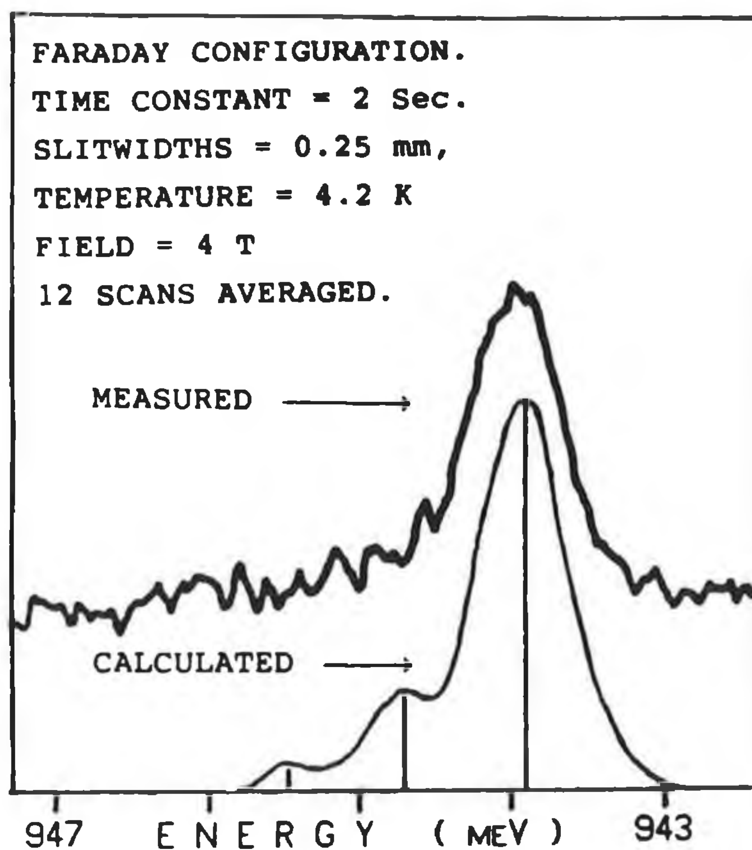

Fig. 5.7 Observed and theoretical Zeeman splittings for the 945 meV ZPL lines for a temperature of 4.2 K, a field value of 4 T and a g-value of 2.

For this reason a more appropriate labelling for the system

would be Zn^* (this notation will be used from now on when referring to this PL system). If there is another TM impurity involved in the defect (which there probably is since this PL centre is not observed in Si diffused with Zn only) then the evidence points towards this being Fe, a common contaminant in most as-grown Si. This theory is further supported by the strength of the Zn^* spectrum in the Si:Fe-Zn sample (a factor of ≈3 times stronger than any seen previously).

In summary the spectral position of the Zn^* luminescence, the observed rapid decrease in intensity for T > 40 K, its simple ZPL structure and strong phonon coupling, are all characteristic of IBE recombination at a TM related defect in Si (Dean & Herbert 1979). Diffusion studies indicate that zinc is involved in some way in the defect along with some other impurity possibly iron. The infinite temperature intensity ratio for the two ZPL's is consistent with that expected for a singlet - triplet energy level as described in section 3.7 . In this case the triplet evolves from an allowed J=1 to J=0 transition while the higher energy singlet is derived from a forbidden J=0 to J=0 transition. Zeeman studies to confirm this were inconclusive while not being inconsistent with such an assignment.

5.2.2 THE 919 MEV ZN-RELATED PL SYSTEM

It has already been pointed out that preventing accidental contamination by unwanted impurities during high temperature diffusion experiments is extremely difficult. The contaminants are present in the chemicals used for cleaning the samples, in the quartz of the furnace tubes and in the windings of the furnace elements. Fortunately the two most serious contaminants, copper and iron, are easily identified by their characteristic PL spectra (Weber et al. 1982, Mohring et al. 1986). During the course of the work described in section 5.2.1 several samples nominally diffused with zinc only were found to produce the copper-related 1014

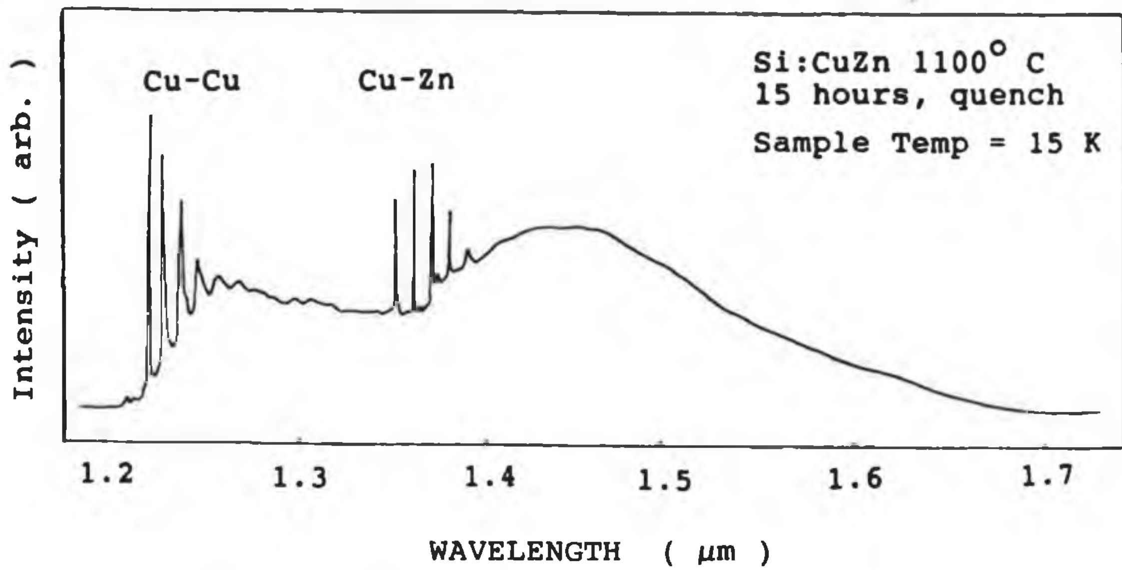

Fig. 5.8 Spectrum of the 919 meV PL system.

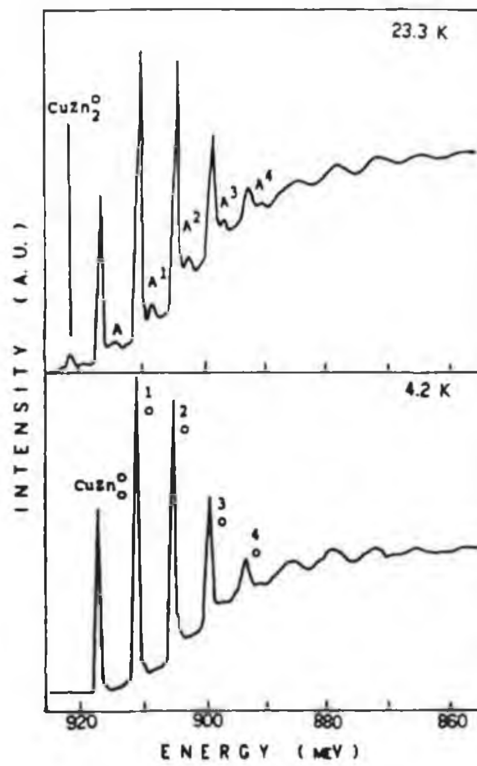

Fig. 5.9 High resolution spectrum of the 919 meV PL system.

meV PL band accompanied by a similar band with a zero phonon line at 919.8 meV. The PL spectrum of one such sample is shown in Fig. 5.8

The PL spectrum (shown in Fig.'s 5.8 & 5.9) consists of two observable ZPL's accompanied by strong phonon coupling in the form of a series of 6.3 meV Stokes and anti-Stokes replicas and a broad phonon sideband extending down to lower energies

This defect, which we will call the CuZn centre was extensively studied by O'Donnell (1988) and accordingly this section will only list his main findings. Fig. 5.10 shows the ZPL level structure for the CuZn system. The intermediate level 3.3 meV above the lowest energy transition is proposed to account for weak fine structure in the phonon sideband.

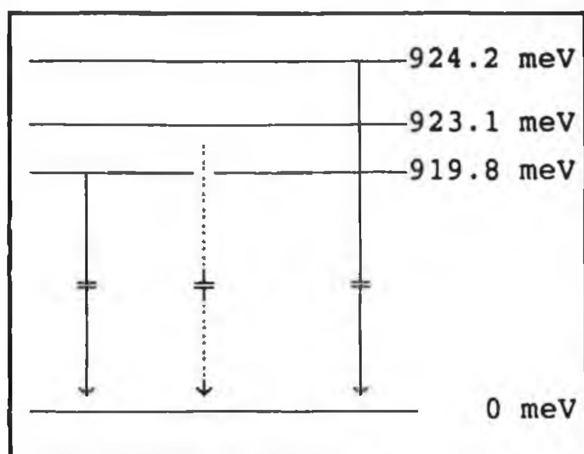

Fig. 5.10 An energy level diagram of the 919.8 meV PL system

The luminescence lifetime was found to be extraordinarily long (9 msec) for temperatures below 50 K with a rapid fall off between 50 and 100 K. The energy level structure and PL lifetimes are consistent with an axial isoelectronic binding centre model with a positive central cell potential, caused by a tensile local strain at the defect, as well as a large electron - hole exchange interaction. A secular matrix similar to that proposed by Davies (1984) constructed by O'Donnell gives an excellent fit to the observed data for a

tensile local strain of 0.14 GPa and an exchange splitting of 14.3 meV. A tentative model of a substitutional Zn atom in association with 2 interstitial Cu^+ ions is suggested.

The behaviour of total luminescent intensity as a function of temperature is shown in Fig. 5.11. The temperature dependence of the total luminescence intensity is seen to be very similar to that observed for the Zn^* system described in detail above. Similar effects are assumed to be responsible in this case. The solid line is a fit made using Eq. 2.18. Here we ignore any small changes in total intensity which may be produced by populating excited states and we combine all the levels together. This approximation could not be made for the Zn^* system since there was a clear increase in total intensity between 4 to 12 K, unlike this system. The fitted parameters are as shown in the diagram. It should be noted that some degree of flexibility between the values of E_i and G is possible which means a similar fit can be achieved with slightly different values for these two parameters. As

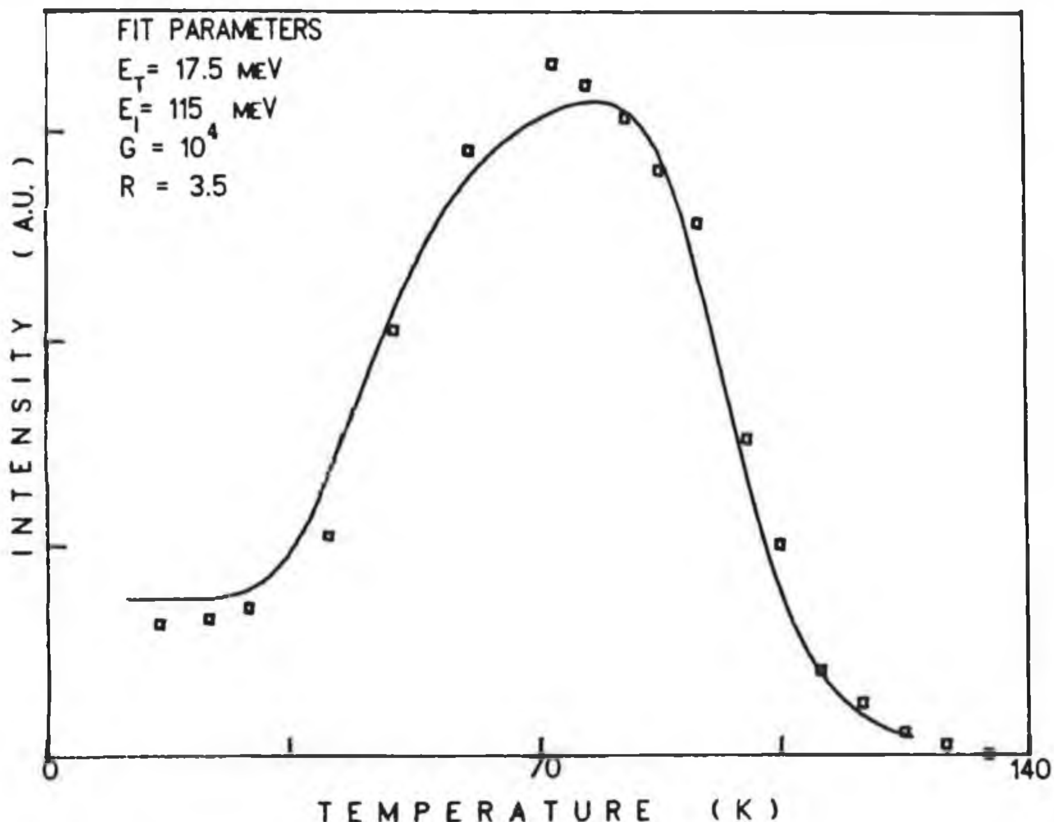

Fig. 5.11 Total luminescent intensity as a function of temperature for the 919 meV PL band.

can be seen from the diagram the luminescence is quite long lived with respect to temperature. For T > 30 K the spectrum consists of a broad featureless band peaking at about 0.885 eV.

5.2.3 THE 1059.9 MEV ZN-RELATED PL CENTRE

Like the 919 meV system this PL band was also first detected while trying to ascertain the chemical identity of the 945 meV Zn^* defect. To this end silicon samples were

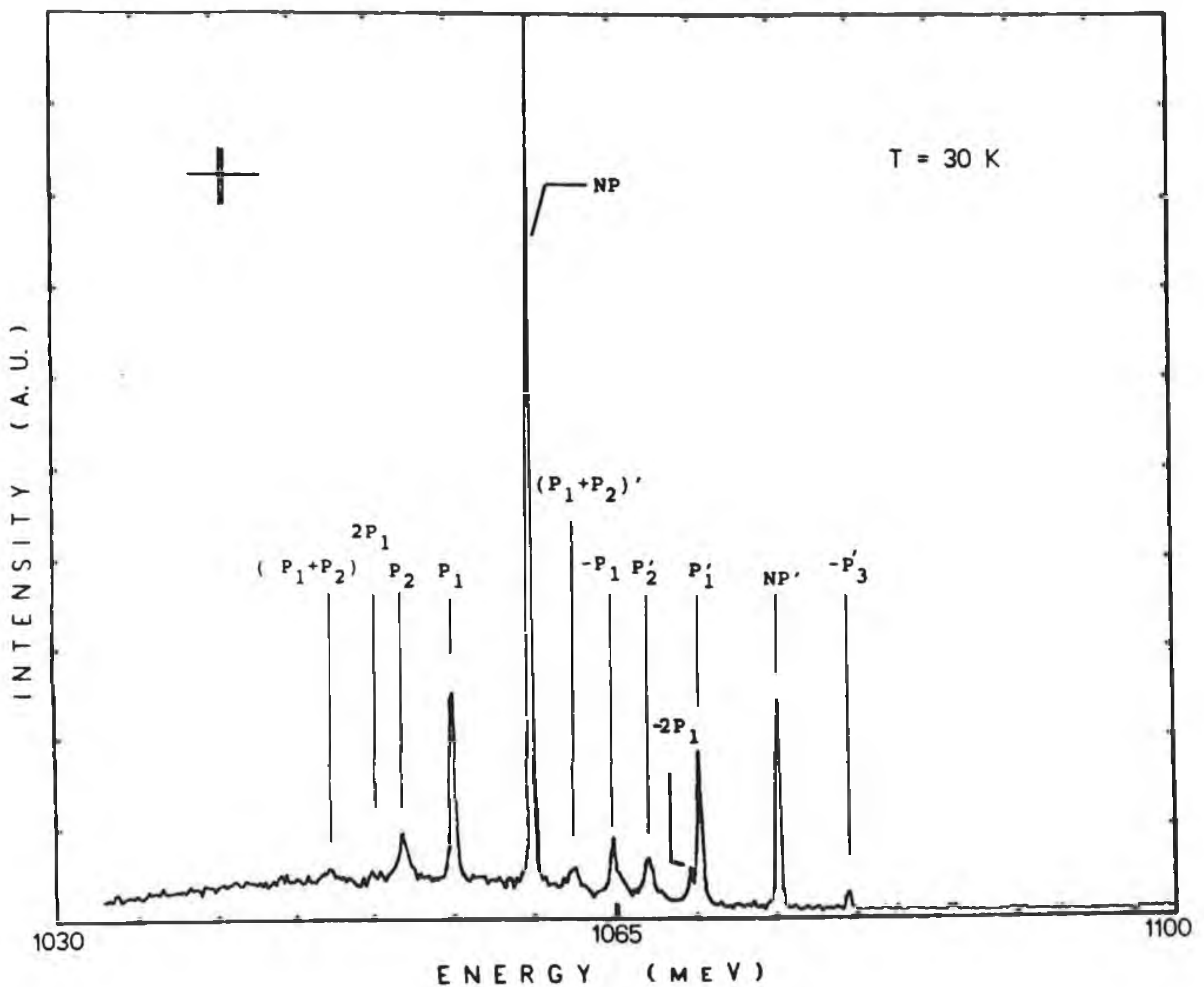

Fig. 5.12 A 30 K spectrum of the 1059.9 meV PL spectrum.

co-diffused with Fe and Zn for 15 hrs at 1050^{oC}and subsequently heated in air at 1100^{oC} for 30 seconds before being quenched in vacuum oil. Two PL bands were found to exist in these samples, one being the 1014 meV copper related system and the other a new system with zero phonon lines at 1059.9 (± 0.2) and 1075.1 (± 0.2) meV.

The PL spectrum is shown in Figures 5.12 and 5.13 (a) for a range of temperatures between 4.2 and 50 K. As can be seen a dramatic change occurs as the temperature increases. Despite the apparent complexity of the spectrum, all the features can be identified. The energies and labels of all the PL features in the system are given in Table 5.2.

The lowest energy no-phonon line occurs at 1059.93 ±.05 meV and is labelled NP. It is accompanied by four Stokes phonon replicas labelled P_1, P_2, $2P_1$ and P_1+P_2, where the phonon energies involved for $P_1$and P_2 are 4.9 meV and 8.0 meV respectively.

LINE	ENERGY meV	SEPARATION meV	LINE	ENERGY meV	SEPARATION meV
NP	1059.9	0	NP′	1075.12	0
P_1	1055.1	4.85	P_1'	1070.2	4.92
P_2	1051.9	7.98	P_2'	1067.1	8.05
P_1+P_2	1047.1	12.78	$P_1'+P_2'$	1062.3	12.85
$2P_1$	1050.2	9.68	$2P_1'$	1065.3	9.84
$-P_1$	1064.8	4.85			
$-2P_1$	1069.6	9.67	$-P_3'$	1079.3	4.22
			$-2P_3'$	1083.3	8.18
O^{Γ}	996.4	63.5	$O^{\Gamma'}$	1011.4	63.70
P_1+O^{Γ}	991.2	68.7	$P_1'+O^{\Gamma'}$	1006.5	68.60
			$-P_3'+O^{\Gamma'}$	1016.0	59.10

Table 5.2 Classification of PL features observed in the Si:FeZn spectrum.

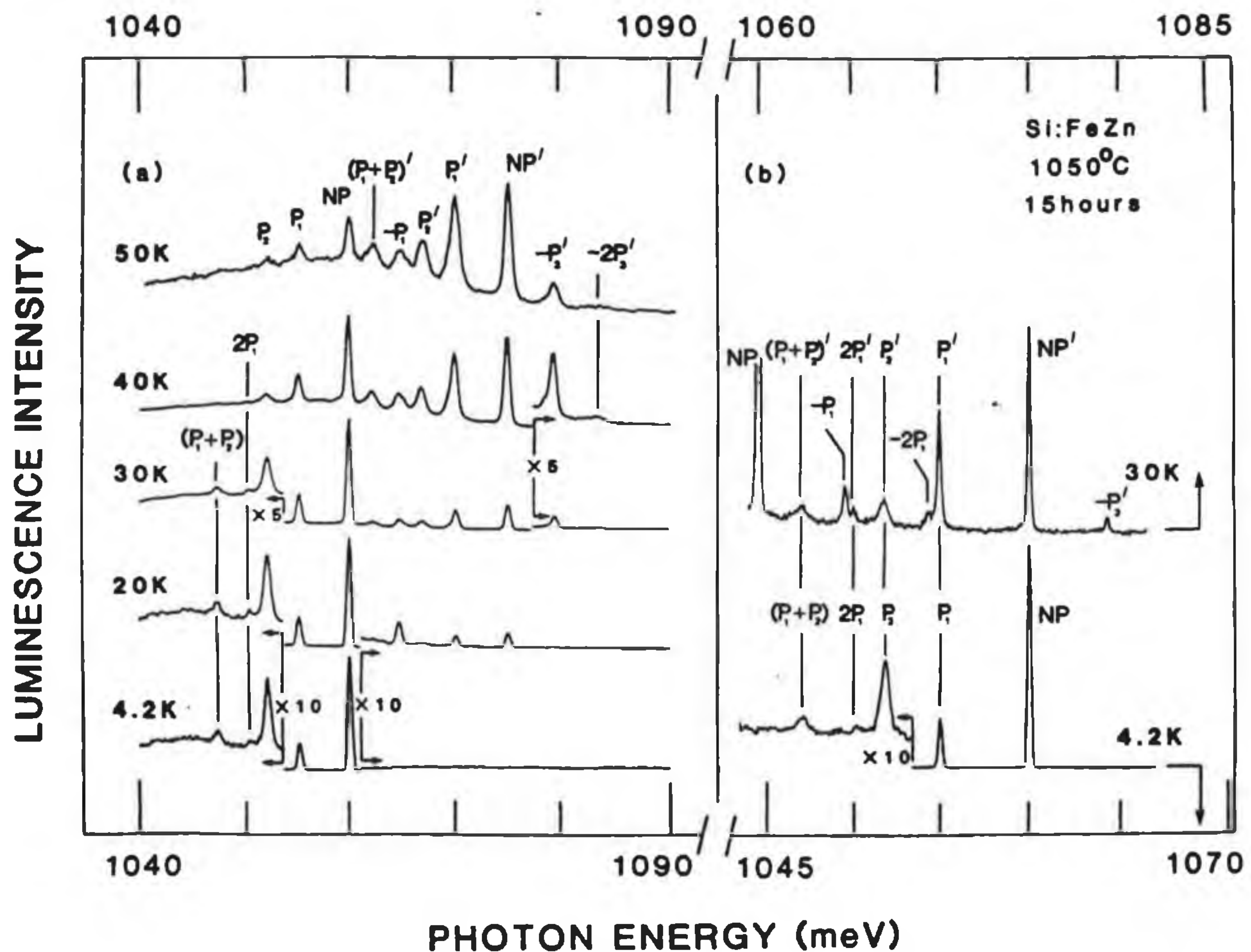

Fig. 5.13 (a) PL spectra for the temp. range 4.2 - 50 K

(b) 4.2 K and 30 K spectra displaced by 15.2 meV to align the NP & NP' lines.

A second system of lines emerges above NP as the temperature increases. Fig. 5.13 (b) shows the 4.2 K and 30 K spectra displaced by 15.2 meV such that the most intense line of the new system coincides with NP. It is immediately apparent that most of the new lines can be identified with P_1 and P_2 Stokes replicas of the line at 1075.12 ±.05 meV which is labeled NP' and identified as a ZPL originating on an excited state separated by 15.2 meV from the first excited state which gives rise to NP. This is confirmed by an Arrhenius plot of the NP':NP intensity ratio against

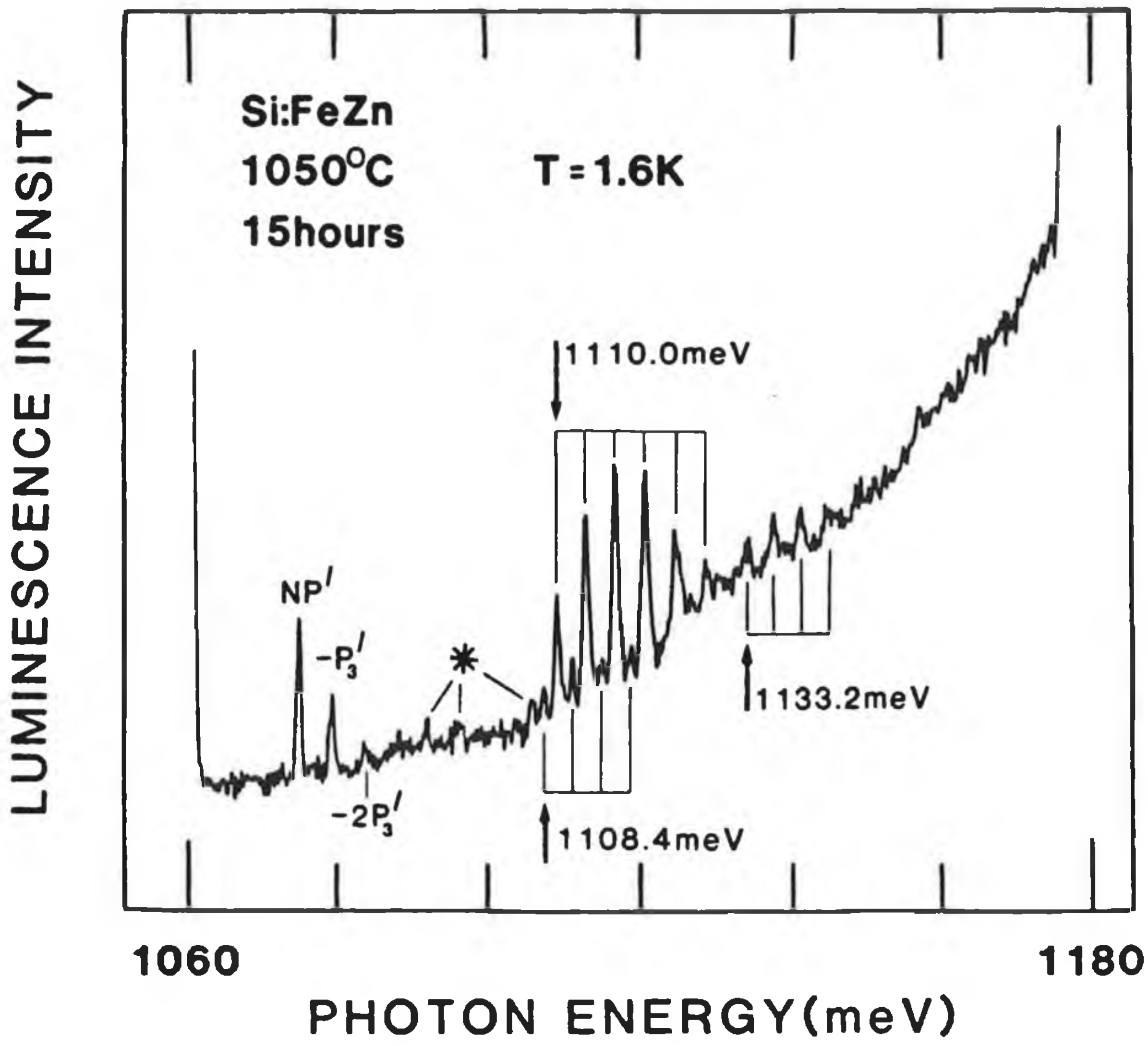

Fig. 5.14 A normalized PLE spectrum of the 1060 mev NP line at 1.6 K. Features marked with a * do not occur reproducibly.

temperature which yields a thermal activation energy of 14.7 ±1 meV which is in good agreement with the observed spectroscopic separation of the lines indicating that both lines are in thermal equilibrium and decay into the same ground state. This Arrhenius plot also gives us a value of infinite temperature ratio of approximately 50 thus explaining how the NP' line is observed, despite the large

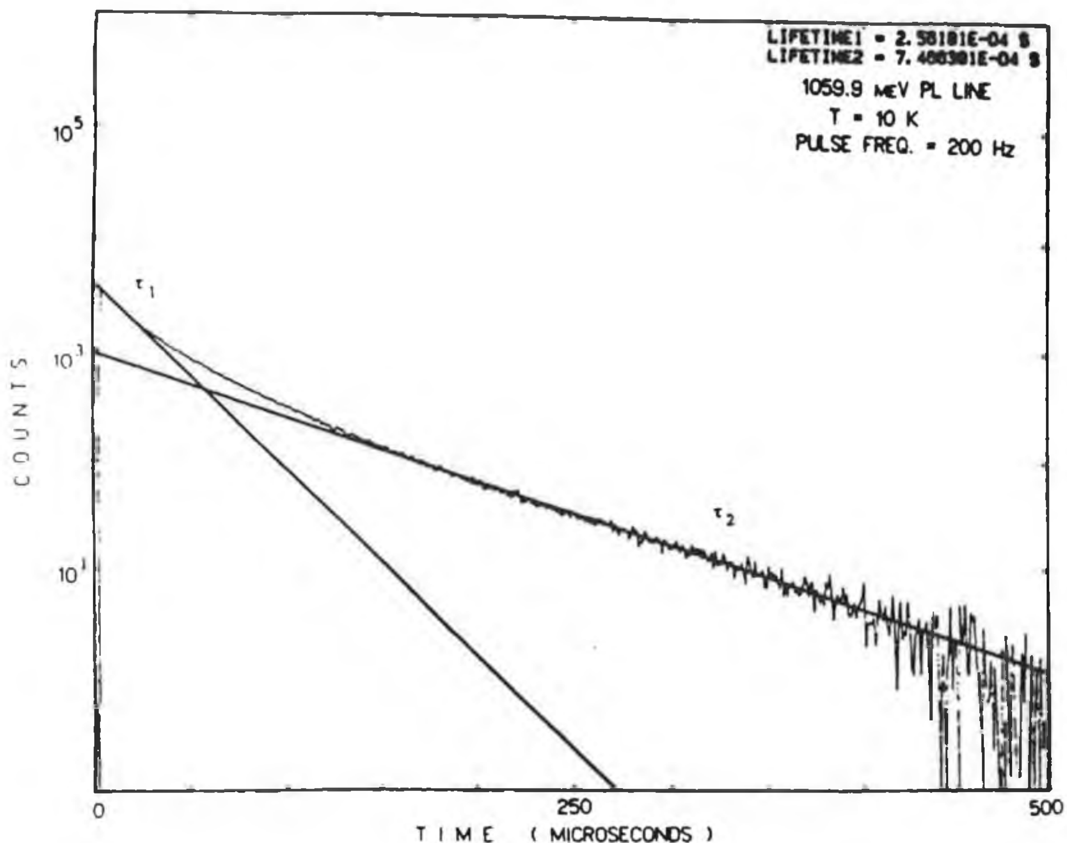

Fig. 5.15 10 K lifetime spectrum of the 1060 meV line.

activation energy, even at 20 K.

PLE and lifetime measurements were carried out on this system by M. O. Henry at Simon Fraser University, Vancouver. Fig. 5.14 shows the PLE spectrum of the 1060 meV NP line extending from the Si absorption edge down to the vicinity of the NP line. The NP' line is clearly seen at 1075 meV along with two 4.2 meV phonon replicas, consistent with the PL data. The NP line was not observed in the PLE spectra of its sidebands.

The dominant feature in the PLE spectra, however, is the series of sharp lines in the range 1108 - 1130 meV. This series can be subdivided into 2 sets of lines originating at 1108.4 meV and 1110.0 meV with separations of 3.5 meV between adjacent components within each set. This is interpreted as being consistent with absorption into a pair of electronic energy levels separated by 1.6 meV and both coupled to a 3.5

meV phonon mode. A third series of lines, also coupled to the 3.5 meV phonon mode is seen with its lowest energy component at 1133.2 meV.

The favourable spectral position of the PL band enabled lifetime measurements to be made at Simon Fraser University, Vancouver. Below 20 K the transients consist of 2 components whereas only single exponential decays are observed for T > 20 K. These two components are clearly visible in the 10 K transient shown in Fig. 5.15. This type of behaviour can be explained if we consider the situation shown in Fig. 5.16. Here we see two separate energy level systems within the band gap of the host crystal.

We assume that the system with the higher energy excited

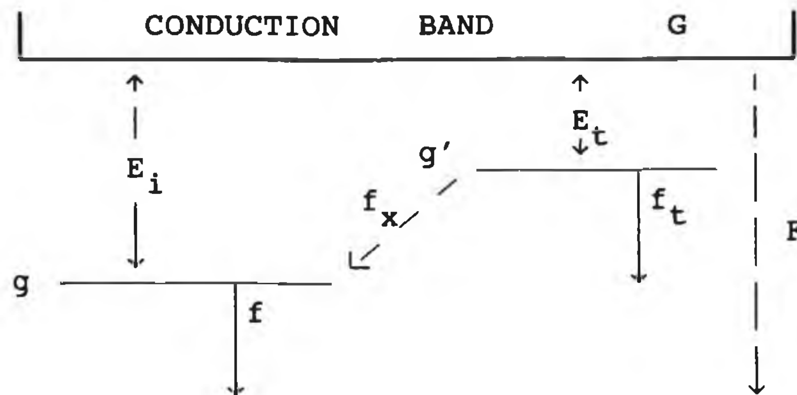

Fig. 5.16 Schematic representation of the effect of shallow traps transfering energy into a luminescence level.

state transfers some of its energy down to the lower energy system (which in our case would be the 1060 mev PL system).

Such a mechanism would give the luminescence a behaviour similar to that shown in Fig. 5.17. Here $I^1(t)$ is the luminescence of the 1060 meV band populated directly by the optical pumping pulse while $I^2(t)$ is the luminescence produced by energy transfer from the higher energy, longer lived traps (Reilly 1976).

If the slow exponential tail of the decay is extrapolated back to t = 0 (the dotted line in Fig. 5.17) and this value of luminescence intensity called B and the initial value of

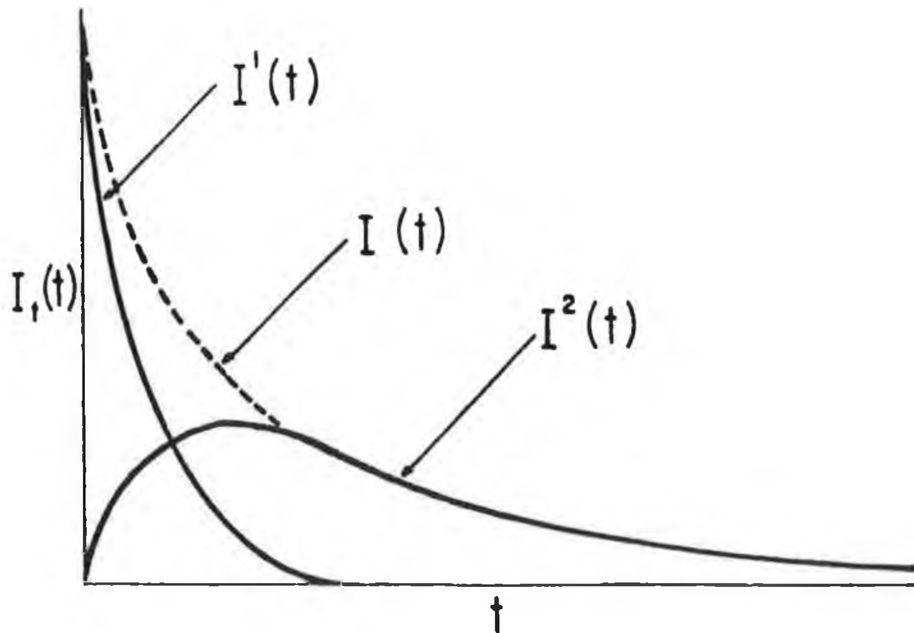

Fig. 5.17 Lifetime behaviour of a trap being partly excited via an energy transfer mechanism from another system.

the intrinsic trap luminescence called A, then the I(t) vs. t curve can be expressed in terms of these two constants as :

$$I(t) = A.\exp(-t/\tau\ ) + B.[\ \exp(-t/\tau_{\tau}) - \exp(-t/\tau\ )\ ] \qquad (5.2)$$

(Reilly 1976) where τ is the true decay of the luminescence and τ_{τ} is the decay lifetime of the contribution from the long lived traps as explained in section 2.10.

A plot of the luminescence decay time as a function of temperature is given in Fig. 5.18. The τ_t term of Eq. 5.2 was easily calculated from the tails of the lifetime transients are plotted as squares in the diagram. If a value of 240 μs is assumed for the τ term multiplied by the B factor in Eq. 5.2 and then the whole B component subtracted from the lifetime transients the remainders (plotted as crosses in Fig. 5.18) are found to be single exponentials. 240 μs is chosen since this is the measured lifetime at 20 K. This temperature is sufficiently low that the excited states make a negligible contribution to the lifetime. If a decreasing value of τ is assumed as the temperature increasesthe

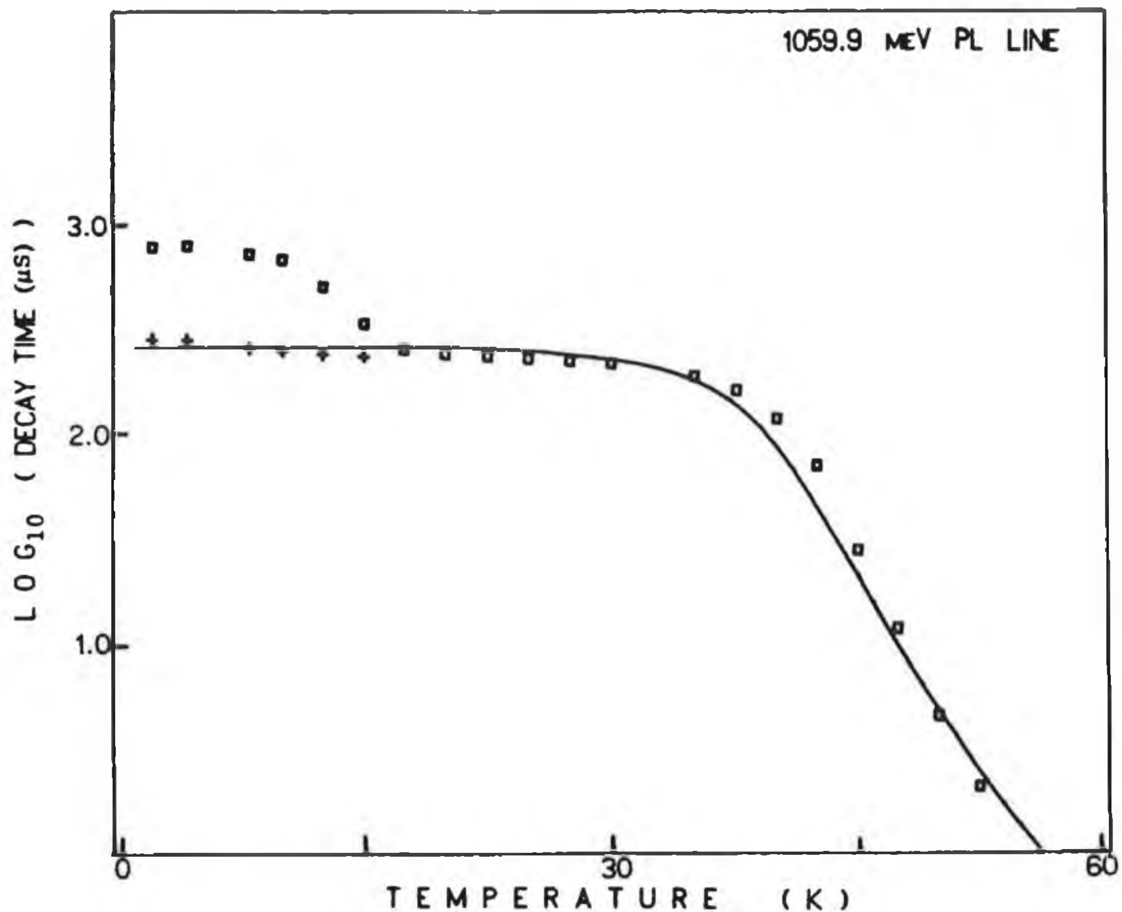

Fig. 5.18 A plot of the PL decay time versus temperature. Squares are measured values. The solid line and crosses show the values assumed & deduced for the PL decay time according to Eq 5.2 and Eq. 5.3 for T < 20 K.

agreement is even better. Such a decrease is quite likely given the enhancement of the sidebands in the PL spectra. In the range 35 - 40 K the lifetime decrease is consistent with the activation in to the 1075 meV level. Above 40 K a new and very efficient decay process takes effect. Allowing for the effect of the 1075 meV level, the new process is found to have an activation energy of 70 meV.

A theoretical plot of the true decay time of the luminescence with temperature is shown as the solid line in Fig. 5.18. The equation governing this line is :

$$1/\tau = \frac{g_0 f_0 + g_1 f_1 . \exp(-\Delta_1/kT) + g_2 f_2 . \exp(-\Delta_2/kT) + GFT^{3/2}\exp(-E_i/kT)}{g + g_1 \exp(-\Delta_1/kT) + g_2 \exp(-\Delta_2/kT) + GT^{3/2}\exp(-E_i/kT)} \quad (5.3)$$

where g_i = the degeneracy of the ith level.
f_i = the transition probability of the ith level.
Δ_1 = energy difference between the two lowest energy excited states.
Δ_2 = energy difference between the first and third excited states.
E_i = the ionization energy of the 1060 meV system defect.

and the subscript i = 0 refers to the lowest energy level.
i = 1 denotes the exchange split ground state level.
i = 2 denotes the valley-orbit excited state level.

the fitted parameters were first roughly guessed using evidence taken from PL, PLE and thermalisation data and then varied slightly to make the final fit whose values are listed in Table 5.3.

Δ_1	15 meV
Δ_2	48 meV
E_i	62.5 meV
$g_0 f_0$	1
$g_1 f_1$	50
$g_2 f_2$	250
GF	$1x10^8$

Table 5.3 Parameters fitted to equation 5.3 that create the solid line shown in Fig. 5.18.

One such short lived τ lifetime transient is shown in Fig. 5.19. As can be seen the calculated lifetime (the straight line in the figure) is valid over at least two orders of

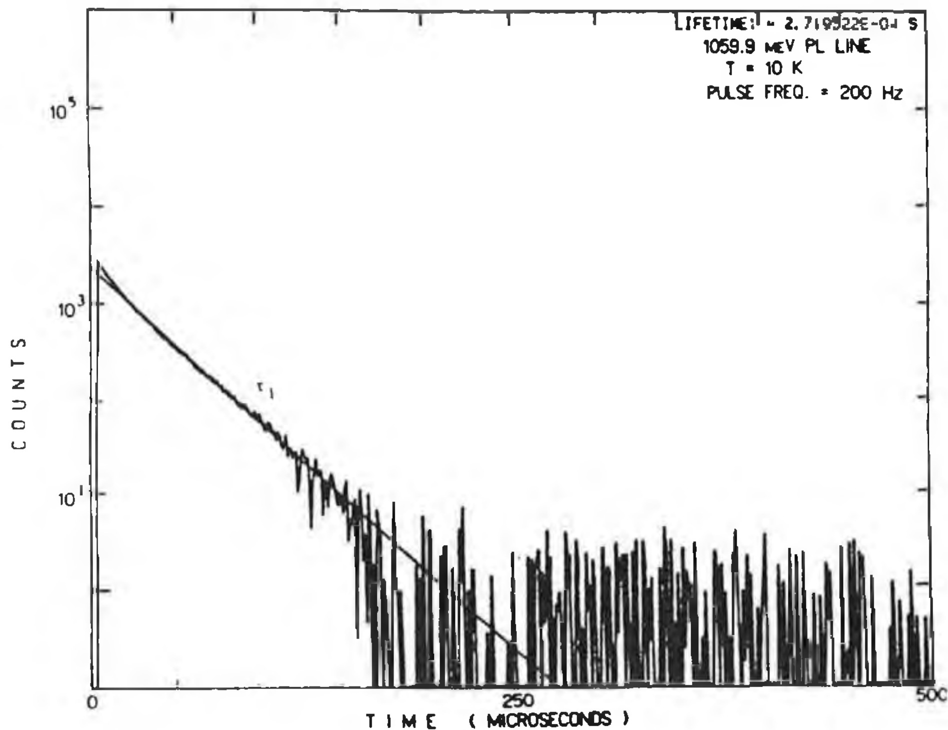

Fig. 5.19 Lifetime spectrum of the 1060 meV line with the energy transfer contribution subtracted out.

magnitude on the y-axis. This transient is in fact that produced by the transient shown in Fig. 5.15 and is within 10 % agreement with that calculated by Eq. 5.3.

The spectral position, the relatively long lifetime and the rapid decrease in PL intensity and lifetime for T > 40 K, all indicate radiative recombination at an IBE. The relative intensity of the NP & NP' lines conforms to that expected for forbidden and allowed transitions at an IBE although this necessitates an exchange splitting of 15.2 meV which is quite large for IBE's in Si. In this respect the 1060 meV system is similar to the Si:In IBE spectrum (Watkins et al. 1984) where the electron and hole are both localized at the optical centre and the overlapping wavefunctions produces a large exchange splitting of 11.4 meV (Watkins et al. 1986). Such a binding mechanism with a large exchange splitting could account for the 1060 and 1075 meV levels in this Zn - related

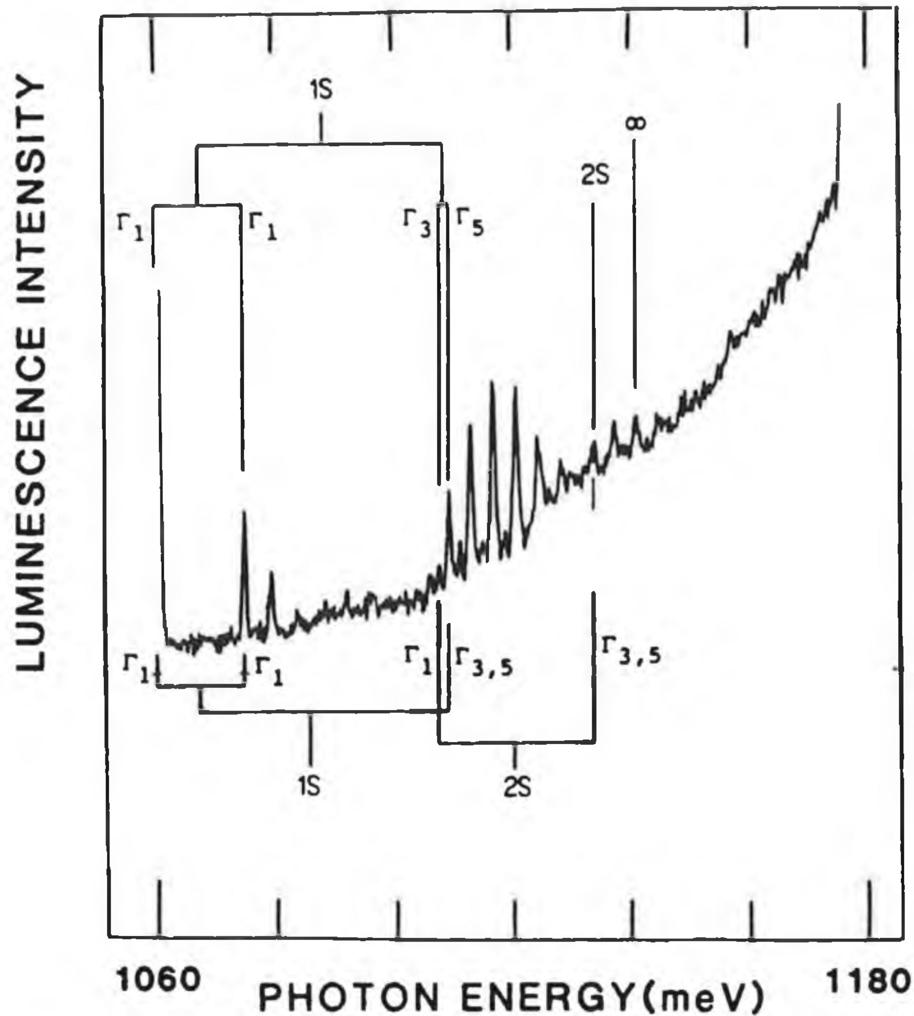

Fig. 5.20 PLE spectrum of the 1060 meV line with the theoretical energy level schemes included.

centre. Higher excited states observed in the Si:In PLE spectra have been identified as being Γ_3 and Γ_5 valley - orbit (V-O) excited states of the electron in the exciton.

Similar effects could also explain the presence of the excited states at 1110 meV in the Si:FeZn centre since the extra degeneracy of the V-O excited states account very well for the much greater intensity of the absorption into the 1110 meV levels compared to the 1075 meV level. The differences in the strength of the phonon coupling for the 1110 mev level compared to the 1060 meV and 1075 meV levels would also be expected due to the different electronic

configurations in the two cases. This identification of the 1110 meV level places the ionization limit of the IBE at 1141 meV, if the theoretical binding energy of 31.3 meV is assumed for the V-O excited states as calculated by Faulkner (1969) which is in reasonable agreement with the estimate of 1130 meV derived from the lifetime data.

The 1133 meV PLE level can be assigned to a 2s state of the electron. Again if a theoretical binding energy of 8.8 meV is assumed for this state (Faulkner 1969) the ionization limit is calculated to be 1142 meV in excellent agreement with the previously deduced value (Fig. 5.20). The fact that there are clearly 2 levels at 1110 meV can be accounted for in several ways. The two levels could result from two S = 0 states formed by the hole and non-degenerate V-O excited states (Γ_3 and Γ_5) of the electron or alternatively, degenerate Γ_3 and Γ_5 V-O states, could produce exchange split S = 1 and S = 0 states as explained schematically by the upper energy level scheme in Fig. 5.20. Neither can the possibility that the 1108.4 meV level corresponds to an S = 0 IBE state formed from a hole and a 2s electron in the Γ_1 V-O state be ruled out since the 2s state would be expected to show some V-O splitting in view of the large V-O splitting of 42.5 meV (in the absence of j-j coupling) for the 1s state (illustrated in the lower energy level scheme in Fig. 5.20).

On the question of chemical identity the PL spectrum was observed in samples doped with Zn and any of the following elements : Mn, Cu and Fe. The strongest signal levels were obtained from Si:Fe-Zn samples but all of these showed the presence of Cu impurities in the form of the 1014 mev Cu-Cu PL system. The 1060 meV system was also observed in samples nominally doped with Zn only but contaminated with Cu. Although there is strong evidence for the involvement of Fe or Cu along with Zn, the possibility that some other contaminant is participating cannot be discounted. For this reason a study of Zn ion implanted samples was undertaken but despite uncovering several previously unreported PL spectra (

which will be discussed later) no further information has as yet been obtained.

5.2.4 THE 1130 AND 1091 meV ZINC-IMPLANTED PL SYSTEMS

One of the main conclusions that can be drawn from the study of the three previous PL bands is that diffusion is not the most suitable method of introducing zinc into the silicon lattice since it is so susceptible to contamination. With this in mind a zinc implanted wafer was obtained with a view to studying the 919, 945 and 1060 meV systems in a much more controlled environment.

The starting material was a p-type CZ wafer with a boron concentration of 10^{14} cm^{-3} which was implanted with 70 keV ions. Samples cut from this were cleaned using organic solvents only (at no stage were acid etches used) and then subjected to 15 minute anneals in a helium atmosphere at a range of temperatures up to 1000° C.

None of the above mentioned PL bands were discovered in the implanted samples, further supporting the view that zinc alone is not responsible in their formation.

Following the implantation the PL spectra of the samples consist exclusively of the 969 meV carbon related system reported by Davies et al. (1983) and the 1018 meV W (or I1) system (Ciechanowska et al. (1984)), both of which are associated with radiation damage. The effects on the spectra of annealing at temperatures of 300° C and above are shown in Fig. 5.21. These bands persist on annealing up to 500° C after which they diminish in favour of three new groups of PL features. The first group consists of a broad featureless band centred about 885 meV accompanied by a series of sharp lines between 900 and 1000 meV. The energies of most of these lines correspond to features previously reported as being due to radiation damage (Mudryi et al. 1973, Tkachev et al. 1977, Davies et al. 1983, Ciechanowska et al. 1984 and Weman et al. 1985) and as such they will not be discussed here. The second group is identified by the strong line at 1090.68 ± 0.05 meV labelled Zn_B, which is the main line in the

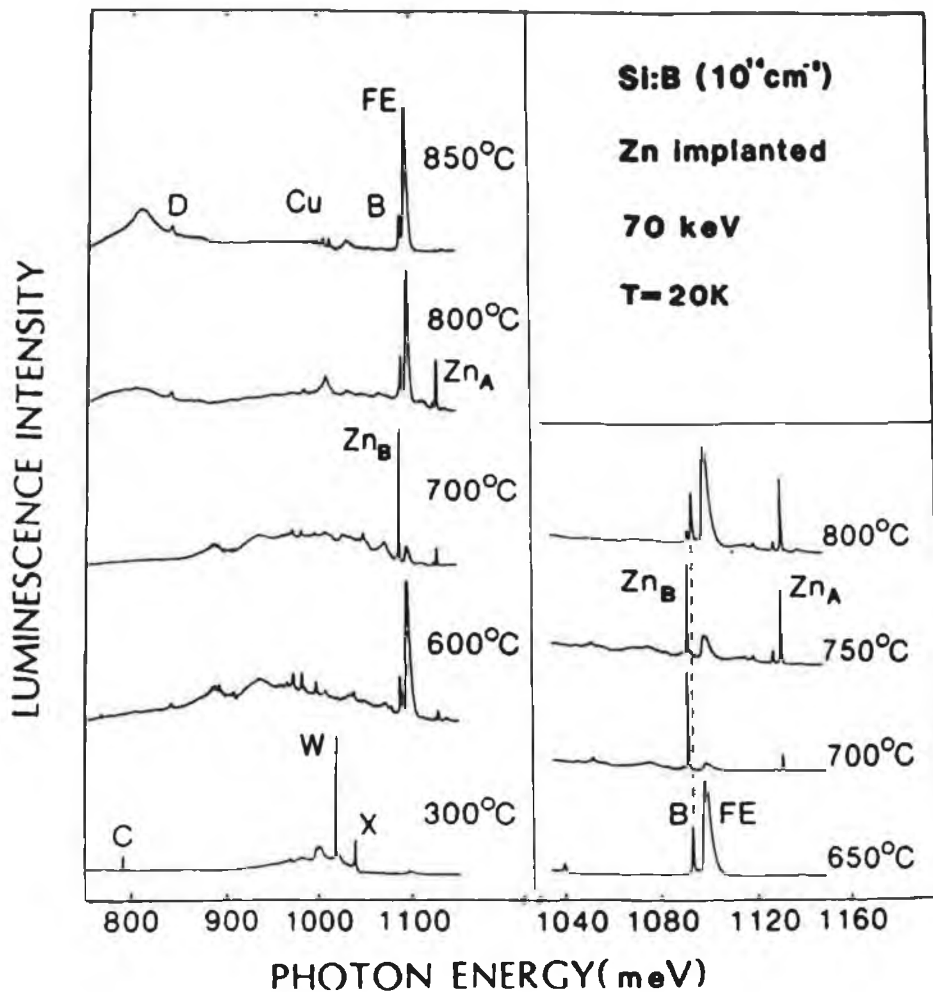

Fig. 5.21 PL spectra recorded for a Zn-implanted sample subjected to successive 15 minute anneals at the temperatures indicated.

spectrum of the sample annealed at 700°C. The third group of lines appear strongest in the spectrum of the 800° C annealed sample. The most intense feature in this group, labelled Zn_A, lies at 1129.82 ± 0.05 meV. Annealing above 800° C causes both the Zn_A and the Zn_B spectra to vanish. The spectrum then consists of a weak 1014 meV Cu-Cu (Weber 1982) system and the D lines associated with TM decorated dislocations (Lightowlers et al. 1989). Rapid quenching of samples annealed at 1000° C gives rise to the 1067 meV Fe-B PL band reported by Mohring et al. (1984). Fig. 5.22 shows high

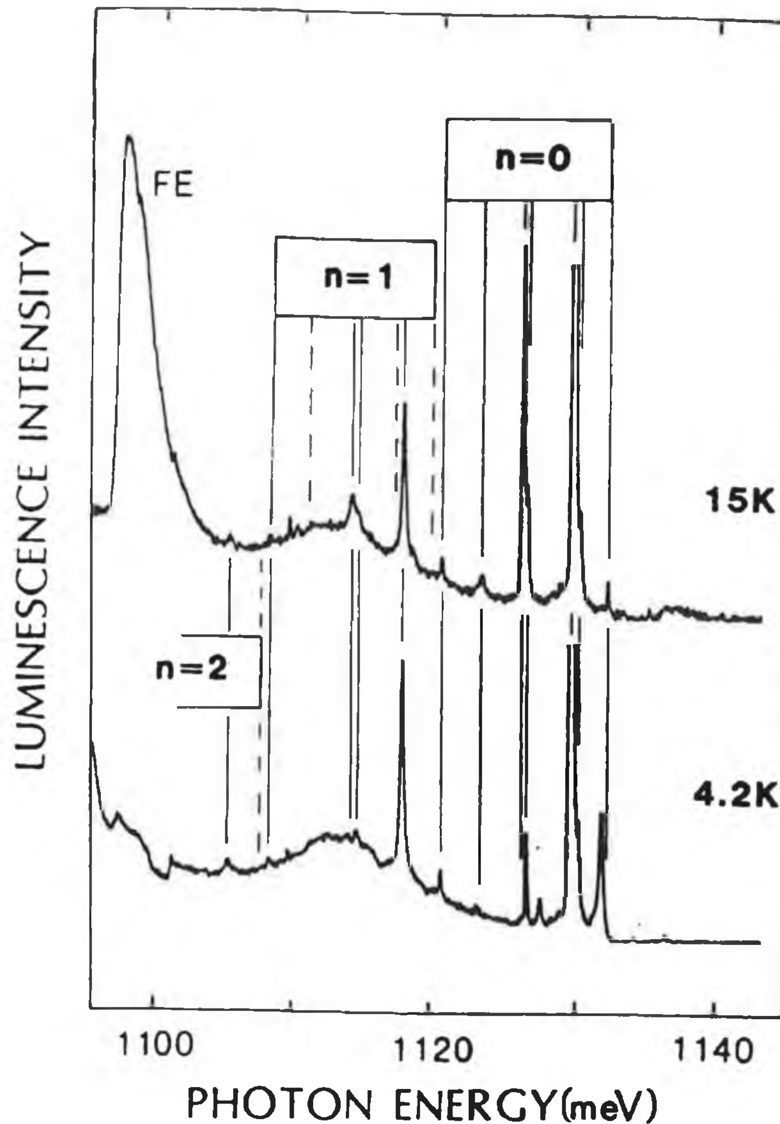

Fig 5.22 High resolution spectra of the Zn_A PL band recorded at 4.2 K and 15 K on a Fourier transform spectrometer.

resolution spectra of the Zn_A system recorded at 4.2 K and 15 K on a Fourier transform spectrometer, while the line energies of all the zero phonon features are given in Table 5.3. All the lines can be classified as zero phonon lines (n=0), one phonon replicas (n=1) or two phonon replicas (n=2) of a basic group of seven lines. In all the spectra recorded on different samples the relative intensities of the members of this group of lines are the same. This indicates that the lines are due to different transitions within the same centre. Careful study of the spectra reveals that the

ENERGY meV	LABEL
1132.42	Zn_A1
1130.38	Zn_A2
1129.85	Zn_A3
1126.88	Zn_A4
1126.65	Zn_A5
1123.50	Zn_A6
1120.68	Zn_A7

Table 5.4 A list of all the zero phonon line energies and labels for the Zn_A PL band.

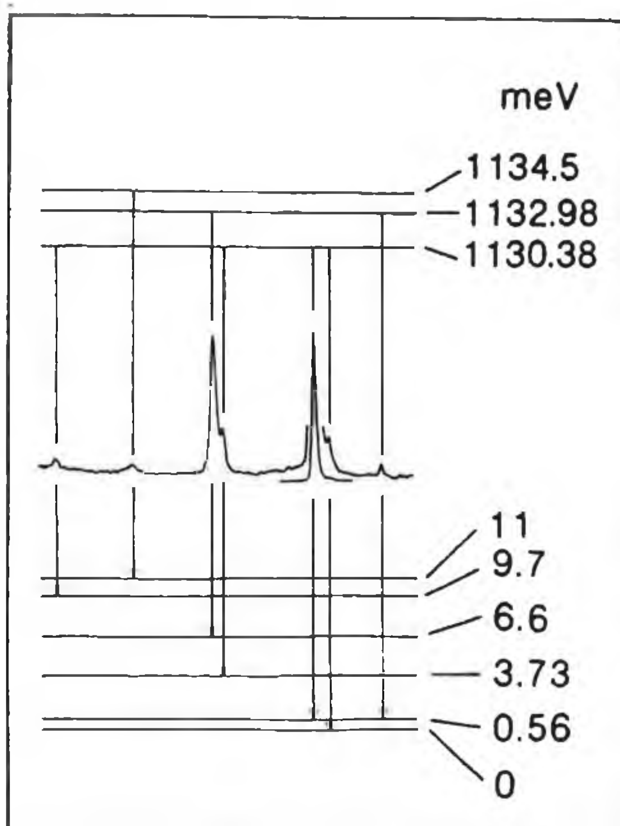

Fig. 5.23 The energy level diagram of the Zn_A PL system based on spectroscopic and thermalisation data.

strongest of the n=1 phonon replicas and the only observable n=2 replica are associated with the weak Zn_A2 line at 1130.38 ± 0.05 meV. Replicas are not observed for the intense Zn_A3 line . The energy level diagram shown in Fig. 5.23 is based on an analysis of the temperature dependence of the intensity ratios of this group of ZPL's.

The third group of lines lie in an area where several boron luminescence lines are also found but it is the features that persist above sample temperatures of 20 K that we label the Zn_B group as shown in Fig. 5.24. The closely spaced group of lines surrounding the intense feature at 1090.68 meV have

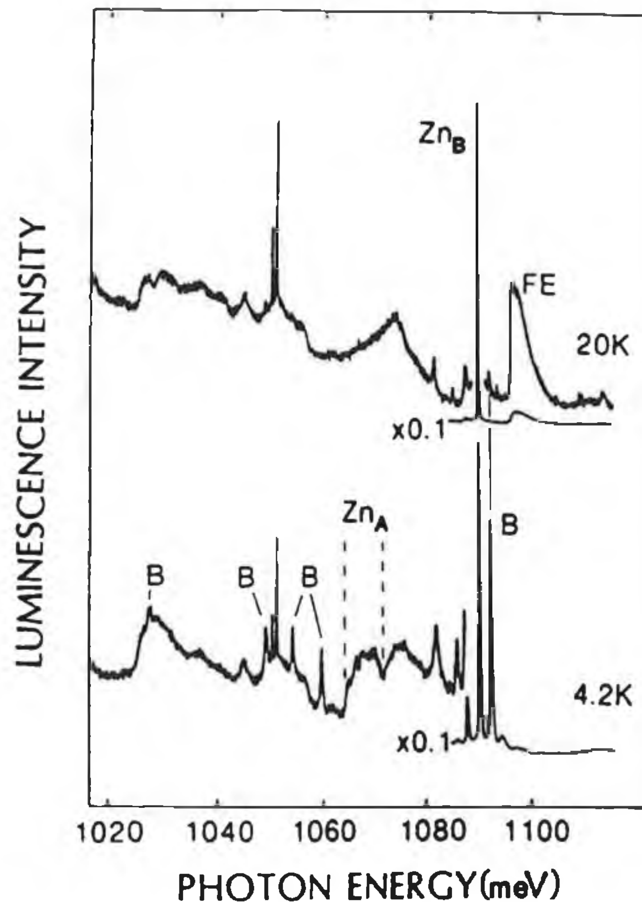

Fig. 5.24 High resolution PL spectra of the Zn_B system recorded at 4.2 K and 25 K on a Fourier transform spectrometer. Features marked B are associated with boron. The feaures marked by the dotted lines correspond to O^{Γ} cut-off points of Zn_A ZPL PL features.

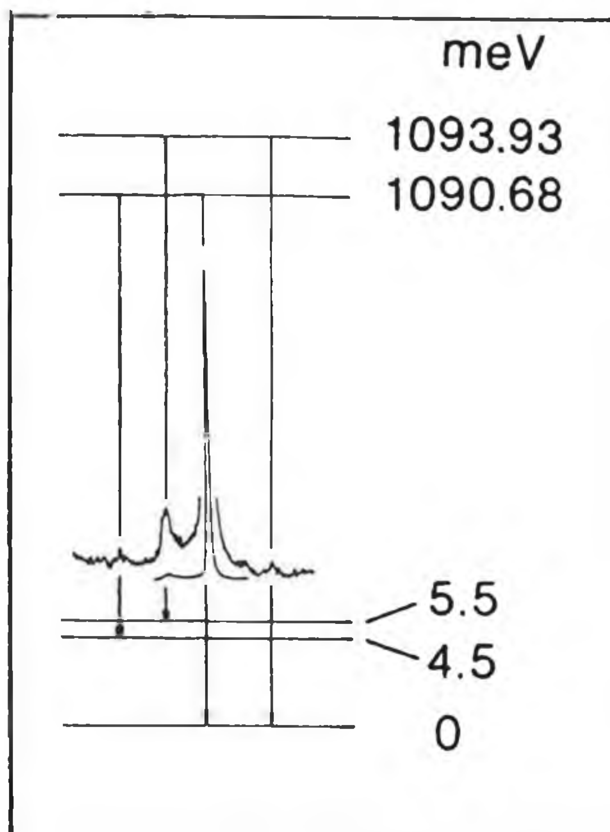

Fig. 5.25 Energy level diagram of the Zn_B PL system

been assigned to zero phonon lines and the energy level structure shown in Fig. 5.25 is based on the behaviour of the line intensities as a function of temperature. The zero phonon lines couple to several phonon modes, as is indicated by the richly structured phonon sideband. The two sharp features at around 1050 meV appear to be local mode phonon replicas separated by 39.4 and 40.4 ± 0.1 meV from the main line Zn_B2. A well defined broad peak at 1045 meV is separated from this line by 45.7 meV which corresponds to the peak in the LA phonon branch for silicon. The sharp cut-off in the phonon sideband occurs at ≅ 1026 meV , a separation of 64 meV which is also the energy of the O^{Γ} phonon in Si.

Fig. 5.26 (a) shows the temperature dependence of both PL spectra. The intensity of the Zn_A luminescence decreases rapidly above 20 K whereas the Zn_B system survives up to

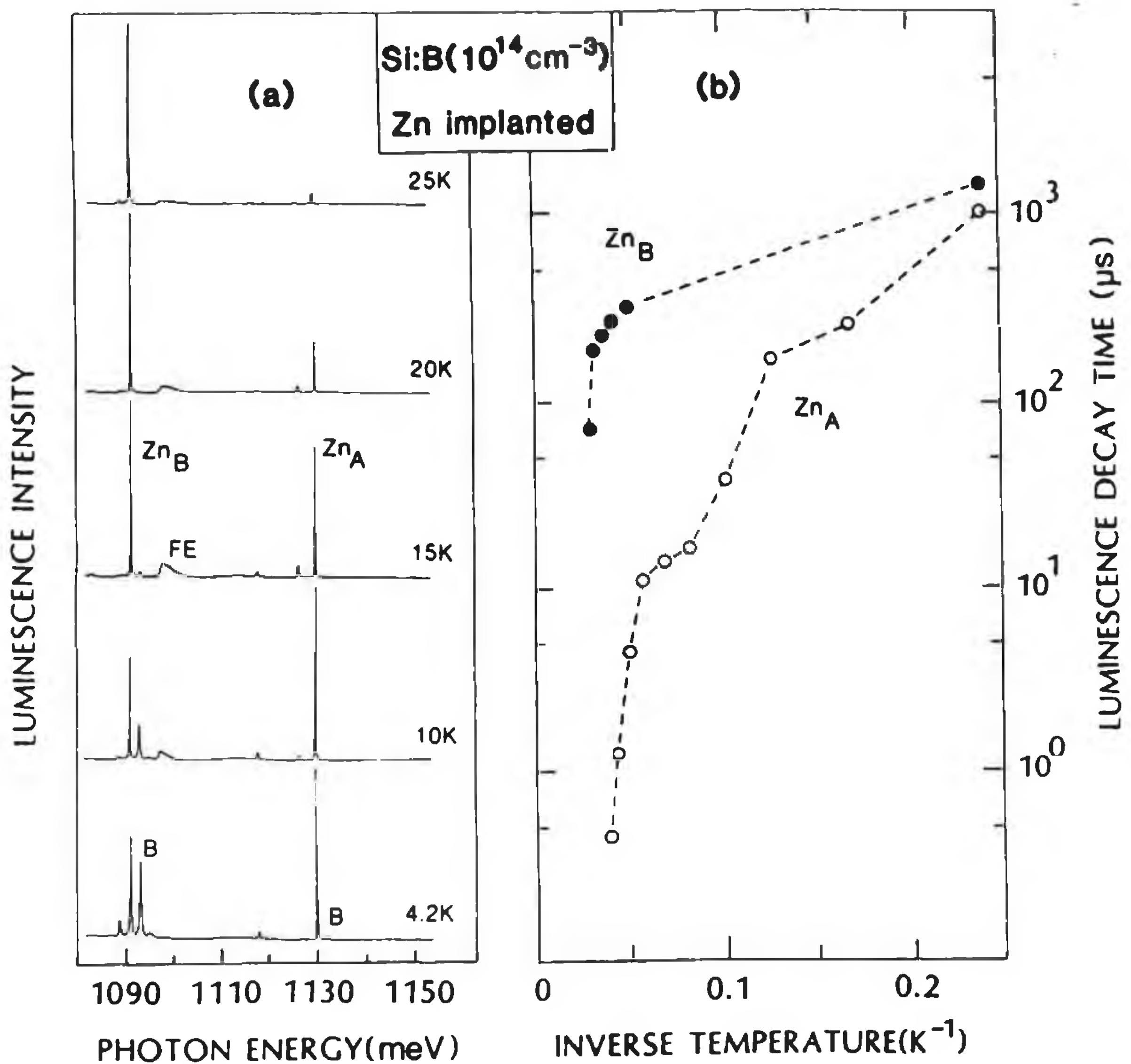

Fig. 5.26 (a) Temperature dependence of the PL spectrum of a sample that shows both the Zn_A and the Zn_B systems. For T > 40 K the luminescence is weak and confined to the 800-1020 meV range.

(b) Temperature dependence of the luminescence decay times of both systems. Broken lines are guides only.

temperatures of 40 K. Deactivation of the luminescence at such low temperatures is usually indicative of recombination of weakly bound carriers. Fig 5.26 (b) is a plot of the decay times of both systems as a function of inverse temperature. The data is consistent with the observed deactivation of the

luminescence intensity.

Both the Zn_A and Zn_B spectra are generally compatible with IBE recombination. In particular, the rapid fall off in the luminescence intensity and decay time with increasing temperature are characteristic of this type of recombination. The energy level diagrams as suggested by the thermalisation data place these systems in the minority group of IBE spectra with complex ground state structure exemplified by the Si:In and Si:Tl systems (Thewalt 1982). However, Zeeman measurements in fields up to 4 T in Faraday configuration failed to produce any shift or splitting in either system unlike the indium and thallium defects (Watkins and Thewalt 1985).

The high background boron concentration in these samples may be responsible for some of the observed luminescence and to this end further studies using higher purity starting material are desirable. In addition the sharp PL features are also well suited to isotope studies. Given that two other deep acceptors in silicon, In and Tl have also produced similar PL spectra it would appear that this class of impurity produces a distinct family of IBE spectra, which leads one to the conclusion that this area of research warrants further investigation.

5.3 COPPER RELATED PL STUDIES

5.3.1 THE 943.7 meV Cu-RELATED PL CENTRE

During investigations of the 1060 meV PL system it was noticed that samples that exhibited a weak 1014 meV Cu-Cu system (indicative of low Cu concentrations) often produced another similar PL system with ZPL features around 943 meV. This system was also reported by Minaev (1979) during his studies of heat treated Si. Early experiments indicated that the 943.7 meV system, which we labelled the Cu^* system, occurs only in samples with very low Cu doping levels. Accordingly a large number of samples were prepared using the

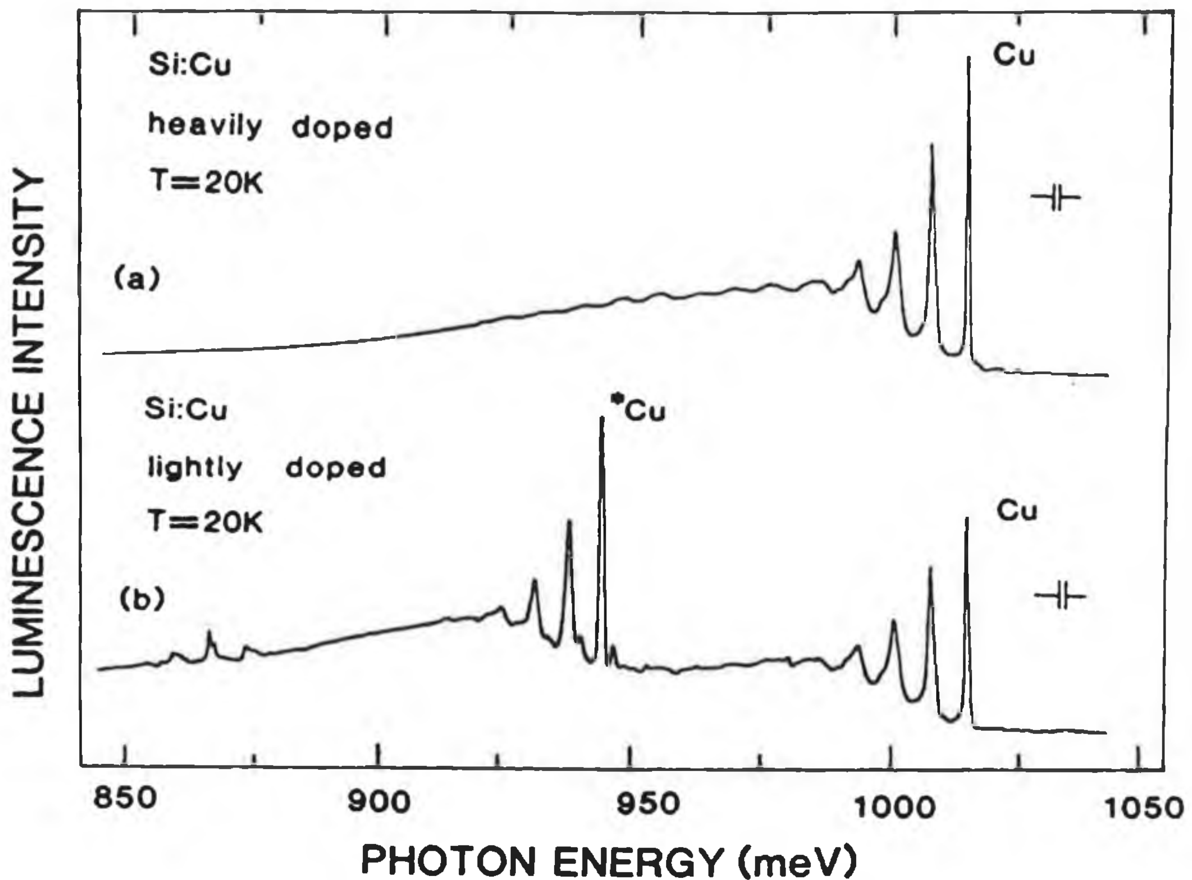

Fig. 5.27 PL spectra recorded at 20 K for Si samples (a) heavily doped and (b) lightly doped with Cu. Both spectra have been corrected for atmospheric water vapour absorption.

vertical furnace and fast quench method outlined in section 4.2.

If the PL spectra of heavily doped and lightly doped Si in Fig. 5.27 are compared the similarities between the Cu-Cu and Cu^* systems can be clearly seen. Another PL system of weak lines at ≅ 875 meV are seen. These lines were also reported by Minaev (1979). They are not thought to be intrinsic to the defect in question since they only appeared occasionally in Cu^* samples and so will not be discussed further in this section. Two high resolution PL spectra of the band are shown in Fig. 5.28 with the labels of each feature included.

Fig. 5.29 shows a range of high resolution Cu^* spectra recorded for a range of temperatures between 1.5 and 58 K.

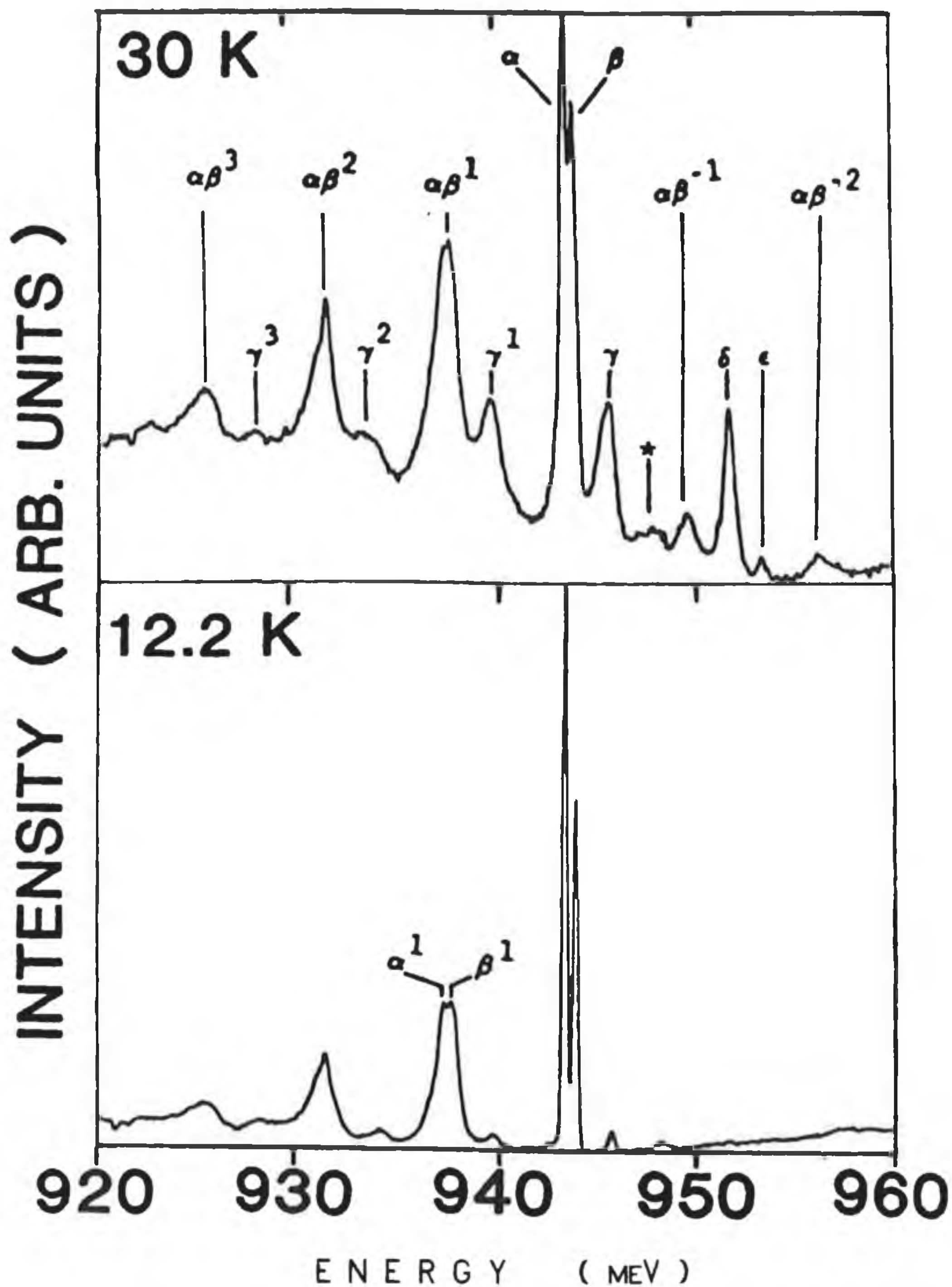

Fig. 5.28 High resolution spectra of the Cu* PL band at 12.2 and 30 K.

The spectrum consists of 5 ZPL's that were labelled Cu^{*0}_{0} to Cu^{*0}_{4} by McGuigan et al. (1988) - but for convenience have

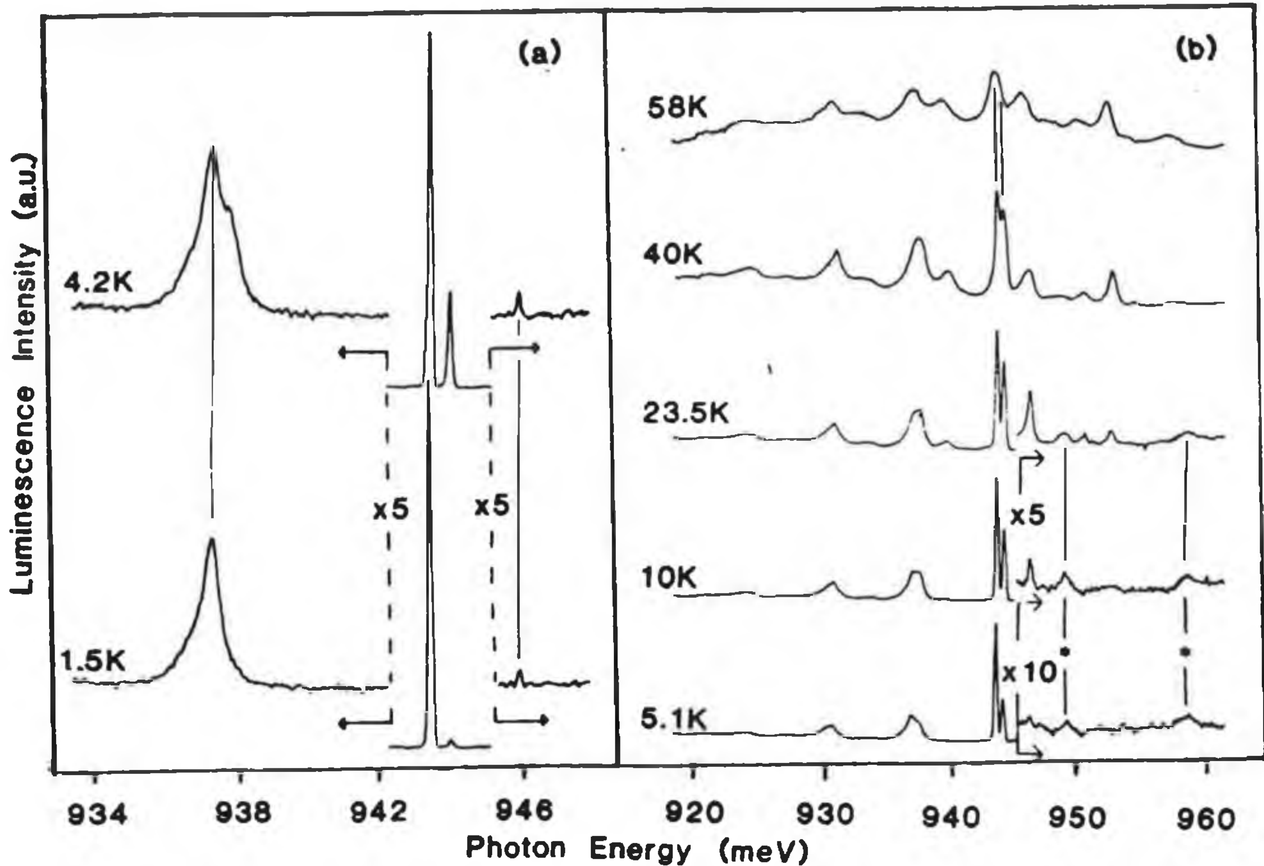

Fig. 5.29 (a) PL spectra in the region of the ZPL's & first Stokes replica at 1.5 K & 4.2 K recorded on a Fourier - Transform spectrometer at King's College London.

(b) PL spectra in the temperature range 5.1 K to 58 K, recorded on a dispersive spectrometer at N.I.H.E.

been relabelled α, β, γ, δ and ε throughout the remainder of this text. A number of Stokes and anti-Stokes phonon replicas, involving a phonon of 6.45 meV energy, can be seen coupling to most of the transitions, as well as a moderately strong broad phonon side band. The positions of all the features both their labelling systems and their spectroscopic separations from their corresponding ZPL's are given in Table 5.5. The γ line has an asymmetric lineshape that can be partly explained by a contribution from a Stokes replica of

ENERGY (meV)	LABEL 1	LABEL 2	SEPARATION SPECTRAL (meV)	SEPARATION THERMAL (meV)	T(∞) RATIO	NOTES
943.67	Cu^{*0}_{0}	α	-	-	1	ZERO PHONON LINES
944.24	Cu^{*0}_{1}	β	0.57	0.5	1	
946.24	Cu^{*0}_{2}	γ	2.57	?	?	
952.56	Cu^{*0}_{3}	δ	8.89	11	10	
954.20	Cu^{*0}_{4}	ε	10.50	12	2.5	
937.22	Cu^{*1}_{0}	α^1	6.45			STOKES SIDEBANDS
930.78	Cu^{*2}_{0}	α^2	12.89			
924.20	Cu^{*3}_{0}	α^3	19.4			
937.79	Cu^{*1}_{1}	β^1	5.88			
931.50	Cu^{*2}_{1}	β^2	12.2			
939.60	Cu^{*1}_{2}	γ^1	4.1			
933.50	Cu^{*2}_{2}	γ^2	10.2			
950.40	$Cu^{*-1}_{0,1}$	$\alpha\beta^{-1}$	6.4*			ANTI-STOKES SIDEBANDS
957.30	$Cu^{*-2}_{0,1}$	$\alpha\beta^{-2}$	13.3*			

* measured from the mean energy of α & β

Table 5.5 A compilation of all the PL features observed in the Cu^* spectrum. The spectroscopic separations of all lines are included as well as the thermal activation energies and infinite temperature ratios for all ZPL's

the δ line. The lines marked * in Fig.'s 5.28 and 5.29 are associated with the underlying Cu-Cu spectrum.

Temperature dependent measurements showing the log of the intensity of each ZPL relative to that of the α line versus inverse temperature are displayed in Fig. 5.30. Their relative infinite temperature ratios and thermal activation energies are calculated from these data. With the notable

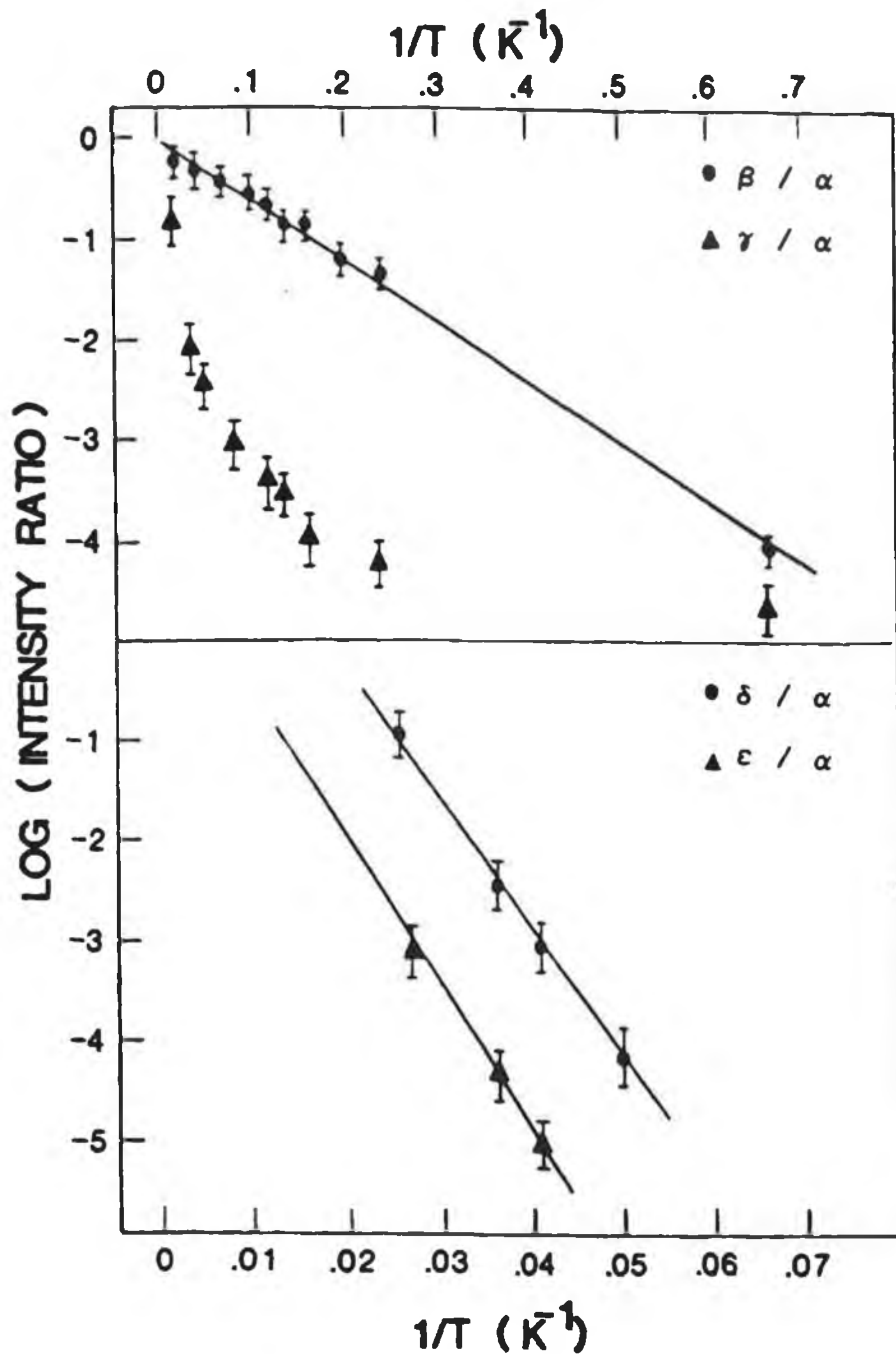

Fig. 5.30 The $\log_e$ of the intensity ratio of all zero phonon lines relative to line A plotted against inverse temperature. The solid lines are least-square fits to the data using equation 5.1.

exception of line γ all the thermal activation energies are in reasonable agreement with their respective measured, spectroscopic separations, indicating that these lines all

share a common ground state.

Line γ is observed at all temperatures down to 1.5 K and as can be seen from Fig. 5.30 its intensity relative to the α line does not follow a simple exponential relationship with temperature. This behaviour can be explained perhaps if this level has a slow thermal relaxation down to the other excited states within the energy level manifold, which results in radiative transitions occurring before the level can completely relax. Such a mechanism has been reported for the Si:In IBE and the Si:P BE by Thewalt (1982 and 1979).

The straight line fits in Fig. 5.30 assume that the relative intensities of any two spectral lines, originating from levels in thermal equilibrium, can be expressed by :

$$\frac{I_1}{I_0}(T) = \frac{g_1 f_1}{g_o f_o}.\exp(-\Delta E/kT) \quad (5.3)$$

: where g_i is the degeneracy of level i
f_i is the transition probability of level i.

This equation is valid for zero phonon lines, neglecting the role of phonon sideband effects if, and only if, their respective Huang-Rhys factors are equal. In reality each line intensity has a temperature dependence given by :

$$I(T) = I(0).\exp[-S(2n+1)] \quad (5.4)$$

: where S is the Huang-Rhys factor and n is given by :

$$n = \exp[(\hbar\omega/kT)-1]^{-1} \quad (5.5)$$

: $\hbar\omega$ being the energy of the phonons involved. Eq. 5.4 thus becomes

$$\frac{I_1}{I_o}(T) = \frac{g_1 f_1}{g_o f_o}.\exp(-\Delta E/kT).\exp[-(S_1-S_o)(2n+1)] \quad (5.6)$$

The S_i can be calculated from the intensity ratio of the

first phonon sideband relative to the ZPL intensity. For $\hbar\omega$ = 6.4 meV, S_{α} = 0.5 and S_{β} = 0.7. The measured β/α intensity

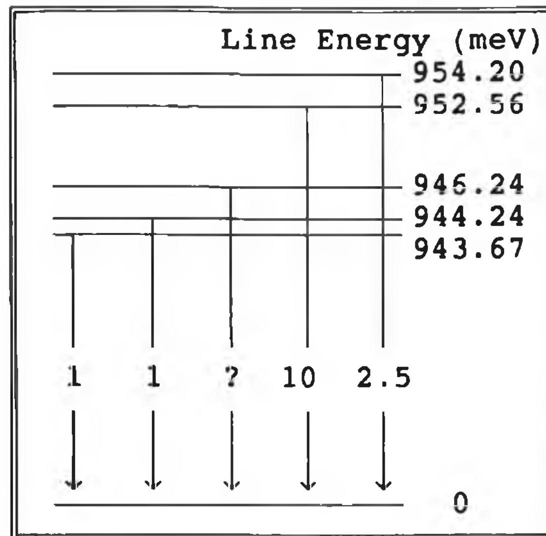

Fig. 5.31 Diagram of the energy levels for the Cu^* centre. The numbers on the vertical lines are infinite temp. intensity ratios.

ratio underestimates the corrected value by 12% at 50 K. Close inspection of Fig 5.30 shows that the measured values of the β/α intensity ratio deviate away from the straight line dependence at higher temperatures. This explains why the thermal activation energies calculated from straight line fits to this graph are somewhat lower than expected. A simplified energy level diagram based on the evidence obtained from the thermalisation data is given in Fig. 5.31.

The Cu^* PL spectrum bears a striking similarity to the 1014 meV Cu-Cu PL system. Copper in GaP and InP has been shown to produce a variety of almost identical PL spectra (Gislason et al. 1982 and Skolnik et al. 1984), while Li, another fast diffuser in Si also produces a range of similar PL systems in electron - irradiated Si (Canham 1984). This behaviour may be characteristic of fast diffusers in general.

A plot of the total intensity versus temperature is given in Fig. 5.32. The Cu^* PL band is not well behaved with respect to temperature dependence of the total intensity. One

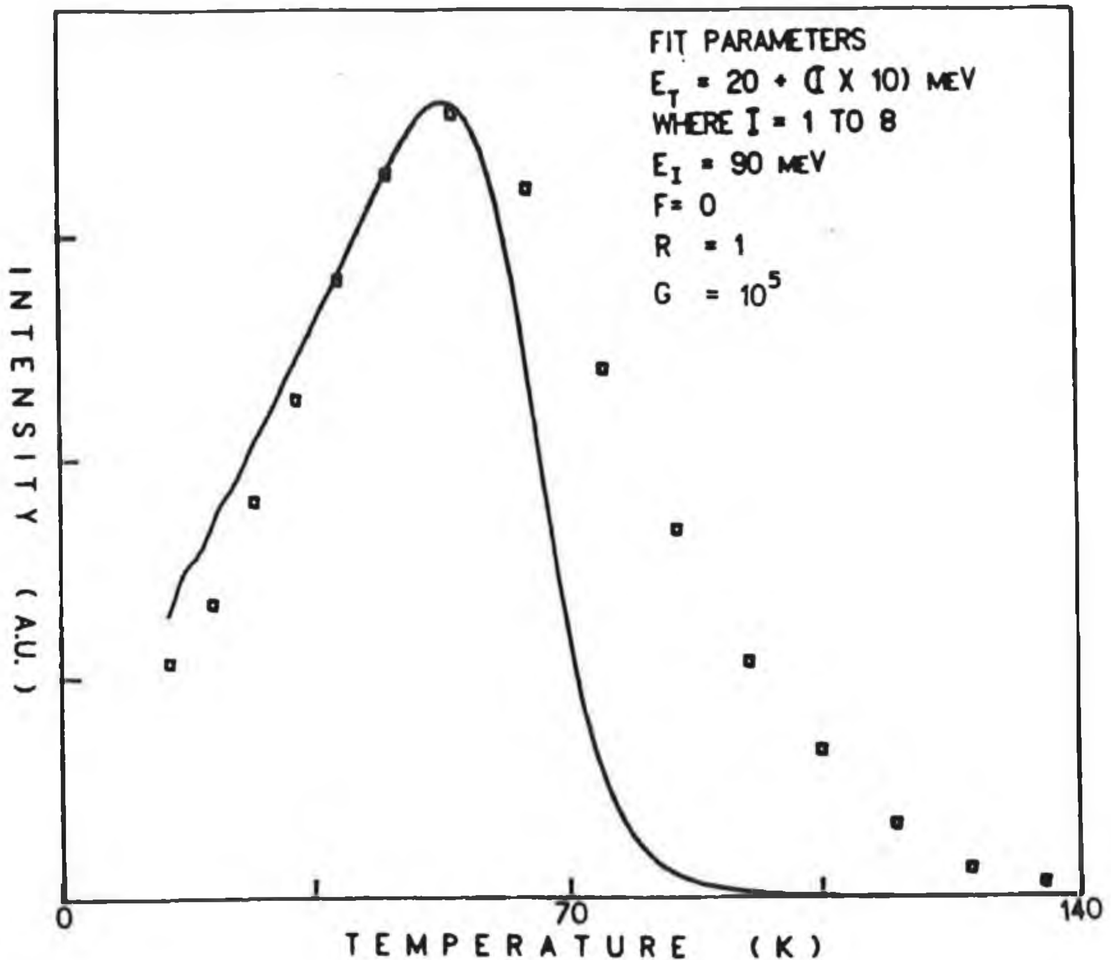

Fig 5.32 A plot of the total intensity of the Cu* PL system versus the sample temperature.

would expect the intensity to obey a relation similar to Eq. 2.18 but no suitable fit could be made to the data. A barely acceptable fit to the low temperature side of the curve (solid line in Fig. 5.32) can be made assuming a range of different shallow traps start transferring energy into the level at different activation energies but no explanation could be found for the slow decay of luminescence as the excitons begin to ionize off the levels. Clearly some kind of feeding process into the state must be in operation at these temperatures. This effect might be connected to the irregular temperature behaviour of the γ line intensity since above 40 K this feature is one of the more dominant lines in the spectrum.

Since the Cu-Cu spectrum has been identified with IBE recombination at a copper centre involving at least two copper atoms, the possibility that the Cu^{*} system might be a precursor to the Cu-Cu system was considered. Annealing studies have shown that the Cu^{*} system anneals out after approximately 1 hour at 275° C without any corresponding increase in the intensity of the Cu-Cu system, leaving us with no evidence, as yet, to connect the two PL systems apart from the involvement of copper. Samples produced from FZ or CZ starting material showed no reproducible differences in the Cu^{*}/Cu-Cu intensity ratio, thus ruling out the possibility that the Cu^{*} defect is a carbon modified Cu-Cu defect such as occurs in Si:Be (Labrie 1987) and Si:Li (Lightowlers 1984). Although there is little doubt that copper impurities are involved in the Cu^{*} defect it is difficult to discount the involvement of other elements, given that other impurity elements are inevitably present in the samples considering the treatment which they undergo.

Further discussions on the defect identity based on the results of uniaxial stress and Zeeman measurement are given in the next chapter.

5.3.2 THE 1034 meV COPPER RELATED SYSTEM

As mentioned before, the final PL spectra obtained from copper diffused silicon was mostly determined by the quench rate that the sample experienced. Nowhere was this more apparent than for the case of the ingot of copper contaminated silicon (concentration = 10^{13} cm^{-3}) received from Wacker. Samples of dimensions 9 x 4 x 2 mm would produce a different spectrum than those of dimensions 7 x 3 x 1.5 mm simply because the larger mass/surface-area ratio prevented the bigger samples from quenching as fast as the smaller ones. Under the same conditions, smaller samples produced strong Cu^{*} signals while larger produced the PL spectra shown in Fig. 5.33 (b). The spectrum is dominated by the 1014 meV Cu-Cu PL band (Weber et al. 1982) but two sharp features can be seen on the high energy side of the system. These

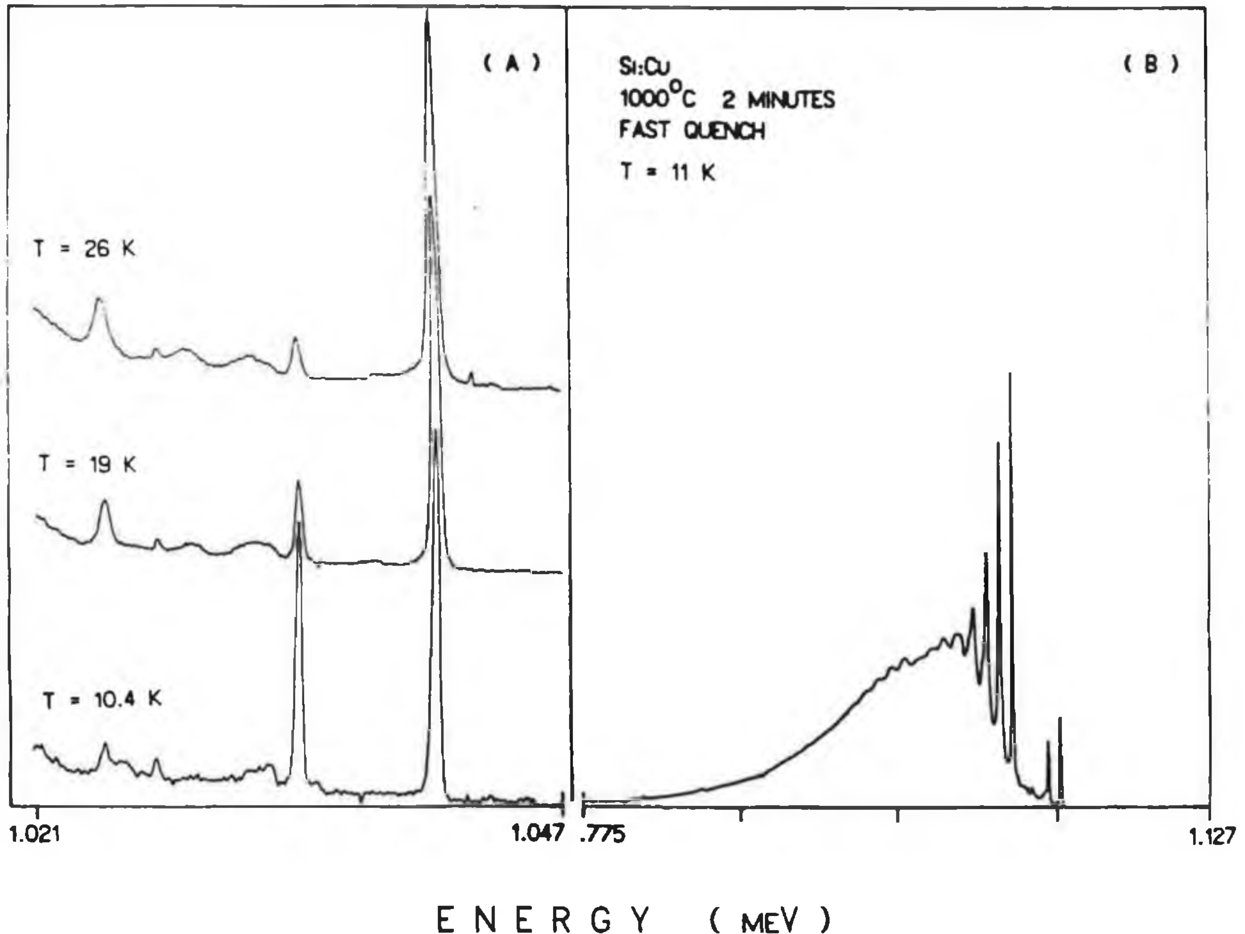

Fig. 5.33 High (A) and low (B) resolution PL spectra of the 1033.5 meV and 1014 meV systems produced in Si:Cu samples after heating at 1000°C for two minutes followed by a fast quench.

lines are shown in greater detail in Fig. 5.33 (a). This spectrum was recorded at D.C.U using the Spex 1m dispersive spectrometer. The system appears at first sight to consist of these two lines at energies 1034.01 ± 0.02 meV and 1040.11 ± 0.02 meV. However, subsequent studies carried out using a Fourier transform spectrometer at Kings College London reveal that each line is in fact a doublet, both having a separation of 0.1 ± 0.02 meV (Fig. 5.34). The reason that this

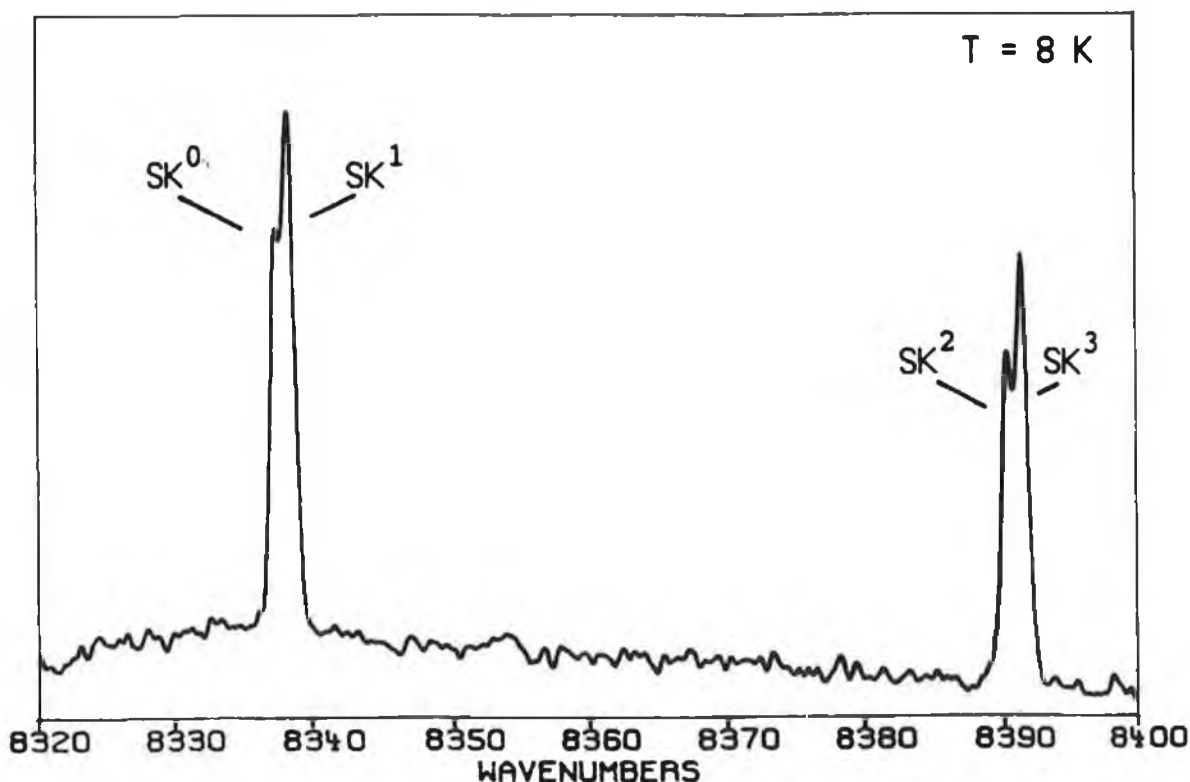

Fig. 5.34 High resolution spectrum of the 1034 meV system recorded on a F.T.I.R. spectrometer at K. C. L. (Note, energy (meV) = wavenumber X 0.123948)

splitting was overlooked in the first dispersive scans is a combination of the facts that the spectrum was taken at 200 microns slitwidths and a scanning increment of 1 angstrom, equivalent to 0.1 meV in this region of the spectrum, was used. Table 5.6 gives the line energies and labelling of all the features in the system.

At low temperatures the $SK^{0,1}$ doublet predominates but the intensity of the $SK^{2,3}$ doublet grows rapidly as temperature increases. An Arrhenius plot of the log of the ratio of the integrated intensities with inverse temperature yields a thermal activation energy of 4.2 ± 1.0 meV which is reasonable agreement with the spectral separation (6.54 ± 0.02 meV) suggesting that both levels decay into the same ground state manifold. The infinite temperature ratio for

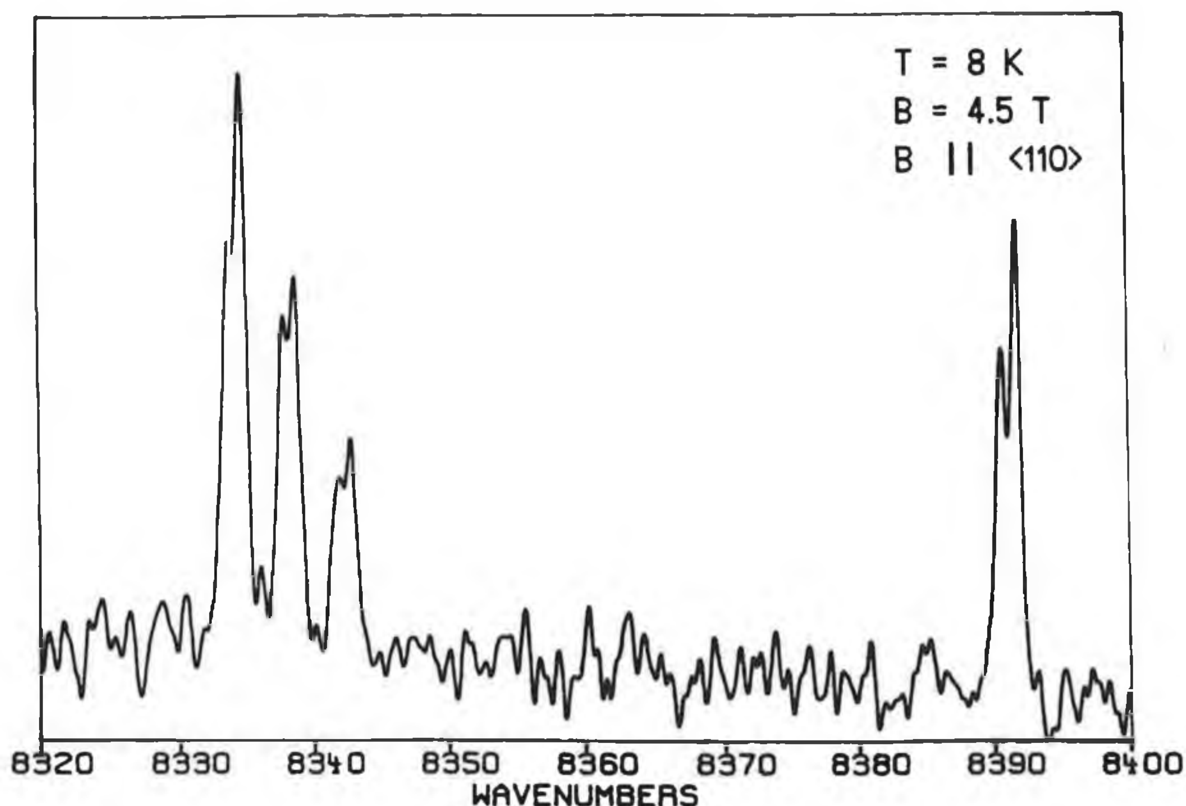

Fig. 5.35 Representative Zeeman spectrum of the SK PL band.

these doublets is calculated from the same data and is found to be approximately $SK^{2,3}$: $SK^{0,1}$ ≅ 76 : 1 .

The results of Zeeman measurements in Faraday configuration in fields up to 5.5 T are shown in Fig's. 5.35 and 5.36. The $SK^{0,1}$ feature is seen to split into an isotropic thermalizing triplet with each of its components retaining its original doublet fine-structure. The thermalisation between the components indicates that the splitting is in the excited state and not the ground state. The $SK^{2,3}$ doublet remains unaffected by the magnetic field. This triplet - singlet nature is usually indicative of a strong hole-attractive, compressive axial field about the defect site (Gislason et al. 1985).

Close examination of the splitting in any of the K.C.L. spectra suggests that the splitting in the lower energy doublet is smaller than that in the higher energy pair.

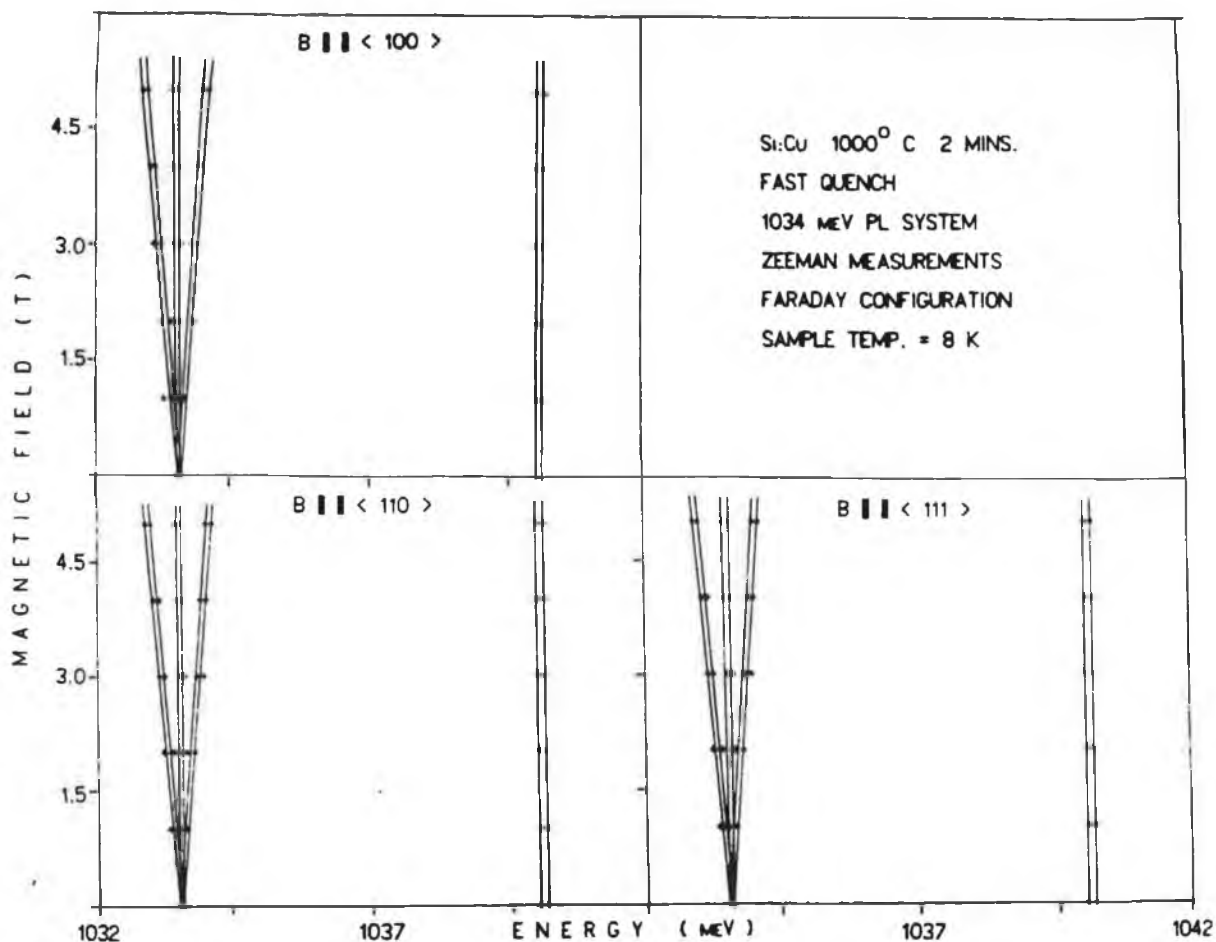

Fig. 5.36 Fan diagrams showing the Zeeman splittings of the SK ZPL's for the three major crystalographic directions.

ENERGY (meV)	LABEL
1033.51	SK^0
1033.62	SK^1
1040.05	SK^2
1040.17	SK^3

Table 5.6 Line energies and labelling of the 1034 meV system.

However, given the signal to noise ratios involved in the Zeeman spectra and the fact that in each case the doublet

separation is less than the full width at half maximum of the PL feature no further statement can be made based on the data at hand.

With regard to the chemical identity of the defect constituent(s), there is little that we can say with any degree of certainty except perhaps that it is likely that copper is involved. Clearly further diffusion, annealing, and isotope studies would go a long way towards giving us a better understanding of this defect and the PL band associated with it.

CHAPTER 6 : UNIAXIAL STRESS AND ZEEMAN MEASUREMENTS ON THE 943.6 meV Cu^* PL SYSTEM IN SILICON

6.1 INTRODUCTION

It was decided to perform uniaxial stress and Zeeman measurements on at least one of the newly discovered PL bands in the hope that the symmetry and exciton states of the defect could be determined. The decision to study the Cu^* system was made for both scientific and financial reasons. Sets of samples oriented along the main crystal directions are quite expensive so we had to be as certain as possible that the risk of contamination during the diffusion process was minimised. In addition to this it would be wasteful to use a set of oriented samples on a system of little scientific interest. With these factors in mind the Cu^* system was chosen because it was the defect most easily reproduced in the laboratory, while also being one of the least well understood of the newly detected systems. Also the Cu^* centre appears to be one of the simpler copper centres since it is only seen in lightly doped samples.

6.2.1 UNIAXIAL STRESS MEASUREMENTS

The usual dimensions of oriented samples (9 x 4 x 2 mm) are much larger than those of the unoriented Cu^* samples (usually ≅ 2 x 2 x 1 mm) that had been studied prior to this. In an effort to ensure that this defect, which was known to be quench rate dependent, could be produced in the much larger oriented samples, unoriented samples of the same dimensions were cut from the Wacker ingot and prepared in the manner described in section 4.2. It was found that only a very weak Cu^* PL signal could be detected, if at all, and most of the samples produced the PL spectrum shown in Fig. 5.33 (B). When the same experiment was repeated, however, using the same samples but cut to the smaller dimensions of 7 x 3 x 1.5 mm the spectrum shown in Fig. 6.1 was obtained showing a very strong Cu^* signal along with a medium 875 meV

signal and almost negligible SK and Cu-Cu systems. Having perfected the defect production technique, oriented samples of the required dimensions were cut for us from the Wacker ingot in King's College London and subsequently treated in

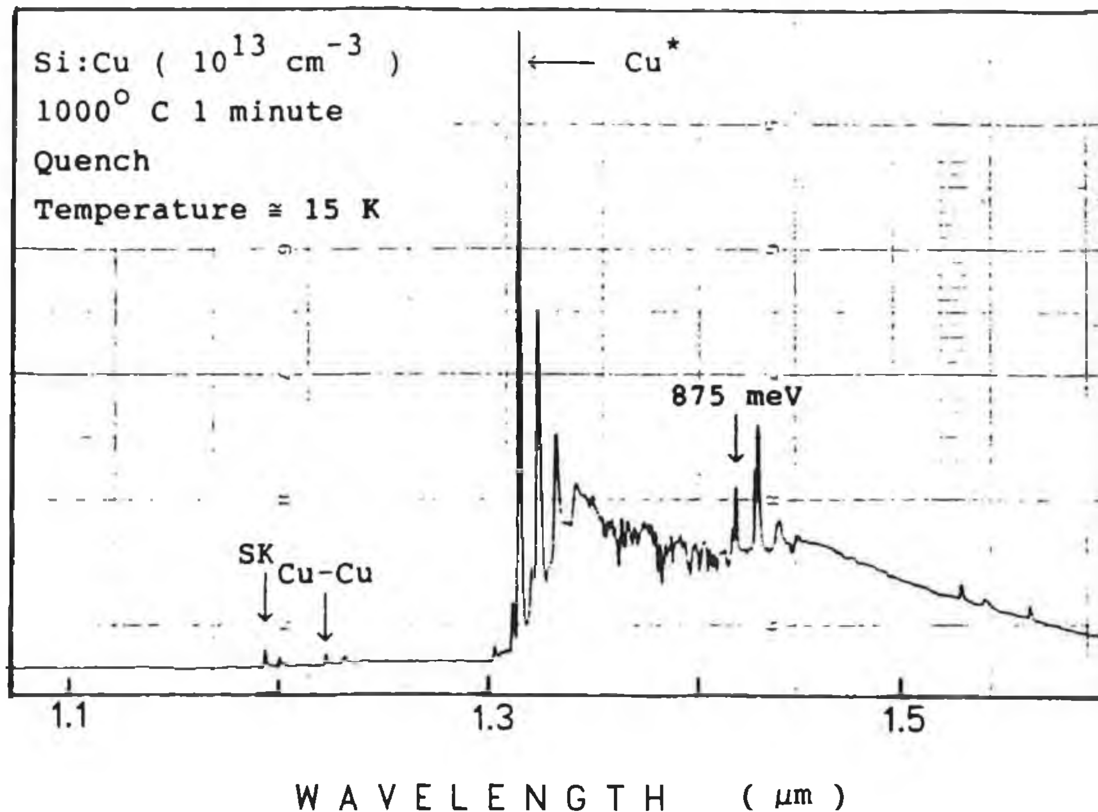

Fig. 6.1 PL spectrum of Si:Cu samples of dimensions 7 x 3 x 1.5 mm, treated as indicated in the figure. The spectrum has not been corrected for system response or water vapour absorption.

the manner outlined previously. The PL spectra obtained from all three samples were similar and closely resembled that shown in Fig. 6.1.

The uniaxial stress measurements were usually carried out in the stress cell described in section 4.6 but some data were taken at King's College London (KCL) on stress cells of similar design but with the load supplied by either hydraulic or compressed gas action.

The results of these measurements on the α and β lines of the Cu^{*} PL band are given in the following sections.

6.2.2 STRESS PARALLEL TO <111>

Fig. 6.2 shows representative stress spectra for the α and β ZPL's. Both lines are seen clearly to split into two components. The shift rates of all the stress induced components are linear, as can be seen from Fig. 6.3, indicating no interaction between these lines and any of the other higher energy ZPL's under stress along this direction.

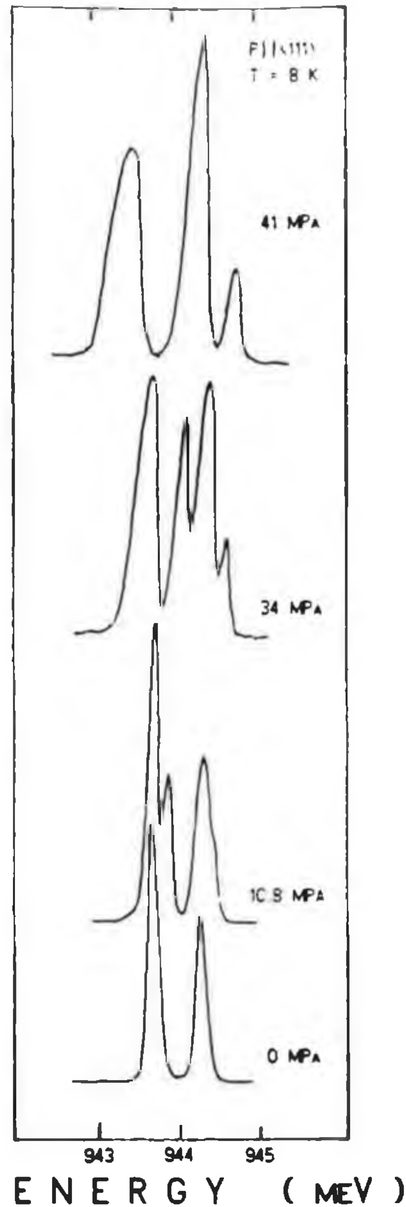

Fig. 6.2 Traces of representative stress spectra for P||<111> for a number of different stresses.

The second component has been observed to emerge from the low energy side of the alpha line component but is not seen in the data shown in Fig. 6.3. In every other respect this data is believed to be the most reliable.

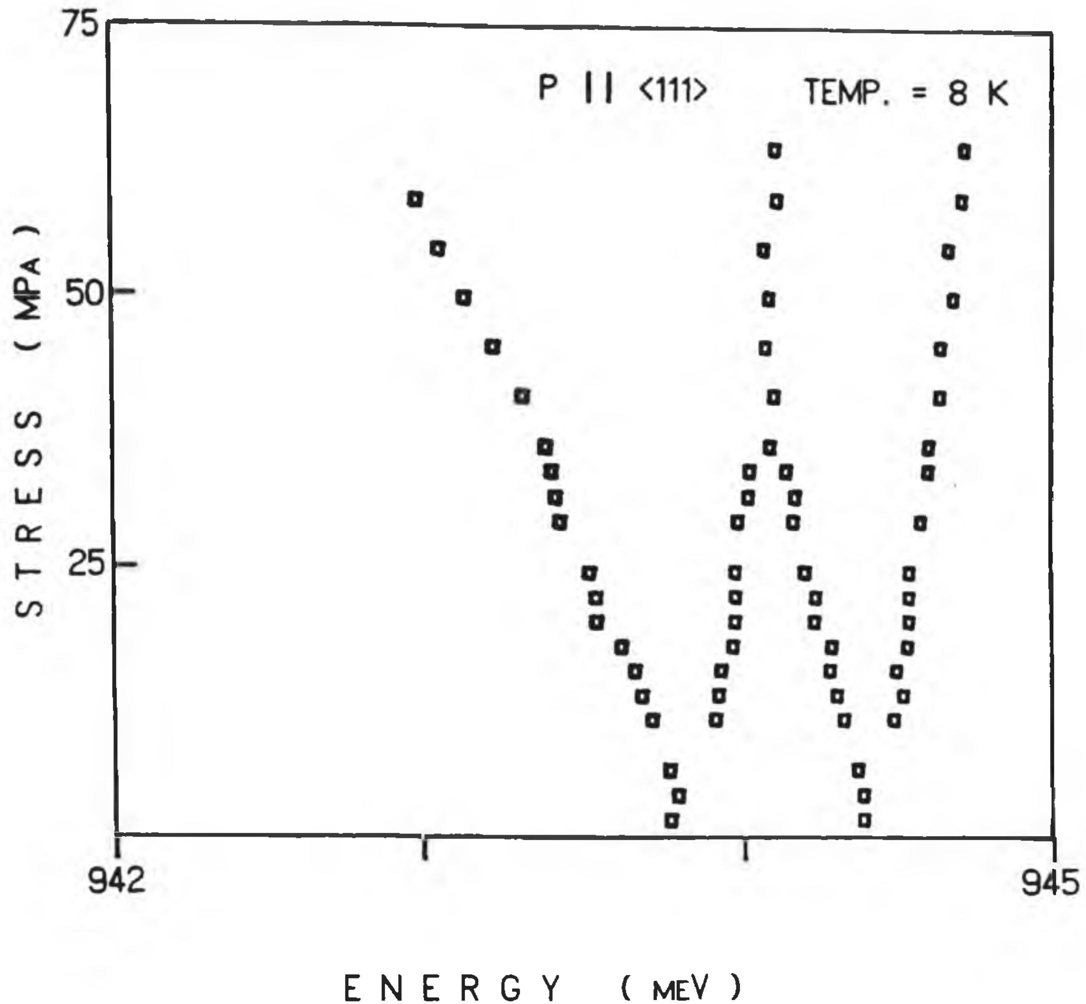

Fig. 6.3 A fan diagram of the stress induced splittings of the α and β ZPL's under <111> uniaxial stress.

6.2.3 STRESS PARALLEL TO <100>

Measurements of the α and β lines under <100> stress were taken on four separate occasions using three different stress rigs. In each case the β line was seen to split into two components. The data for the α line is not quite so straightforward. On two occasions the line seemed to split into two components and in the remaining two instances the

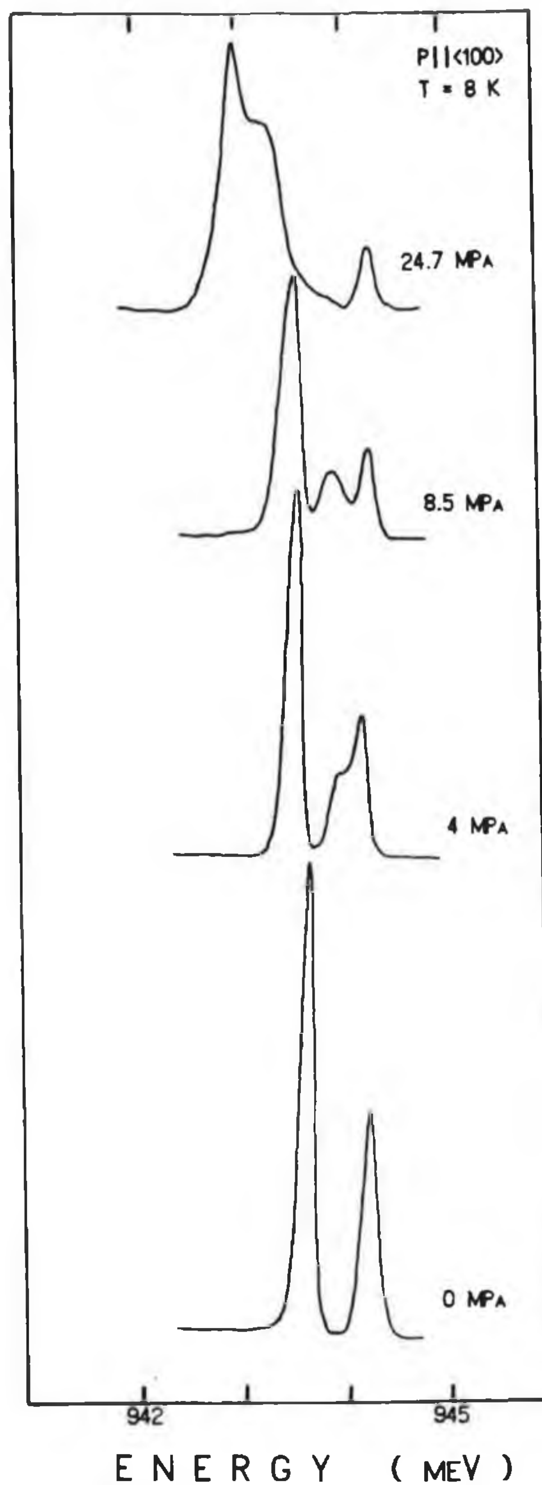

Fig. 6.4 Traces of representative stress spectra for P||<100> for a number of different stresses.

line remained unsplit but substantially broadened. The data shown in Fig.'s 6.4 and 6.5 is taken from what are believed to be the most reliable data.

Unlike the <111> data the observed shift rates are not

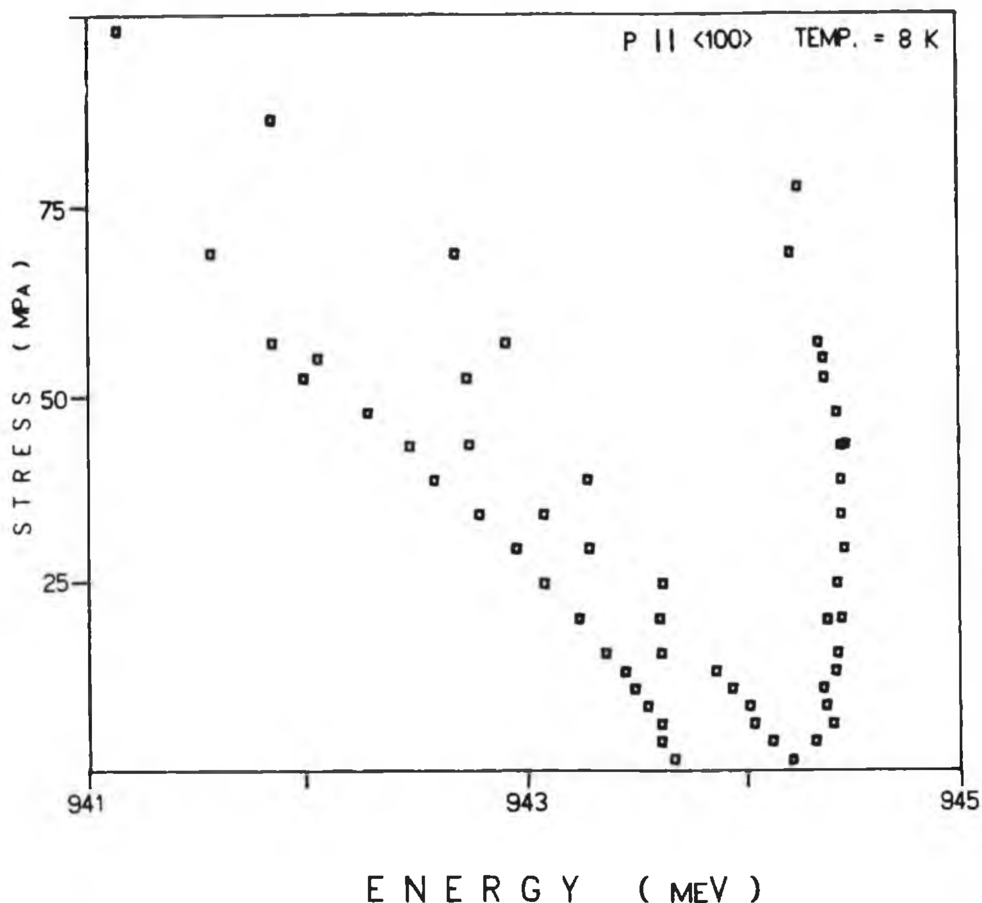

Fig. 6.5 A fan diagram of the stress induced splittings of the α and β ZPL's under <100> uniaxial stress.

linear. The high curvature of the stress components away to lower energy indicate that both levels are interacting at high stresses with some level higher in energy.

6.2.4 STRESS PARALLEL TO <110>

The signal levels from the <110> sample were by far the worst obtained from any of the three oriented samples at my disposal. Despite this the β line was observed to split into three components on both occasions that measurements along this direction were taken (on different apparatus). Spectra taken on the dispersive spectrometer in Dublin showed the α line to remain unsplit but broadened under the effect of

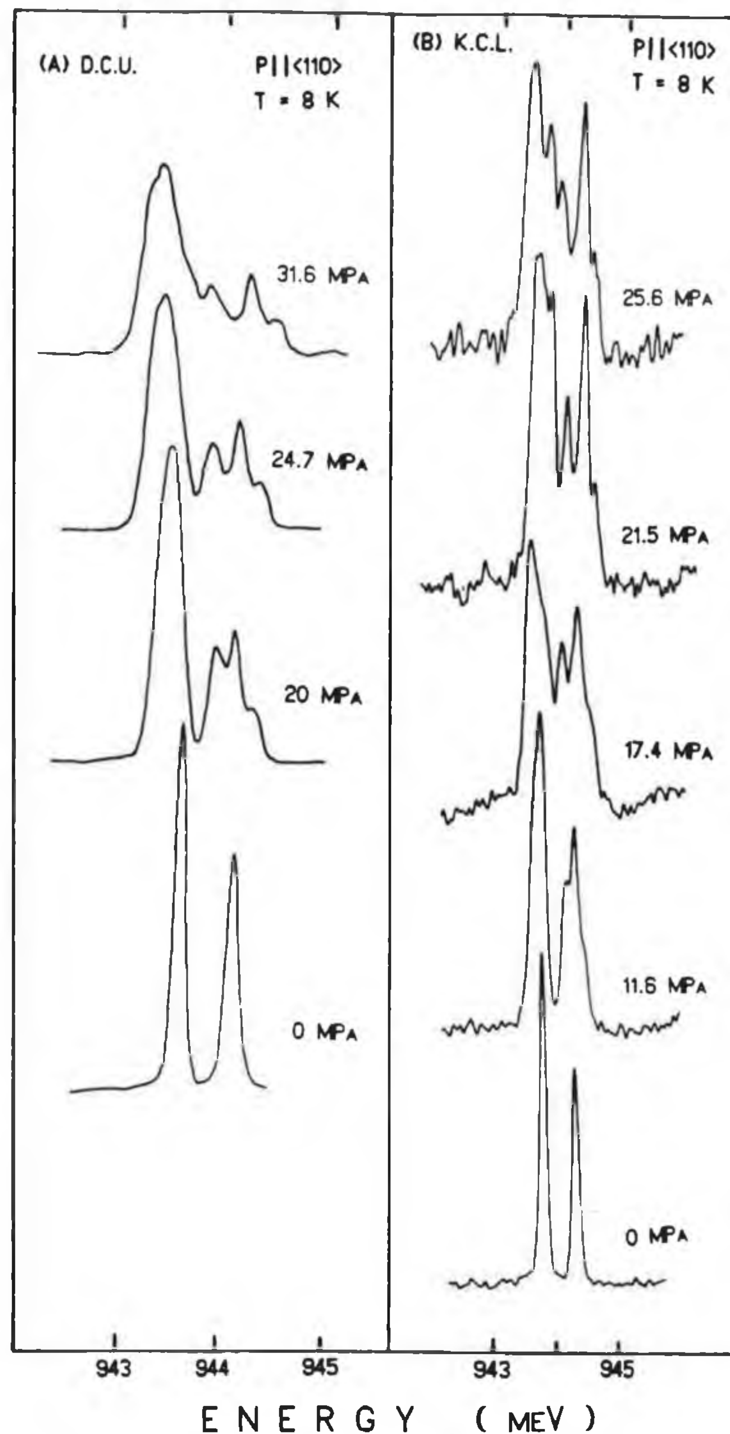

Fig. 6.6 Representative spectra of the stress induced splittings for P|| <110> observed at D.C.U. on the dispersive spectrometer (A) and at K.C.L. (B) on the F.T.I.R. system using a compressed gas load cell. The spectra were all taken at ≅ 8 K.

stress (Fig. 6.6). Measurements taken later on the F.T.I.R. spectrometer at KCL revealed one more component belonging to the α line as well as a possible third (Fig. 6.6) which is however of the same order of magnitude as the signal to noise ratio and so may not be real, especially since it is only observed once. Fig. 6.7 shows fan diagrams for both sets of data ((1) and (2)) as well as a diagram combining parts of both (3).

Once more the shift rates are found to be non-linear although not to the same degree as the <100> data, indicating some interaction between the states present.

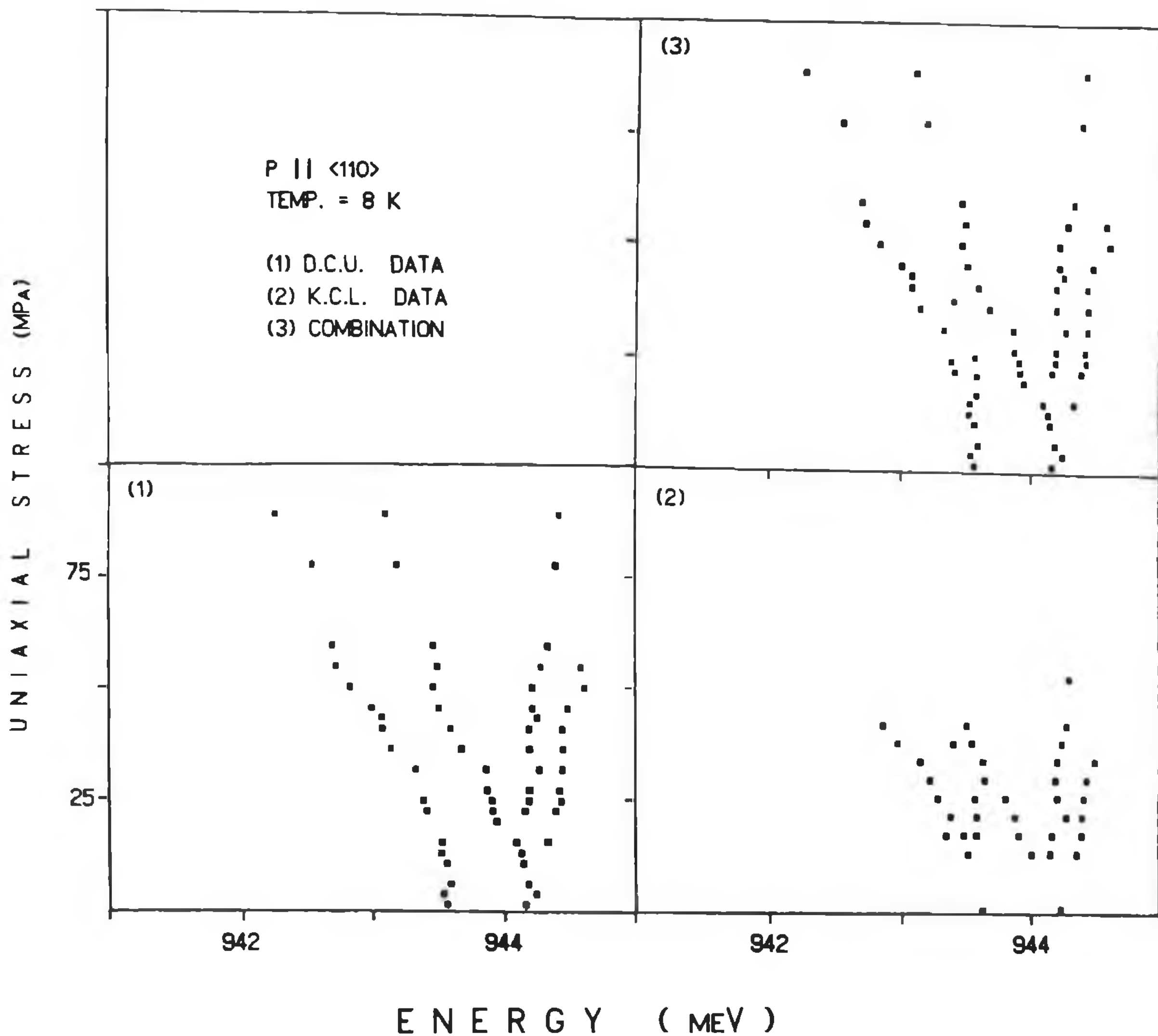

Fig. 6.7 Fan diagrams showing the stress induced splittings of the α and β lines for P||<110>. Data taken at D.C.U. (1) and K.C.L. (2) are shown as well as a diagram combining both.

6.2.5 POLARIZATION DATA

As we have already seen in chapter 3 polarization information is extremely useful when trying to determine the symmetry of a defect. In order to optimize the conditions for the collection of such data the edges, and faces not in use, of each sample were blacked off using an indelible marker before they were mounted in the stress cell. This was done to minimize internal reflections within the sample which tend to mix the polarizations.

Despite these precautions we were unable to obtain any useful polarization information from any of the samples. This is not unexpected however in the presence of severe mixing (G. Davies and M. C. do Carmo private communications). Also luminescence polarization measurements are greatly affected by internal reflections within the samples, which tend to mix the polarizations present in the PL signal.

6.3 ANALYSIS OF THE STRESS DATA

Simplified diagrams representing the observed splittings under stress of the α and β lines are shown in Fig. 6.8.

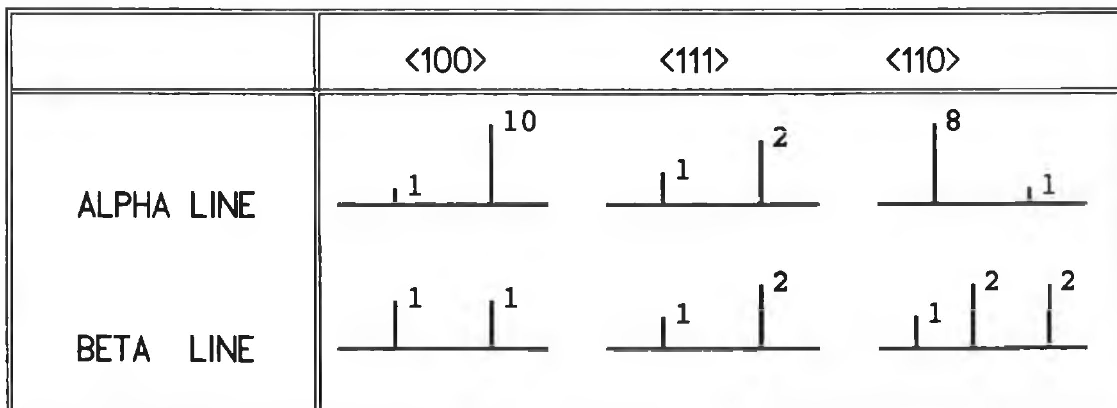

Fig. 6.8 Observed splittings and line intensities for the α and β ZPL's under the stress directions indicated.

If we compare these with the predicted splittings calculated by Fitchen (1968), reproduced in Fig. 6.9. we can see several different defect symmetries that produce similar

splittings. If we take into account the possibility that some of the stress parameters for the defects are zero then the number of possible symmetries that correspond to our findings increases even further. There is one factor however that reduces the number of likely symmetries down to just two. Non-linear shifts under <100> and <110> stresses are usually indicative of either trigonal or tetrahedral (T_d) symmetry (G. Davies. and M.C. do Carmo , private communication 1989). If we restrict ourselves to these two symmetry systems we can see that the only possible assignations to the transitions are now trigonal E to A or T_d T to A. A comparison of the predicted splittings and line intensities with the experimentally measured values is given

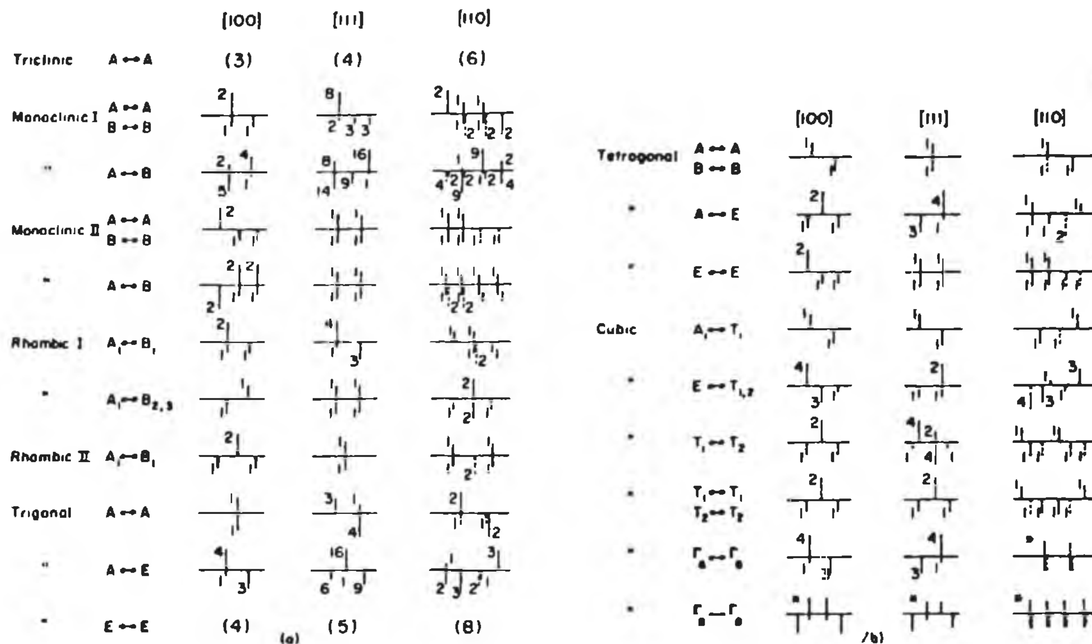

Fig. 6.9 Schematic splittings of ZPL's under uniaxial stress for various transitions at centres belonging to the eight possible symmetry systems (taken from Fitchen (1968)). The ordering of the lines is arbitrary and the relative intensities are indicated by the small numerals. The lines above the line are polarized parallel to the stress, those below perpendicular to it.

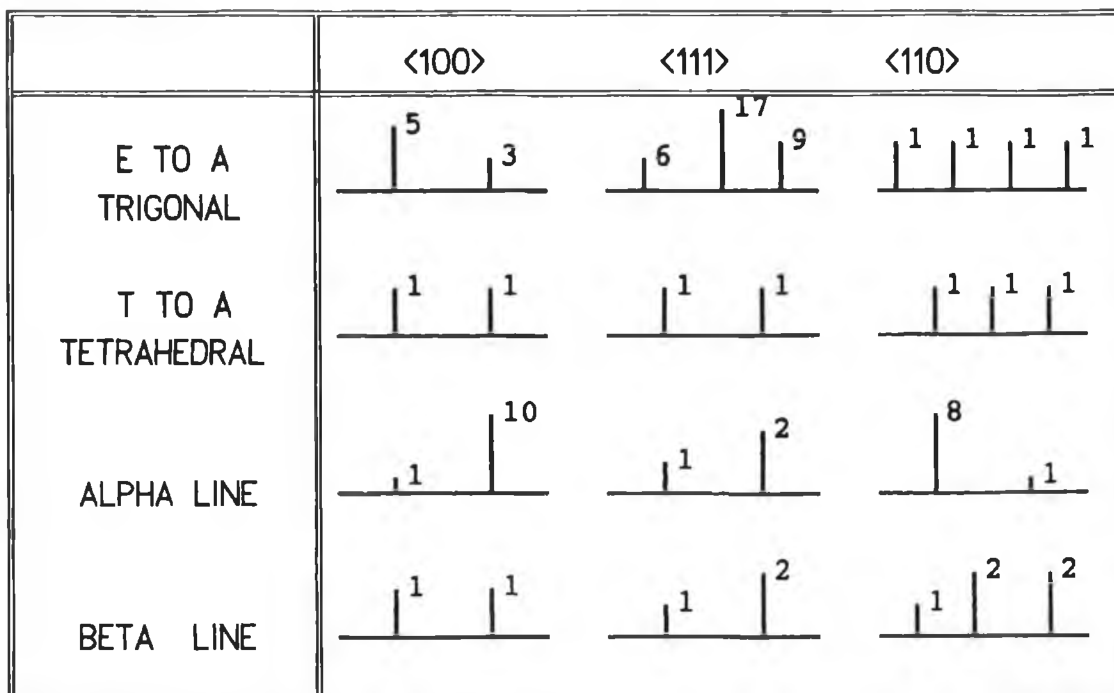

Fig. 6.10 Schematic comparison of the calculated and experimentally measured splittings and line intensities of the α and β lines under uniaxial stress.

	TRIGONAL E TO A	TETRAHEDRAL T TO A
$P \parallel \langle 100 \rangle$	$A_1 + 2B$ $A_1 - 2B$	$A + 2B$ $A - B$
$P \parallel \langle 111 \rangle$	$A_1 - 2(A_2)/3 + 4C/3$ $A_1 - 2(A_2)/3 - 4C/3$ $A + 2A$	$A + 2C/3$ $A - C/3$
$P \parallel \langle 110 \rangle$	$A_1 + A_2 + (B - 2C)$ $A_1 + A_2 - (B - 2C)$ $A_1 - A_2 + (B + 2C)$ $A_1 - A_2 - (B + 2C)$	$A - B$ $A + (B+C)/2$ $A + (B-C)/2$

Table 6.1 The theoretical shift rate equations for a trigonal E to A and tetrahedral T to A transitions as calculated by Hughes and Runciman (1968) and Kaplayanskii (1964 (b)).

schematically in Fig. 6.10, followed by Table 6.1 giving the theoretical shift rate equations calculated for these transition types (Hughes and Runciman (1967) and Kaplayanskii (1964) (b) respectively).

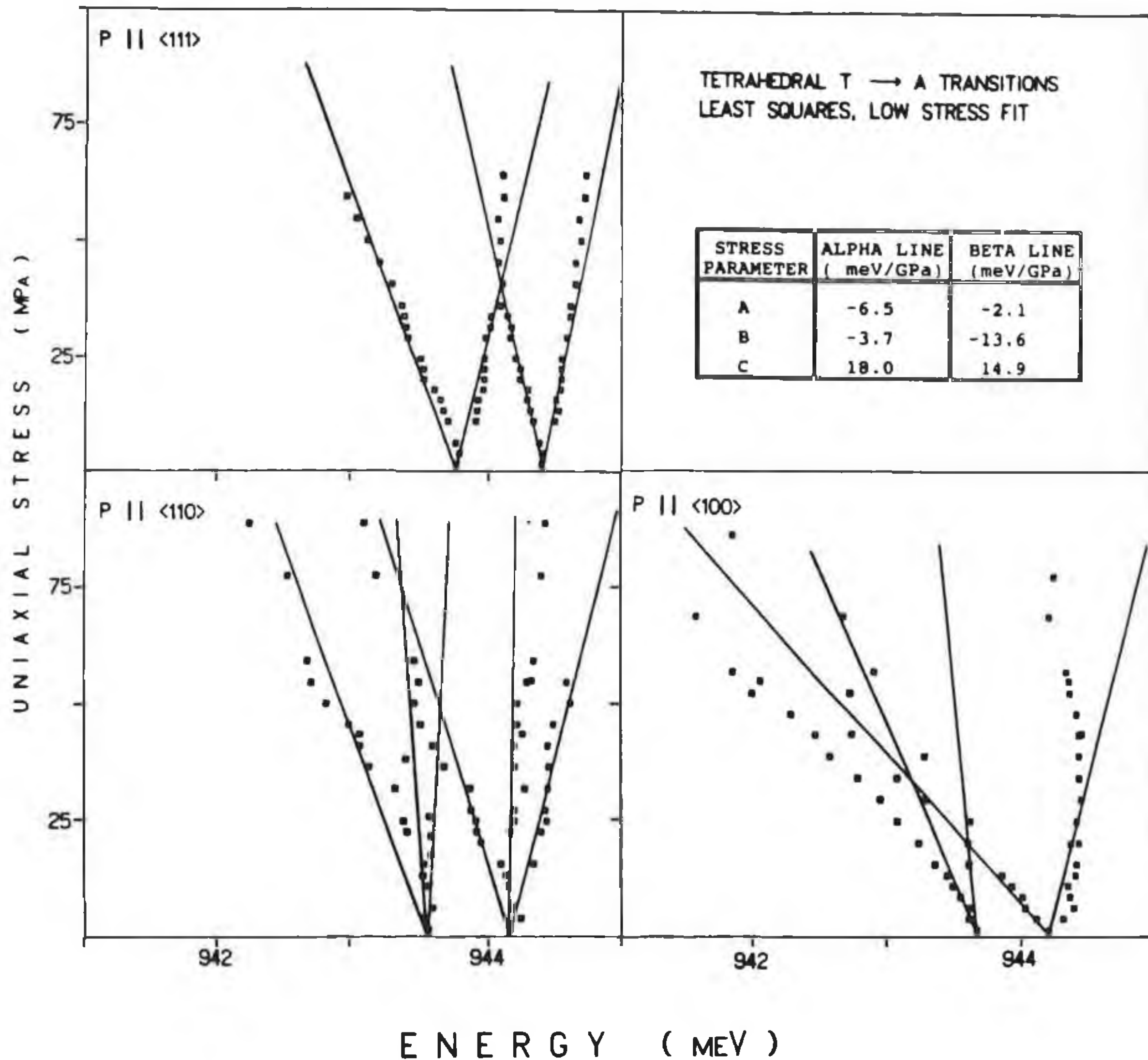

Fig 6.11 A T_d T to A fit to the experimental data in the low stress regime. The fitted parameters are as indicated.

As can be seen from Fig. 6.10 the observed splittings most resembles the T_d assignation. A least squares fit to the low stress data based on such a model is shown in Fig. 6.11. The fit is restricted to a low stress regime where the effects of

mixing between states is not too severe.

A least squares fit to the experimental data using a trigonal E to A model has also been made and yields an error of roughly the same order of magnitude as the T_d fit. In order for the trigonal model to be correct, however, this requires only two components to be observed under <111> stress which only happens if one of the stress parameters is zero. The splittings in the other two directions dictate that C, and C only be zero. This leaves the splitting under <110> stress determined by the simple expression :

$$\delta_i = A_1 \pm A_2 \pm B$$

No matter how large or small A_1, A_2 or B are these can only produce one, two or four stress induced components in a ZPL but never three as is observed for the β line. One could argue that the fourth line is there but not resolved but if this is the case we still need two more lines to be unresolved for the α line. It is for this reason that we favour the tetrahedral identification for both lines with the assumption that the α line also splits into three but only one of these components is unresolved. One unresolved component in the P||<110> direction have been observed for the Au and Pt T_d centres in silicon (Thebault et al. 1983).

Clearly a more ideal situation would be one where a fit could be made that included the interaction effects observed at higher stresses. The secular matrix describing a situation where all five ZPL's are T_d T to A transitions would have dimension 10 and be expressed in terms of 75 variables of which only 6 are at present known. Even if we limited ourselves to the α, β and γ lines the matrix would have dimension 6 and be in terms of 27 variables. In order to solve these matrices stress measurements on the other three lines are necessary. Unfortunately the signal levels obtained at the D.C.U. laboratory on the dispersive spectrometer were insufficient for any useful data to be obtained on any of the γ, δ or ε lines. Such experiments would require long term access to an F.T.I.R spectrometer such as is used at K.C.L. but unfortunately this was not possible owing to financial and scheduling problems.

6.4 ZEEMAN MEASUREMENTS

Zeeman studies were conducted on the α and β lines of the system at K.C.L. using an Oxford Instruments Spectro Mag 4 liquid helium bath cryostat that employs a superconducting magnet in a split pair arrangement to produce fields up to 5 Tesla for temperatures between 1.4 and 300 K (Canham 1983). All the results presented were taken in Voigt configuration with the sample arrangement shown in Fig. 6.12.

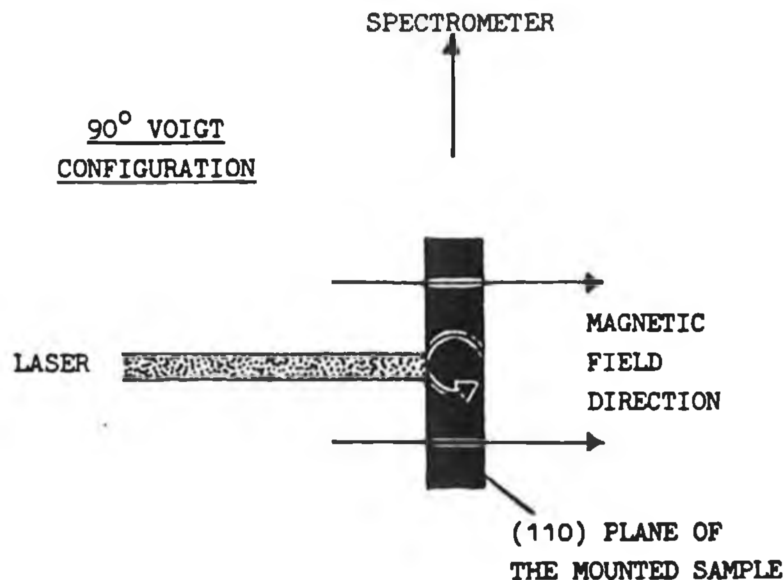

Fig. 6.12 Voigt configuration as used in the K.C.L. Zeeman system.

A <110> oriented sample was used since all three major crystallographic directions can be obtained by rotations in a <110> plane as shown in Fig. 6.13.

Representative spectra and fan diagrams for the field parallel to <110>, <111> and <100> are given in Fig.'s 6.14 and 6.15. The α line is clearly seen to be an isotropic triplet with the three components thermalizing between each other, yielding a g-value $\cong$ 2. Although the β line exhibits five components in all three directions the manifold is anisotropic with the two outer components converging towards

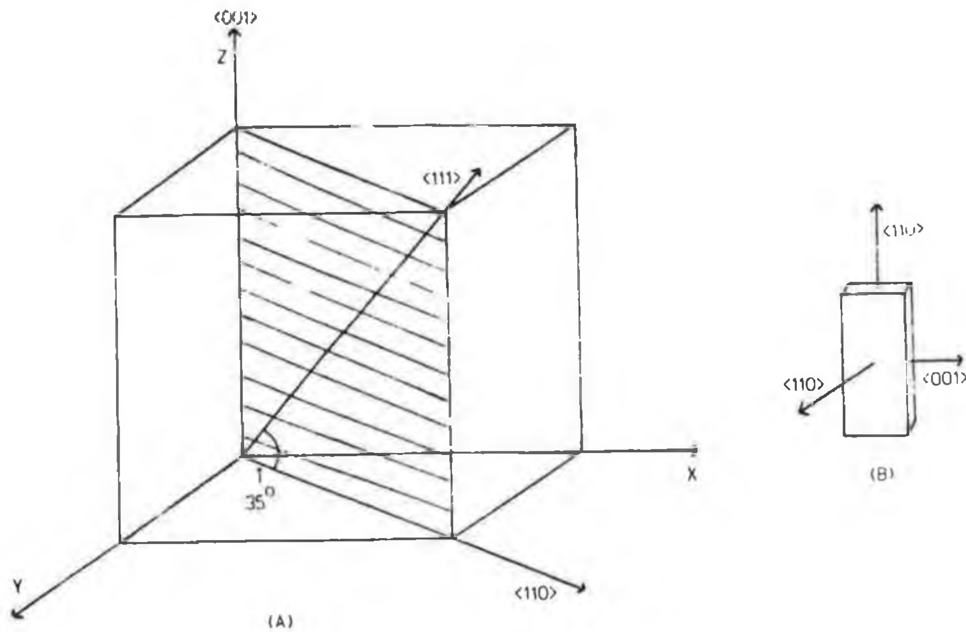

Fig. 6.13 (a) Schematic representation of how the three major cystallographic directions can be obtained from a (110) plane. (b) The face orientations of the <110> oriented sample used in the Zeeman measurements.

each other and seemingly exchanging intensities or perhaps crossing over each other at some angle near the B || <111> position. Once again no polarization information could be obtained.

The observed splittings closely resemble those reported by Merz et al. (1968) for the nitrogen defects in GaP. They constructed a secular matrix that applies to Γ_3, Γ_4 (J=2) and Γ_5 (J=1) exciton states formed from the coupling of a Γ_6 electron with a Γ_8 hole in T_d symmetry and corresponds to the most general Zeeman interaction. This matrix is given in Table 6.2.

The observed anisotropy about B||<111> and the apparent exchange of intensity around this field angle, closely resemble the Zeeman data reported by Mohring et al. (1984) for the FeB centre in silicon. Representative spectra and fan diagrams of the FeB_0^0 and FeB_1^0 lines are shown in Fig. 6.16 and the similarities can be clearly observed. The Merz et al. secular matrix was employed here also to make the fit shown

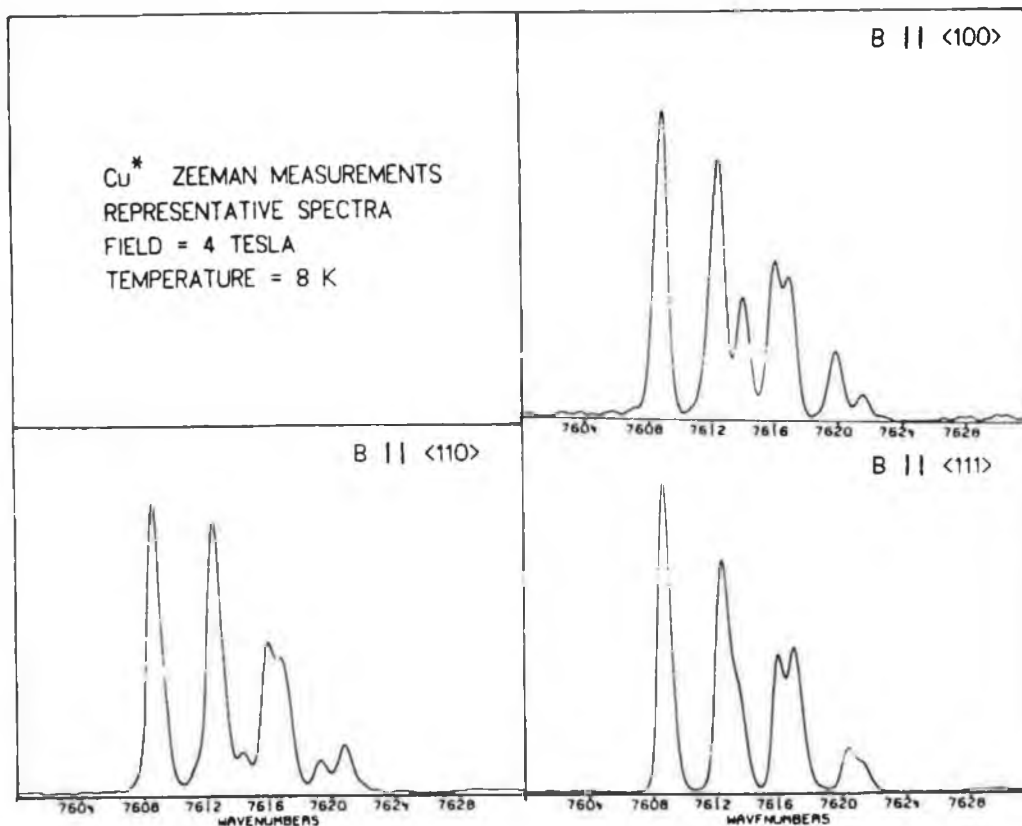

Fig. 6.14 Representative Zeeman spectra for the field along the three major crystal directions. All spectra were taken at 4 tesla and at temperatures between 6 and 9 K.

as solid lines in the diagrams. However neither I nor the groups in Aveiro or K.C.L. could reproduce their results with the parameters given in the publication. Nevertheless the Merz secular matrix was still thought to be the most promising theoretical basis for our calculations, since we were able to reproduce the data of Merz et al. for the B* line in the N trap in GaP.

A problem arises in applying this matrix to the observed data in that to do this would require the apparent exchange splitting to be reversed relative to that expected for a bound exciton. This is needed since the triplet is observed at lower energy than the quintuplet which is not usually the situation (see Fig. 3.8). A possible explanation of this

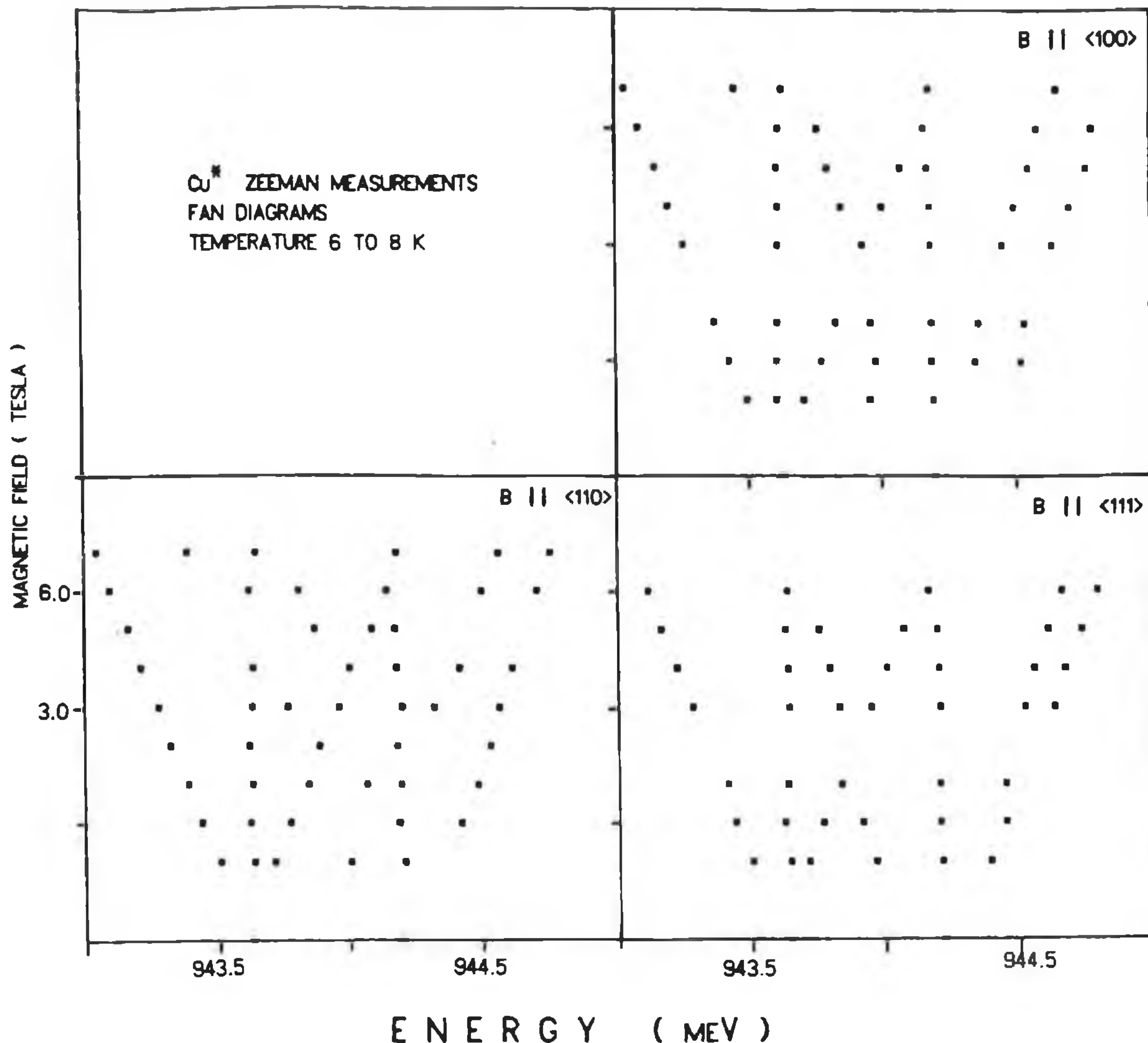

Fig. 6.15 Zeeman fan diagrams for the field along the three major crystal directions for the α and β Cu^* lines.

may come from the uniaxial stress analysis where the T_d T to A fit predicts different values of stress parameter A for each transition. The A parameter, which is found to be larger for the α line than the β line describes the hydrostatic shift rate for the level thus providing a mechanism whereby the J=1 could be shifted down below the J=2 level in the presence of a local strain about the defect. The validity of such an assumption is investigated in a following section. A fit to the experimental data using this matrix was made and the results are shown in Fig. 6.17. The fitted parameters are given in Table 6.3. The eigenvalues and eigen vectors of the matrix were calculated using NAG routine F02AXF on a VAX 1

		Γ_5			Γ_4			Γ_3	
		1	2	3	1	2	3	1	2
Γ_5	1	ε_5	$-i\gamma_1 H_z$	$i\gamma_1 H_y$	0	$-i\sqrt{3}\delta_1 H_z$	$-i\sqrt{3}\delta_1 H_y$	$-i\sqrt{3}\delta_2 H_x$	$-i\delta_2 H_x$
	2		ε_5	$-i\gamma_1 H_x$	$-i\sqrt{3}\delta_1 H_z$	0	$-i\sqrt{3}\delta_1 H_x$	$i\sqrt{3}\delta_2 H_y$	$-i\delta_2 H_y$
	3			ε_5	$-i\sqrt{3}\delta_1 H_y$	$-i\sqrt{3}\delta_1 H_x$	0	0	$i2\delta_2 H_z$
Γ_4	1				ε_4	$i\gamma_2 H_z$	$-i\gamma_2 H_y$	$-i\gamma_3 H_x$	$i\sqrt{3}\delta_3 H_x$
	2					ε_4	$i\gamma_2 H_x$	$i\gamma_3 H_y$	$-i\sqrt{3}\delta_3 H_y$
	3						ε_4	$i2\gamma_3 H_z$	0
Γ_3	1							ε_3	0
	2								ε_3

This is a complex Hermitean matrix where :

H_i = the component of the magnetic field along the ith direction multiplied by the Bohr magneton.

γ_1 gives the low field splitting of the Γ_5 state.

γ_2 and γ_3 determine the splitting of the ($\Gamma_3 + \Gamma_4$) manifolds.

δ_1 and δ_2 mix the Γ_4 and Γ_5, or Γ_3 and Γ_5 states respectively and cause non-linear splittings at higher fields.

Table 6.2 The interaction matrix constructed by Merz et al. (1968) to fit the observed splittings of J=1 and J=2 exciton states.

mainframe computer. Since all the splittings appear to be linear and there is no evidence of mixing at higher field values, both the delta parameters were set to zero.

γ_1	2.0
γ_2	1.22
γ_3	1.26
δ_1	0
δ_2	0

Table 6.3 Parameters fitted to the experimental data using the Merz et al. (1968) matrix.

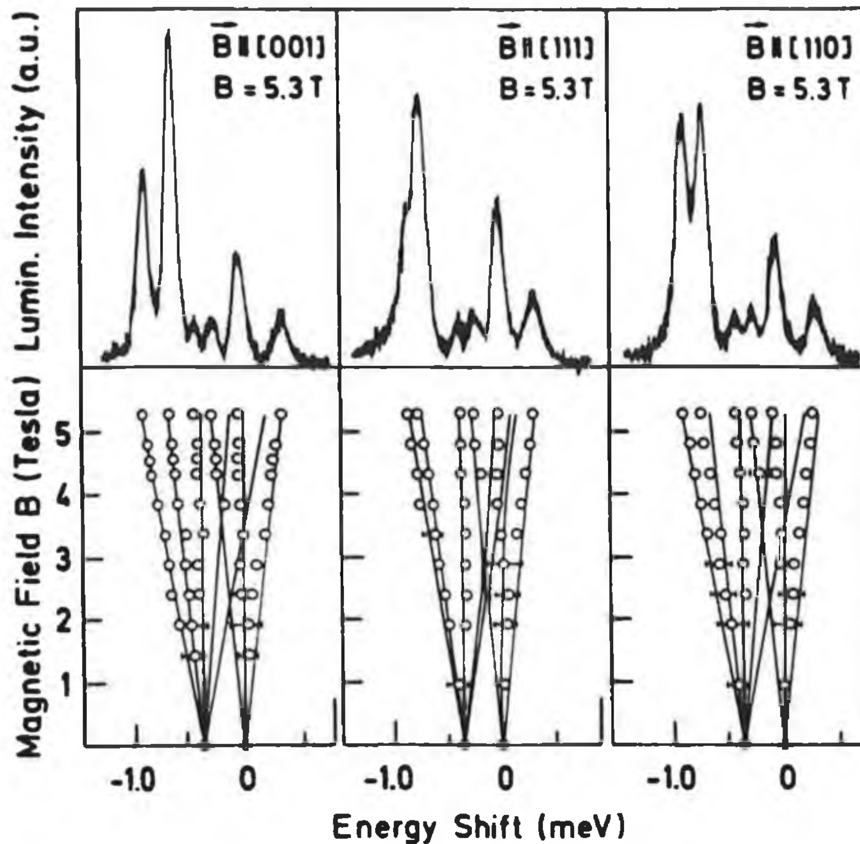

Fig. 6.16 Representative spectra and fan diagrams of the Zeeman data reported by Mohring et al. (1984) for the iron - boron centre in silicon.

The theoretical angular dependence of the J=1 and J=2 Zeeman split manifolds was calculated using the Merz et al. matrix and two "Numerical Recipes" fortran subroutines (Jacobi and Eigsrt) run on a Prompt AT P.C. The results are graphed in Fig. 6.18. The program was calibrated by successfully reproducing the angular dependence for the B line of the GaP:N system reported by Merz et al. (1969) Only slight anisotropy is expected in the J=2 manifold of the order of 0.01 meV which is a factor of ten smaller than that needed to fully explain the observed merging of the |2,±2> and |2,±1> components (using the $|J,m_j\rangle$ notation). Neither is any exchange of intensity between the lines predicted. The possibility that the data could be explained by a misalignment of the sample in the cryostat during the

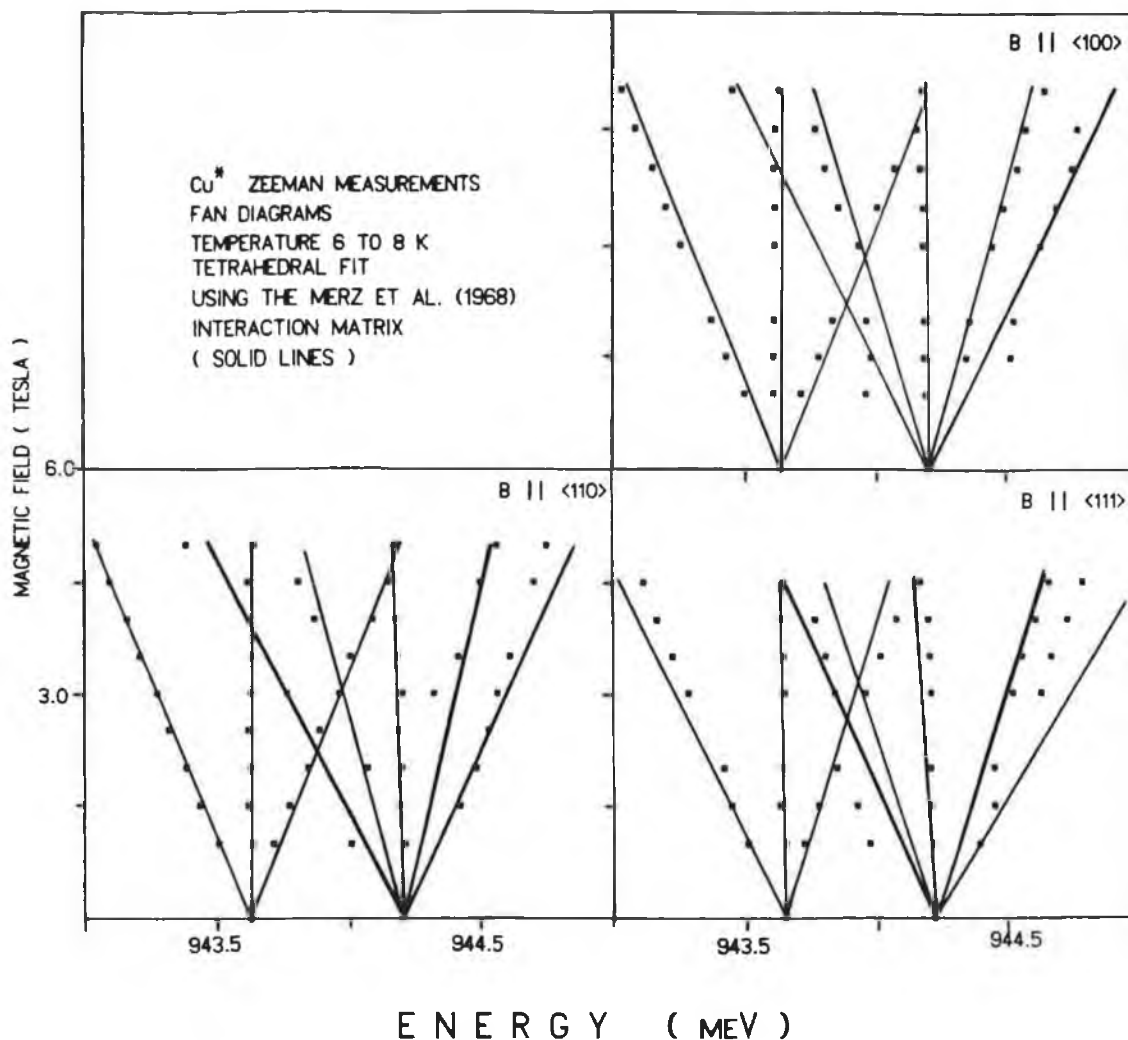

Fig. 6.17 Fan diagrams showing the experimental data for B along the three major crystal axes as well as the splitting predicted by the Merz matrix (solid lines) using the parameters given in Table 6.23.

experiment was investigated by calculating the H_x, H_y and H_z components of the matrix using spherical polar co-ordinates. This allowed us to incorporate a misallignment either in or out of the <110> plane that the sample was supposedly rotated in during the experiment. However neither systematic misalignments in or out of the plane or totally random misalignments could produce energy shifts of the order of magnitude required, all being at least a factor of ten too

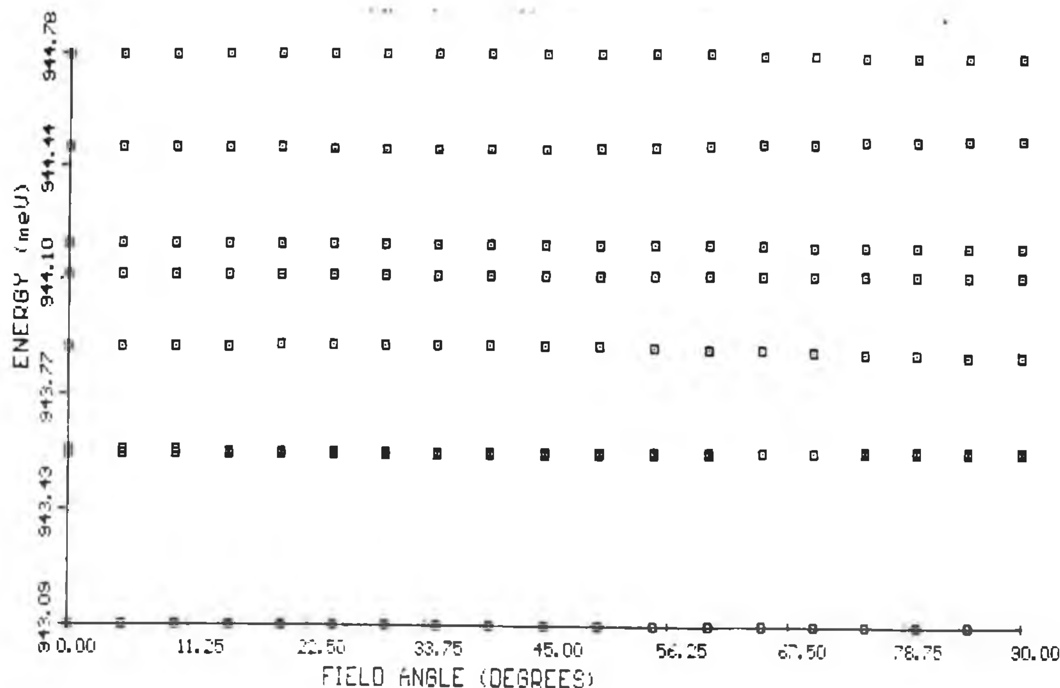

Fig. 6.18 Theoretical angular dependence of the Zeeman splitting of J=1 and J=2 manifolds as predicted by the Merz et al. (1968) secular matrix.

small.

A further modification to the Merz et al. matrix was the inclusion of four more constants (P,Q,R and S) calculated by Killoran et al. (1982) to account for the effect of a tetragonal strain about the defect site that might produce the observed angular dependence. Unfortunately this did not produce an acceptable fit either.

The fortran program used to obtain the eigenvalues and eigenvectors of all the previously mentioned matrices is listed in Appendix 1.

The apparent inversion of the exchange splitting between the J=1 and J=2 lines ties in nicely with the different hydrostatic stress parameters predicted from the T_d T to A

transitions assignation in the uniaxial stress analysis. One must however address the question of whether such an inversion is likely.

The elastic constants of pure silicon at low temperature are

$$C_{11} = 168 \text{ GPa}$$

$$C_{12} = 65 \text{ GPa} \qquad \text{(Davies 1989)}$$

$$C_{44} = 80 \text{ GPa}$$

the fractional change in volume of the unit cell is equal to the trace of the strain tensor i.e.

$$\Delta V/V = \text{trace } \varepsilon_{ij}$$

where ε_{ij} is the strain tensor.
For cubic or tetrahedral systems :

$$\text{trace } \varepsilon_{ij} = \text{trace } \sigma_{ij}/ C_{11}+ 2C_{12}$$

where σ_{ij} is the stress tensor. From the uniaxial stress analysis we know that the relative hydrostatic shift rate of the α and β lines is 4.4 meV/ GPa. If we assume an original exchange splitting in the absence of hydrostatic shift of 2 meV, which is not unreasonable, then the pressure needed to produce the observed zero stress splitting of 0.57 meV is 0.57 GPa.

$$\Delta V/V = 0.57 / 168 +2(65) = 1.9 \times 10^{-3} \cong 0.2 \%$$

So a change of as little as 0.2 % in the volume of the unit cell could produce the observed inversion of the J=1 and J=2 states via the hydrostatic shift produced by a defect with tetrahedral symmetry.

6.5 DEFECT IDENTITY AND DIFFUSION RATE CONSIDERATIONS

If we assume for a moment that the defect is a single copper atom lying in the interstitial tetrahedral site then we know from the diffusivity equation given in chapter 1 :

$$D = D_o \exp(-Q/kT)$$

E. R. Weber (1983) calculated the values of D_o and Q for copper in silicon to be 4.7 X 10^{-3} and 0.43 eV respectively which gives the diffusivity at room temperature of 20° C as :

$$D = 1.9 \times 10^{-10} \text{ cm}^2/\text{sec}$$

which corresponds to a linear diffusion rate of 7.81 X 10^{-6} cm/sec. We already know from atomic absorption measurements that the copper concentration in the starting material is ≅ 10^{13}cm^{-3} i.e. one copper atom for every 10^{-13} cm^3. If we assume this volume to be a cube then the longest possible distance between adjacent copper atoms is the body diagonal length of a cube of this same volume which turns out to be = 7.97 X 10^{-5}cm, only a factor of ten larger than the expected diffusion rate. In the light of these simple calculations one would expect any luminescence arising from defects consisting of a single interstitial copper atom to deteriorate quite quickly after room temperature storage over a period of days if not even hours as the single atoms diffuse through the sample, encounter other similar atoms and form more complex defects. This ,however, is not the case for samples exhibiting the Cu^* PL system. In fact samples that had been stored at room temperature for periods of up to eighteen months showed no noticeable deterioration in signal.

There is the possibility that the copper has taken up a substitutional site but this is unlikely since all the indications are that substitutional TM diffusion is a slow process, often requiring the presence of a second TM element as in the indirect substitutional diffusion process of manganese via copper substitution reported by Ludwig and

Woodbury (1964) and even then the process takes place over a period of hours and not minutes as is the case required here.

Recall

$$D = D_o \exp(-Q/kT)$$

with units of cm^{-2}/sec. If we convert this to linear distance travelled r in one second at temperature T we get :

$$r = (D_o/\pi)^{1/2} . \exp(-Q/2kT)$$

Thus the total distance travelled by a single copper atom during a one second quench from 1000^oC to room temperature would be given by the integral :

$$r_q = (D_o/\pi)^{1/2} \int_{293}^{1273} \exp(-Q/2kT).dT$$

Solving this using the Eureka mathematical package and the presently accepted values for D_o and Q gives a value of :

$$r_q = 0.79 \text{ cm}$$

This figure is valid only if the copper atom does not meet another contaminant as the sample cools which, given the dimensions of the samples seems highly unlikely. These calculations would suggest that if copper is involved in the defect then it would almost certainly be accompanied by some other contaminant, which more than likely would be at least one if not more, copper atom.

If we are to maintain our belief in the tetrahedral nature of the defect then the most obvious choice left to us is four interstitials surrounding a substitutional site in an tetrahedral arrangement similar to that already reported for the Mn_4 defect (Conzelmann 1984) and the Li_4 radiation damage centre (Canham 1983) in PL and the NL22 Fe related EPR centre reported by Muller et al. (1982). All of the previous defects have been shown to be very stable at room

temperature. Another factor in its favour is the fact that copper is known to form clusters and aggregates during high temperature quenches (Weber et al. 1981, Conzelmann 1986). If this is the case then the Cu^* defect would be an ideal candidate for isotope studies.

This tetrahedral assignation does lead to some uncomfortable questions. Why should two transitions occurring on the same centre have different reactions to hydrostatic pressure ? The fact that α line splits isotropically with a g value $\cong$ 2 indicates the origins of this state to be band-like. If we adhere to the Merz formulation then both the α and β lines should originate from the same bandlike states but this in itself means that their reactions to hydrostatic pressure should not differ.

Given the low concentration of copper needed to form the centre and keeping in mind the tentative suggestion that the defect consists of four interstitial atoms these facts would indicate that the 1014 meV copper-related defect also incorporates at least four copper atoms. Isotope studies conducted by Weber et al. (1981), although not conclusive, were able to ascertain that at least two copper atoms are needed for the formation of this centre. The results of our studies are not inconsistent with this hypothesis.

Given theoretical fits to the Zeeman and stress data are reasonably good, we conclude that the 943.7 meV Cu^* luminescence is due to recombination of an exciton at a centre of T_d or near T_d symmetry. The inversion of the J=1 and J=2 exciton states observed in this case can be accounted for on the basis of the stress data, a volume contraction of only 0.2 % being sufficient to produce the observed effects. Combining all the information deduced from the uniaxial stress and Zeeman analysis, the data suggest that the Cu^* PL system is produced by a defect possibly consisting of four interstitial copper atoms in a tetrahedral arrangement about some common centre of unknown origin.

CHAPTER 7 : CONCLUSIONS AND SUGGESTIONS FOR FURTHER WORK

7.1 CONCLUSIONS

All the PL centres discussed in the last two chapters can be classified as being either zinc or copper related.

Table 7.1 gives a compilation of selected data collected for all the PL centres discovered in the course of the research for this thesis.

In the case of the zinc related systems, all are consistent with IBE recombination at defects which probably involve at least two constituent atoms. They all exhibit sharp zero phonon lines as well as well structured phonon sidebands indicating moderate to weak crystal field modulation of the defect excited states. The Zn_A and Zn_B defects form a smaller sub-class of their own since they both have complex ground states similar to those reported for the indium and thallium defects in silicon (Thewalt 1982). The 919 and 945 meV systems are both well behaved in terms of total intensity versus temperature and although no similar measurements were carried out on the 1060 meV system, the luminescence decay time versus temperature behaviour is well understood.

The Mn_i-Zn_s identification suggested by Henry et al. (1987) for the 945.8 meV PL system is shown to be incorrect although the participation of zinc in the formation of the defect still seems likely.

The 919 and 943.7 meV systems both show striking phonon replica features which closely resemble that reported for the 1014 meV copper related system (Weber et al. 1981).

Uniaxial stress and Zeeman studies on the two lowest energy transitions of the 943.7 meV Cu^* PL system suggest that the luminescence arises from J=1 and J=2 exciton states bound to a tetrahedral copper related defect that probably consists of more than one copper atom but in the absence of isotope study no definitive statement can be made. Zeeman studies on the two main ZPL features of the SK PL system reveal singlet - triplet exciton states expected from the coupling of a j=3/2

SYSTEM	ZPL ENERGY (meV)	DOMINANT PHONON ENERGY (meV)	EXCITON BINDING ENERGY (meV)	ECHANGE SPLITTING (meV)	LIFETIME AT 15 K (μS)	IMPURITY
Zn^* SYSTEM	945.8 944.8	10.3, 19.3,35 64	75			ZINC
Cu-Zn SYSTEM	919.8 924.2	6.3	115	14.3	900	COPPER ZINC
1059.9 SYSTEM	1059.9 1075.1	4.8,8.0 63.5	62.5	11.5	240	IRON ZINC
Zn_A SYSTEM	1132.4 1130.4 1129.8 1126.9 1126.5 1123.5 1120.7	11.8 63.5			15	ZINC
Zn_B SYSTEM	1093.9 1090.7 1088.4 1086.2	39.4 40.4 63.5			300	ZINC
Cu^* SYSTEM	943.67 944.24 946.24 952.56 954.20	6.45	85			COPPER
SK SYSTEM	1033.5 1033.6 1040.1 1040.2					COPPER

Table 7.1 A compilation of selected data for the seven new PL systems investigated in this thesis.

hole and a j=1/2 electron in the presence of a strong crystal field and a central cell potential (Dean and Herbert 1979) similar to that reported by Dean et al. (1973) for the S_P - Ge_P nearest neighbour pair in GaP.

7.2 SUGGESTIONS FOR FURTHER WORK

The analysis of the many PL centres reported in this thesis is not completed and much work remains to
be done on most of the defects discussed. An in depth analysis of the SK system has already been undertaken in collaboration with M. H. Nazare in Aveiro and these results will be presented in the 1989 M.R.S. conference in Boston.

With respect to the Cu^* system the most urgently required work would be corroboration of the uniaxial stress measurements, preferably on a F.T.I.R. spectrometer, full angular dependence of the Zeeman splittings, isotope studies to accurately determine the chemical identity and numbers involved of the constituent atoms, and finally a much more exhaustive investigation of the luminescence intensity Vs. temperature behaviour. With the increase in diversity of high power, low cost tunable solid state lasers on the market, PLE on the transitions could soon be a possibility. Such measurements would be of inestimable benefit especially since none of the centres discussed in this thesis were observed in absorption.

In general it would be true to say that isotope studies on all the PL centres would be desirable but given the cost of purchasing the isotopes and the ambiguity involved in interpreting the small effects produced in TM related defects, such measurements are not a realistic possibility in the near future.

In relation to producing the TM related defects the whole fabrication process loses its scientific integrity at the diffusion stage, since it is extremely difficult, wasteful and expensive to maintain a controlled environment in the furnace. More time should be devoted to the study of

implanted materials rather than persisting with diffused silicon, since the contaminant type, concentration and distribution can all be controlled to a much greater extent with the former method. The combination of ion implantation and rapid thermal annealing using lasers or high power arc lamps holds most promise for the controlled preparation of silicon crystals doped with selected transition metal impurities.

APPENDIX 1

The following pages contain a listing of the fortran program COMHERM.FOR that I used to diagonalize all the secular matrices mentioned in the section of chapter 6. dealing with the Zeeman analysis using a Prompt AT 12 MHz P.C.and a Microsoft F77 fortran package. All the stress secular matrices were diagonalized using the NAG F02AXF routines on the VAX. The program used is almost identicle to the listing given below except for the call statement invoking the subroutine and for a small adjustment to the write statements that differ from monitor to monitor.

The NAG routines were found to give identicle solutions to the Numerical Recipes subroutines if given the same correct matrix. Curiously, there seemed to be no discernable difference between the answers obtained using single precision and those using double precision parameters.

COMHERM.FOR

```
C ***************************************************************
C PROGRAM TO CALCULATE THE EIGENVALUES OF THE MAGNETI C
C INTERACTION MATRIX FOR SINGLE EXCITONIC STATES BASED ON A
C MATRIX COMBINED FROM J L MERZ ET AL. PHYS REV 188,3,P-1238
C (1968) AND N KILLORAN ET AL. J PHYS       C (1982)
C ***************************************************************

C MATRIX TO BE DIAGONALIZED IS HERMITEAN

C OUTPUT OF PROGRAM IS OBSERVED TRANSITION ENERGIES.

      REAL A(8,8),C(8,8),V(16,16),X(16,16),
    1 ANG,ANGRAD,TET,TETR,
    2 W(16),D(16),
    3 G1,G2,G3,D1,D2,E3,E4,E5,H,B,HX,HY,HZ,SQ,P,Q,R,S

      INTEGER N,I,J,NROT,NP,K,KP

      OPEN(10,FILE='ANG60.DAT',STATUS='NEW',ACCESS='SEQUENTIAL'


      N=8
      NP=16
      KP=16

C DEFINE THE MERZ MATRIX PARAMETERS
C D1=(0.5)*(G1-G2)
C D2=((0.5)*(G1+G2))-G3
```

```
      D1=0.215
      D2=0.21

      WRITE(*,*)D1,D2

      E3=944.186
      E4=944.186
      E5=943.624

      WRITE(*,*)E3,E4,E5

      B=0.05788

      H=4.5

      G1=2.0
      G2=1.2
      G3=1.11

      WRITE(*,*)G1,G2,G3

C DEFINE THE KILLORAN MATRIX PARAMETERS
      P=0.0
      Q=-P
      R=0.0
      S=0.0

C ANG = THE ANGLE OF ROTATION DURING THE EXPERIMENTS
C = THE PLANE CONTAINING <110> AND <001>
C TET = THE ANGLE BETWEEN THE EXPERIMENTAL PLANE
C OF ROTATION AND THE Y-AXIS ASSUMED TO BE 45 UNDER
C CORRECT ALLIGNMENT


   DO 250 K=0,18

   ANG=00.0+(5.0*K)
   WRITE(*,*)ANG
   ANGRAD=ANG/57.295779
   TET=60.0
   TETR=TET/57.295779

C DEFINE THE COMPONENTS OF MAGNETI      C FIELD ALONG
C THE CARTESIAN CO-ORDINATE AXES USING SPHERICAL
C POLAR CO-ORDINATES
   HX=H*COS(ANGRAD)*SIN(TETR)
   HY=H*COS(ANGRAD)*COS(TETR)
   HZ=H*SIN(ANGRAD)

   WRITE(*,*)H
   WRITE(*,*)HX,HY,HZ

C DEFINE REAL MATRIX
   DO 210 I=1,N
   DO 200 J=1,N
           A(I,J)=0.0
200     CONTINUE
210     CONTINUE
```

```
      A(1,1)=E5-(R/2.0)
      A(2,2)=A(1,1)
      A(3,3)=E5+R
      A(4,4)=E4-(Q/2.0)
      A(5,5)=A(4,4)
      A(6,6)=E4+Q
      A(7,7)=E3-P
      A(8,8)=E3+P

      A(4,1)=-S
      A(1,4)=-S
      A(2,5)=S
      A(5,2)=S

C  DO 215 I=1,N
C  WRITE(*,*) A(I,I)
C215     CONTINUE




C DEFINE IMAGINARY MATRIX
      C(1,2)=-G1*B*HZ
      C(1,3)=G1*B*HY
      C(1,5)=-SQRT(3.0)*D1*B*HZ
      C(1,6)=-SQRT(3.0)*D1*B*HY
      C(1,7)=-SQRT(3.0)*D2*B*HX
      C(1,8)=-D2*B*HX

      C(2,3)=-G1*B*HX
      C(2,4)=-SQRT(3.0)*D1*B*HZ
      C(2,6)=-SQRT(3.0)*D1*B*HX
      C(2,7)=SQRT(3.0)*D2*B*HY
      C(2,8)=-D2*B*HY

      C(3,4)=-SQRT(3.0)*D1*B*HY
      C(3,5)=-SQRT(3.0)*D1*B*HX
      C(3,8)=2.0*D2*B*HZ

      C(4,5)=G2*B*HZ
      C(4,6)=-G2*B*HY
      C(4,7)=-G3*B*HX
      C(4,8)=SQRT(3.0)*G3*B*HX

      C(5,6)=G2*B*HX
      C(5,7)=-G3*B*HY
      C(5,8)=-SQRT(3.0)*G3*B*HY

      C(6,7)=2.0*G3*B*HZ

      DO 311 I=1,N
      DO 310 J=I,N
              C(J,I)=-C(I,J)
310       CONTINUE
311       CONTINUE

C THE JACOBI SUBROUTINE IS DESIGNED TO DIAGONALIZE
C REAL SYMMETRIC MATICES. WE HAVE DEFINED A COMPLEX
C HERMITEAN MATRIX OF THE FORM A+iC OF DIMENSION 8.
```

```
C THIS CAN STILL BE DIAGONALIZED USING THIS SUBROUTINE
C BY CREATING A MATRIX OF DIMENSION 16 OF THE FORM
C                A   -B
C                B    A
C AND DIAGONALIZING IN THE APPRROPRIATE MANNER.

  DO 313 I=1,8
  DO 313 J=1,8
  X(I,J)=A(I,J)
313     CONTINUE

  DO 201 I=9,16
  DO 201 J=9,16
  X(I,J)=A((I-8),(J-8))
201     CONTINUE

  DO 202 I=9,16
  DO 202 J=1,8
  X(I,J)=-C((I-8),J)
202     CONTINUE

  DO 203 I=1,8
  DO 203 J=9,16
  X(I,J)=-C(I,(J-8))
203     CONTINUE


C  DO 216 I=1,N
C  DO 216 J=I,N
C  WRITE(*,*) A(I,J)
C216     CONTINUE

  CALL JACOBI(X,NP,KP,D,V,NROT)
C NUMERICAL RECIPE TO DIAGONALIZE A SYMMETRI      C MATRIX

  CALL EIGSRT(D,V,NP,VP)
C NUMERICAL RECIPE TO SORT THE EIGENVALUES AND CORRESPONDING
C EIGEN VECTORS INTO ASCENDING ORDER

  DO 217 I=1,NP,2
  WRITE(*,*)ANG, I, D(I)
  WRITE(10,9999)ANG,D(I)
217     CONTINUE


250     CONTINUE


        STOP'END OF PROGRAM'
9999    FORMAT(F13.5)
        END



SUBROUTINE JACOBI(A,N,NP,D,V,NROT)
PARAMETER (NMAX=100)
DIMENSION A(NP,NP),D(NP),V(NP,NP),B(NMAX),Z(NMAX)
```

```
 DO 12 IP=1,N
   DO 11 IQ=1,N
     V(IP,IQ)=0.
11       CONTINUE
   V(IP,IP)=1.
12     CONTINUE
 DO 13 IP=1,N
   B(IP)=A(IP,IP)
   D(IP)=B(IP)
   Z(IP)=0.
13     CONTINUE
 NROT=0
 DO 24 I=1,50
   SM=0.
   DO 15 IP=1,N-1
     DO 14 IQ=IP+1,N
       SM=SM+ABS(A(IP,IQ))
14         CONTINUE
15       CONTINUE
   IF(SM.EQ.0.)RETURN
   IF(I.LT.4)THEN
     TRESH=0.2*SM/N**2
   ELSE
     TRESH=0.
   ENDIF
   DO 22 IP=1,N-1
     DO 21 IQ=IP+1,N
       G=100.*ABS(A(IP,IQ))
       IF((I.GT.4).AND.(ABS(D(IP))+G.EQ.ABS(D(IP)))
1          .AND.(ABS(D(IQ))+G.EQ.ABS(D(IQ))))THEN
         A(IP,IQ)=0.
       ELSE IF(ABS(A(IP,IQ)).GT.TRESH)THEN
         H=D(IQ)-D(IP)
         IF(ABS(H)+G.EQ.ABS(H))THEN
           T=A(IP,IQ)/H
         ELSE
           THETA=0.5*H/A(IP,IQ)
           T=1./(ABS(THETA)+SQRT(1.+THETA**2))
           IF(THETA.LT.0.)T=-T
         ENDIF
         C=1./SQRT(1+T**2)
         S=T*C
         TAU=S/(1.+C)
         H=T*A(IP,IQ)
         Z(IP)=Z(IP)-H
         Z(IQ)=Z(IQ)+H
         D(IP)=D(IP)-H
         D(IQ)=D(IQ)+H
         A(IP,IQ)=0.
         DO 16 J=1,IP-1
           G=A(J,IP)
           H=A(J,IQ)
           A(J,IP)=G-S*(H+G*TAU)
           A(J,IQ)=H+S*(G-H*TAU)
 16            CONTINUE
         DO 17 J=IP+1,IQ-1
           G=A(IP,J)
           H=A(J,IQ)
           A(IP,J)=G-S*(H+G*TAU)
```

```
          A(J,IQ)=H+S*(G-H*TAU)
 17            CONTINUE
        DO 18 J=IQ+1,N
          G=A(IP,J)
          H=A(IQ,J)
          A(IP,J)=G-S*(H+G*TAU)
          A(IQ,J)=H+S*(G-H*TAU)
 18            CONTINUE
        DO 19 J=1,N
          G=V(J,IP)
          H=V(J,IQ)
          V(J,IP)=G-S*(H+G*TAU)
          V(J,IQ)=H+S*(G-H*TAU)
 19            CONTINUE
        NROT=NROT+1
      ENDIF
 21          CONTINUE
 22        CONTINUE
  DO 23 IP=1,N
    B(IP)=B(IP)+Z(IP)
    D(IP)=B(IP)
    Z(IP)=0.
23        CONTINUE
24      CONTINUE
PAUSE '50 iterations should never happen'
RETURN
END


SUBROUTINE EIGSRT(D,V,N,NP)
DIMENSION D(NP),V(NP,NP)
DO 13 I=1,N-1
  K=I
  P=D(I)
  DO 11 J=I+1,N
    IF(D(J).GE.P)THEN
      K=J
      P=D(J)
    ENDIF
11        CONTINUE
  IF(K.NE.I)THEN
    D(K)=D(I)
    D(I)=P
    DO 12 J=1,N
      P=V(J,I)
      V(J,I)=V(J,K)
      V(J,K)=P
12          CONTINUE
  ENDIF
13      CONTINUE
RETURN
END
```

REFERENCES

1 K. P. Abdurakhmanov et al. Sov. Phys. Semicond. 19, 2 (1985) 1.

3 A.C. Aten et al, Phys. Lett. 11, 97, (1964)

4 A.C. Aten et al, Philips Res. Rep. 20, 395, (1965)

5 F. Beeler et al. " Mat. Res. Soc. Symp. " 46, (1985)

6 S. D. Brotherton et al. J. Appl. Phys. 57, 6 (1985)

7 L. T. Canham Ph. D. thesis " Optical Studies of Radiation Damage in Lithium Doped Silicon ", King's College London, (1983)

8 L. T. Canham et al. Physica 117B, 252 (1983)

9 L. T. Canham et al. Proc. 17th Int. Conf. Phys. Semicond, San Fransisco 1984, ed. J. D. Chadi & W. A. Harrison (Springer- Verlag N.Y.) p736 (1985)

10 R. A. Chapmanet al. Phys. Rev. 157, 615 (1967)

11 Z. Ciechanowska et al. Sol. Stat. Commun. 49, 427 (1984)

12 E. Cohen, M. D. Sturge Phys. Rev. B. 15, 1039 (1977)

13 C. B. Collins Phys. Rev. 108, 1409 (1957)

14 A. T. Collins et al. Phys. E. Sci. Instrum. 15, 712 (1982)

15 H. Conzelmann et al.J. Appl. Phys. A 30, 169 (1983)

17 H. Conzelmann " Proc. 13th Intern. Conf. on Defects in Semiconductors " Coronado Press (1984)

18 H. Conzelmann et al. Phys. Stat. Solidi. (b) 133, 655 (1986)

19 R. Czaputa et al. Sol. Stat. Commun. 47, 4 (1983)

20 G. Davies J. Phys. C. 15, 2779 (1982)

21 G. Davies J. Phys. C. 16, 5503 (1983)

22 G. Davies J. Phys. C. 17, 6331 (1984)

23 P. J. Dean et al, Phys. Rev. 185, 1064 (1969)

24 P. J. Dean et al, Sol. Stat. Commun. 9, 1555, (1971)

25 P. J. Dean, W. Schairer et al. J. Lumin. 9, 343 (1974)

26 P. J. Dean and D. C. Herbert, " Bound Excitons in Semicondictors ", Topics in Current Physics, vol. 14, edited by K. Cho, Springer Verlag, 1979, p. 82

27 G. G. DeLeo et al. Phys. Rev. B. 23, 4 (1981)

28 H. Dietrich et al. Sol. Stat. Commun. 58, 11 (1986)

29 R. E. Dietz et al, Phys. Rev. Lett. 8, 391, (1962)
30 M. C. do Carmo et al. " Proc. I. C. D. S. " Budapest (1988)
31 R. J. Elliott Phys. Rev. 108, 1384,(1957)
32 R. A. Faulkner Phys. Rev. 184, 713 (1969)
33 P. Fisher et al. Phys. Rev. Lett. 5, 195, (1960)
34 P. Fisher et al. J. Phys. Soc. Japan, 21, suppl. 21 (1966)
35 P. Fisher and A. K. Ramdas " Physics of the Solid State" ed. S. Balakrishna, M. Krishnamurthi and B. Ramachandra, Academic Press, N. Y. (1969).
36 M. A. Gilleo et al Phys. Rev. 174, 898,(1968)
37 H. P. Gislason et al. Phys. Rev. B. 26, 827 (1982)
38 H. P. Gislason et. al, Phys. Rev. B. 31, 6, 3774 (1985)
39 K. Graff et al. "Semiconductor Silicon 1981, Proc. 4th Intern. Symp. Si Materials Sci. & Tech. " Electrochem. Soc. N.J. 81-85 (1981)40 K. Graff et al. J. Electrochem. Soc. 128, 669 (1981)
2 K. Graff " Proc. 5thIntern. Symp. on Silicon Materials Science and Technology" (1986)
41 A. Hangleiter et al. Phys. Rev. Lett. 55, 2976 (1985)
42 M. Hansen " Constitution of Binary Alloys " McGraw-Hill N.Y. (1958)
43 L. A. Hemstreet Phys. Rev. B 15, 2 (1977)
44 C. H. Henry et al. Phys. Rev. B. 166, 754 (1967)
45 M. O. Henry et al. Sol. Stat. Commun. 64, 1 (1987)
46 M. O. Henry et al. Sol. Stat. Commun. 66, 7 (1988)
47 P. O. Holtz et al. J. Lumin. 34, 245 (1986)
48 J. J. Hopfield et al,Phys. Rev. 17, 312, (1966)
49 R. H. Hopkins et al. J. Cryst. Growth 42, 493 (1977)
50 A. E. Hughes and W. A. Runciman, Proc. Phys. Soc., 90, 827, (1967)
51 A. A. Kaplayanskii Opt. Spectrosc. 16, 329 (1964) (a)
52 A. A. Kaplayanskii Opt. Spectrosc. 16, 557 (1964) (b)
53 H. Katayama-Yoshida et al. Bull. Am. Phys. Soc. 30, 302 (1985)
54 L. C. Kimerling et al. " Defects and Radiation Effects in Semiconductors 1980 " Inst. Phys. Bristol (1981)
55 C. Kittel "Introduction to solid state physics", 5th

edition, Wiley & sons

56 M. Kleverman et al. " Mat. Res. Soc. Symp. Proc. " 104, (1988)

57 D. Labrie et al. Sol. Stat. Commun. 63, 115 (1987)

58 E. C. Lightowlers et al. Phys. Rev. B. 29, 4517 (1984)

59 E. C. Lightowlers et al. Proc E-MRS (1989) in press.

60 G. W. Ludwig et al. Sol. Stat. Phys. 13, 223 (1962)

61 I. K. Ludlow, J. Phys. C. (Proc. Phys. Soc.), Ser. 2, 1, 1194 (1968)

62 K. A. Maloney " A Uniaxial Stress Analysis of the Be Pair Bound Exciton Absorption Spectrum in Silicon ", M.Sc. thesis, N.I.H.E. (1986)

63 D. S. McClure "Electronic Spectra of Molecules & Ions in Crystals " Academic Press N.Y. (1959)

64 K. G. McGuigan et al. Sol. Stat. Commun. 68, 1 (1988)

65 A. G. Milnes " Deep Impurities in Semiconductors " Wiley N.Y. (1973)

66 N. S. Minaev et al. Sov. Phys. Semicond. 13, 233 (1979)

67 G. S. Mitchard et al. Sol. Stat. Commun. 29, 425 (1979)

68 H. D. Mohring et al. Phys. Rev. B 30, 894 (1984)

69 B. Monemar et al, Phys. Rev. B. 33, 1134 (1986)

70 A. V. Mudryi et al. Sov. Phys. - Semicond. 7, 117 (1973)

71 S. H. Muller et al. Phys. Rev. B 25, 1 (1982)

72 N. O'Donnell " Photoluminescence Studies of Silicon Doped with Zinc and Copper " M. Sc. thesis N.I.H.E. Dublin (1988).

74 P. Omling et al. Sol. Stat. Commun. 65, 7 (1988)

75 J. Pankove "Optical Processes in Semiconductors", Dover

76 A. Reilly " Excitation Transfer in Ruby ", M. Sc. thesis Physics Dept., University College Galway (1976).

77 A. Rohatgi et al. Solid-State Electron 23, 45 (1980)

78 W. Ruhle et al, Phys. Rev. B. 18, 7022, (1978)

79 R. Sauer et al. Physica 116B (1983)

80 T. E. Schlesinger et al. Phys. Rev. B 25, 7850 (1982)

81 F. A. Shunk " Constitution of Binary Alloys " McGraw-Hill N.Y. (1969)

82 M. S. Skolnick et al. J. Phys. C. 16, 1967 (1983)

83 M. S. Skolnick et al. J. Appl. Phys. 55, 2951 (1984)

84 T. Steiner et al. Sol. Stat. Commun. 49, 1121 (1984)

85 D. Thebault et al. Sol. Stat. Commun. 45, 7, 645 (1983)

86 M. L. W. Thewalt et al. Can J. Phys. 60, 1961 (1982)

87 M. L. W. Thewalt et al. Can J. Phys. 57, 1898 (1979)

88 D.G. Thomas et al, Phys. Rev. 131, 2397, (1963)

88a M. Tinkham " Group Theory and Quantum Mechanics ", McGraw - Hill, (1964)

89 V. D. Tkachev et al. Inst. Phys. Conf. Ser. 31, 231 (1977)

90 W.J. Turner et al, Appl. Phys. Lett. 3, 102, (1963)

91 M. A. Vouk et al. J. Lumin. 15, 357 (1977)

92 S. P. Watkins et al. Sol. Stat. Commun. 43, 687 (1982)

93 S. P. Watkins et al. Phys. Rev. B 29, 5727 (1984)

94 S. P. Watkins et al. Can. J. Phys. 63, 1074 (1985)

95 S. P. Watkins et al. Phys. Rev. B. 34, 2598 (1986)

96 R. K. Watts " Point Defects in Crystals " J. Wiley & Sons (1977)

97 E. R. Weber et al. Appl. Phys. Lett. 33, 433 (1978)

98 E. R. Weber Appl. Phys. A 30, (1983)

99 J. Weber et al. J. Phys. Soc. Jap. 49, suppl. A, 263 (1980)

100 J. Weber et al. Phys. Rev. B 25, 7688 (1982)

101 H. Weman et al. Appl. Phys. Lett. 47, 1110 (1985)

102 A. M. White et al, J. Phys. C. 7, L35, (1974)

103 N. Wiehl et al. J. Radioanal. Chem. 72, 1-2 (1983)

104 K. Wünstel et al. Appl. Phys. A 27 (1982)

105 A. Zunger et al. Phys. Rev. B 26, 5989 (1982)

106 A. Zunger et al. Phys. Rev. B 27, 2 (1983)

ACKNOWLEDGEMENTS

First and foremost I would like to thank my supervisor Martin Henry for his guidance, patience and encouragement over the last four years. In addition Celeste do Carmo, Gordon Davies and Ed Lightowlers have seen and heard a lot more from me than I suppose any of them had planned, so for their time and forebearance I am deeply grateful. Thanks also to the academic and technical staff at the N.I.H.E. / D.C.U. for their contributions when needed.

Special thanks should also go to :

Kev Dev , for the Rikadenki plotting routine and all the tender moments behind the curtain.

Jim Campion for the implanted zinc system diagrams.

Adrien Geissel for the P.C. screen dump program.

All the other post-grads in the department who have provided me with their friendship and advice on the project.